Guided wave mixing for damage detection in structural elements

By

Juan Carlos Pineda Allen

Thesis submitted in fulfillment of the requirements for the degree of

Doctor of Philosophy

The University of Adelaide

Faculty of Engineering, Computer and Mathematical Sciences

School of Civil, Environmental and Mining Engineering

Abstract

Thin-walled components are fundamental to numerous civil structures such as bridges, buildings, storage vessels, pipes, and becoming progressively diverse with their use in wind turbines, aircrafts and shipbuilding.

Identification and evaluation of damage in such structures plays a significant role in the early stage of the project conception, given that safety, performance and maintenance costs are three fundamental concepts in any engineering design. Structural Health Monitoring (SHM) was originated with collaboration across many disciplines to address a variety of structural issues and prevent dramatic losses.

Nonlinear guided waves combines the benefits of nonlinear ultrasound and guided waves. By means of linear parameters such as wave reflection, attenuation and transition, wave velocity, or wave modes, linear guided waves cannot detect micro-scale damage such as early stage fatigue, corrosion, micro-crack, or micro-delamination. In contrast, nonlinear guided wave have resulted promising due to incipient damage detection capabilities and reference-free potential, and leveraged its advantages over linear guided waves. This thesis investigates the use of nonlinear guided waves via a wave-mixing approach, where two ultrasonic frequencies are used, and the spectral content of the response is expected to carry information of the damage.

This thesis provides a physical insight into the wave-mixing technique for damage detection in structures. The phenomenon is investigated theoretically, numerically and through laboratory experiments. A number of published and prepared journal papers under the same topic is included in this thesis. In Chapter 1, an overview of the general concepts of Structural Health Monitoring and connected non-destructive testing techniques are introduced along with nonlinear guided wave techniques. A theoretical derivation to correlate the contact effect on a steel bolted joint with the spectral content of a signal response is proposed in Chapter 2. Thorough experiments

were carried out and demonstrated the robustness of the technique. Following, in Chapter 3, identification of debonding type of damage in adhesively bonded joints is investigated through three-dimensional finite element simulations and experiments. Numerical and experimental results revealed that guided wave-mixing technique could effectively detect debonding damage. To further extend the advantages of guided wave-mixing for different materials, a composite laminate plate in studied in Chapter 4. In this study, an imaging technique relying of the combined frequency wave is proposed to identify delamination and locate the defect. The proposed approach relies on network of few transducers and does not require reference data from undamaged samples. Lastly, a short study is presented in Chapter 5, where non-collinear pulses of finite time duration and non-planar wave-front are able to generate a resonant wave that is able to measure material nonlinearity, which is subject of study for many early stage fatigue damage detection techniques.

Overall, this thesis systematically revealed and capitalized the advantages of nonlinear guided wave-mixing technique for various types of damage in structures across a wide variety of materials.

Declaration

I certify that this work contains no material which has been accepted for the award of any other degree or diploma in my name, in any university or other tertiary institution and, to the best of my knowledge and belief, contains no material previously published or written by another person, except where due reference has been made in the text. In addition, I certify that no part of this work will, in the future, be used in a submission in my name, for any other degree or diploma in any university or other tertiary institution without the prior approval of the University of Adelaide and where applicable, any partner institution responsible for the joint-award of this degree.

I acknowledge that copyright of published works contained within this thesis resided with the copyright holder (s) of those works.

I also give permission for the digital version of my thesis to be made available on the web, via the University's digital research repository, the Library Search and through web search engines, unless permission has been granted by the University to restrict access for a period of time.

Signature: Date: 02 / 05 / 2022

Acknowledgement

First and foremost, I would like to thank God. I am truly grateful for His love, grace and blessings. He gave me the necessary abilities to pursue this journey.

I am immensely grateful to my supervisor, Prof. Ching Tai (Alex) Ng, for his invaluable support, guidance and encouragement. I found him pleasantly friendly, which is what any PhD student would like to have in an academic supervisor. Many thanks for his patience, support and knowledge. Special thanks to my co-supervisor Dr. Tohid Ghanbari Ghazijahani.

I thank my wife Mariam, for her unconditional love and tolerance. She took the plunge and moved to the opposite side of the planet with me, and I will forever acknowledge her for that. She has been there to listen, to share ideas, to encourage me to move forward during the challenging times and to celebrate the joyful moments.

I thank my mother Emilia and my father Juan Carlos (†), who passed away in the midst of the pandemic during the last year of my candidature. I am sure, however, he would be happy with me and proud of me on the successful completion of my PhD journey, as much as I know my mother is. Words fall short of how grateful I am for their love and their support; and for the ethical and critical thinking my parents instilled in me. I thank my sisters Claudia and Laura, my lovely nephew Juan I. and niece Maria E., for the love and support they have always given me despite the physical distance.

Special appreciation to all my workmates for the insightful academic discussions. Thanks to the administrative staff and laboratory technicians at the University, and to my friends in Adelaide. They all contributed to making my experience more enjoyable.

Finally, I would like to acknowledge the Department of Education, Skills and Employment through the Endeavour Leadership Program for the financial support.

Table of Contents

List of Figures

List of Tables

Chapter 1

Introduction

Chapter 1: Introduction

1.1 Background

The fast pace the world we live in requires safe, effective and rapid solutions for issues arising from ageing infrastructures and mechanical defects in aerospace, oil-gas and energy industries. There are also constantly new materials in the market that need to be scrutinized for safety and reliability prior to their extensive use. Few decades ago, structural health monitoring started gaining relevance with industry stakeholders and the international scientific community due to its cost-effective benefits. Though more importantly due to the catastrophic consequences when the monitoring system is not appropriately implemented or executed, such as the condominium collapse that killed 98 people in Florida USA in June 2021 [1], or the wind turbine collapse in Lemnhult Sweden due to bolt pre-tensioning issues in December 2015 [2]. Fortunately, no casualties were reported in the latter.

Figure 1. Vestas wind turbine collapse in Sweden [2]

1.2 Structural health monitoring

Structural Health Monitoring [3] or simply SHM was developed from the necessity to understand performance of structures in order to reduce the likelihood of structural failures. Failures can be originated due to design issues, construction errors, serviceability, and lack of maintenance, etc. and can be manifested through fatigue, corrosion, cracks, debonding, delamination and so on. SHM is a multidisciplinary technology and requires efforts and collaboration between different disciplines. Much interest have been put together to move from schedule-based maintenance to condition-based maintenance through embedding transducers for continuous monitoring. It has motivated research for integrated management of structures and potentially digital twins' models [4].

1.3 Non-destructive testing

Often related to SHM, non-destructive testing (NDT) methods were developed to inspect materials and structural components, to probe the existence of damage and to determine its severity. The main advantage of NDT methods as opposed to other testing methods is that NDT techniques are able to inspect the region of interest without causing any damage to the component. Numerous NDT methods serve for specific purposes. The most simple and conventional method is visual inspection, although this is time consuming and highly subjective. There are also electromagnetic methods such as eddy current or magnetic flux. Quite popular with porous materials is liquid penetrant testing. Other methods include guided waves, acoustic emission [5], ultrasonics [6], radiographic [7] and thermographic techniques [8].

Guided waves [9] testing offer promising advantages for long range inspection and localization of defects. Love waves, Rayleigh waves and Lamb waves are types of guided waves. Moreover, they can be used for material

characterization and damage quantification. More recently, they were proved effective in detecting early stage damage [10]. Guided wave is an ultrasonic wave with excitation frequency in the order of kilohertz. It is a kind of elastic wave propagating in solid medium, whose propagation characteristics depends on the boundary conditions of the component. Also well known for being suitable for inspecting thin-walled structures. Guided waves method is very attractive due to its (i) ability to inspect the entire cross-sectional area of the component, (ii) low-energy consumption, (iii) cost-effectiveness and (iv) ability to inspect considerable extension of structures.

1.4 Nonlinear guided waves

Linear guided wave methods are effective in detecting macro-scale damage such as open crack but it is less sensitive to microscale damage such as distributed micro-crack or localized material degradation, and less useful for early-warning detection mechanisms. Linear guided waves often require data of the inspected component before the damage happened, which can hinders its applicability because the baseline condition can change due to operational or environmental variations. To overcome these limitations, nonlinear guided waves combining the strength of guided waves and nonlinear ultrasonics have been developed [11]. The incident wave interacts with discontinuities and generates responses due to nonlinear acousto-mechanical behaviour at the damage. Second harmonic generation has gained popularity in the past few years due to its ability to detect fatigue damage [12], crack [13], or delamination. However, nonlinearities arising from contact effect of the damage can be masked by other contact sources such as the interface between transducers and the inspected component. The magnitude of the second harmonic is often of very small making it is hard to be

accurately measured. Testing equipment also introduces nonlinearity thus compromising the isolation of the nonlinearity source.

1.5 Mixed-frequency response in guided waves

In the more generic sense, mixed-frequency response consists of excitation signals at two different central frequencies and one or more waves might be generated due to material nonlinearity in intact specimens or contact nonlinearity produced by the defects. If a low frequency is used to excite the element and a high frequency is used to measure the induced elastic changes, the approach is normally known as vibro-acoustic modulation. Differently, in the so-called wave-mixing technique, two ultrasonic frequencies are used, and the spectral content of the response is expected to carry information of the damage. Wave-mixing can be classified in collinear and non-collinear depending on the angle between the incident waves. As shown in the literature [14-17], fundamental research mainly aims at understanding wave-mixing phenomenon can be found. There were also limited studies on damage-related mechanisms [18-20].

1.6 Thesis outline

This thesis comprehensively investigates the use of wave-mixing response of ultrasonic guided waves for damage detection and material characterization. It systematically examines the effect of guided wave mixing. A variety of materials and components are studied: aluminium plates, composites plates, steel bolted joints, adhesively bonded aluminium joints. Moreover, different actuating and sensing mechanisms are used.

An introduction into the general concept of SHM and NDT is presented in Chapter 1. Further explanation of guided waves based NDT is provided with a

more detailed overview of nonlinear guided waves and mixed-frequency response.

Chapter 2 presents a theoretical development and experimental investigation into nonlinear guided-wave mixing for integrity monitoring of bolted joints in plates. The proposed study relies on the combined frequency wave originated by contact effect at the bolted joint to evaluate the applied torque level in the joint. Practical, small and inexpensive piezoelectric wafer transducers facilitate future applications for online bolted joints monitoring.

In Chapter 3, an accurate 3D finite element model was developed to simulate the mixed frequency response of an antisymmetric (A_0) Lamb wave propagation and its interaction with debonding at an adhesively bonded aluminium joint. A number of different numerical and experimental case studies employing ultrasonic transducers and noncontact sensing demonstrated the proposed approach can be effective and reliable for indicating local debonding.

In Chapter 4, the use of wave-mixing technique in composite laminates in studied for the purpose of damage detection. A validated numerical model is developed and an algorithm based on the arrival time of the combined frequency wave is implemented to locate delamination type of damage in a composite plate. The proposed method does not need baseline measurement.

In Chapter 5, numerical simulations and experiments are carried to demonstrate that non-planar wave front and finite time duration in non-collinear wave-mixing can effectively measure material nonlinearity.

Finally, conclusions of the thesis are summarized in Chapter 6. This is followed by recommendations for future research and potential study directions.

1.7 List of publications

1.7.1 List of journal papers

i) Pineda Allen, J.C.; Ng, C.T. Nonlinear Guided-Wave Mixing for Condition Monitoring of Bolted Joints. *Sensors 2021*, 21, 5093. https://doi.org/10.3390/s21155093

ii) Pineda Allen, J.C.; Ng, C.T. Debonding detection at adhesive joints using nonlinear Lamb waves mixing. *NDT & E International 2021*, 125. https://doi.org/10.1016/j.ndteint.2021.102552

iii) Pineda Allen, J.C.; Ng, C.T. Damage detection in composites laminates using nonlinear guided wave mixing (under preparation).

iv) Pineda Allen, J.C.; Ng, C.T. Mixing of non-collinear Lamb wave pulses in plates with material nonlinearity (under preparation).

1.7.2 List on conference papers

i) Pineda Allen, J. C. ; NG, C. T. Bolted joint torque monitoring using ultrasonic Lamb wave mixing, *2021 IEEE International Ultrasonics Symposium (IUS)*, 2021, pp. 1-5, doi: 10.1109/IUS52206.2021.9593401

ii) Pineda Allen, J.C.; Ng, C.T. Guided wave mixing and bispectrum analysis for monitoring of bolted joints. *10th Australasian Congress on Applied Mechanics* (Online).

1.8 References

1. Guardian, T. *Miami building collapse: one dead as rescue crews say 99 unaccounted for*. Miami building collapse: one dead as rescue crews say 99 unaccounted for, 2021.
2. *Accident of the wind turbine in Lemnhult, Velanda Municipality, Jönköping County, 24 December 2015*. 2017, Swedish Accident Investigation Authority (In Swedish).
3. Farrar, C. and K. Worden, *An introduction to structural health monitoring.* Philosophical Transactions of the Royal Society A: Mathematical, Physical and Engineering Sciences, 2007. **365**(1851): p. 303-315.
4. Vega, M.A., et al., *Diagnosis, Prognosis, and Maintenance Decision Making for Civil Infrastructure: Bayesian Data Analytics and Machine Learning*, in *Structural Health Monitoring Based on Data Science Techniques*, A. Cury, et al., Editors. 2022, Springer International Publishing: Cham. p. 45-73.
5. Kaphle, I.M., et al., *Damage quantification techniques in acoustic emission monitoring*, in *Sixth World Congress on Engineering Asset Management*. 2011: Cincinnati, OH, USA.
6. Bray, D.E., *Ultrasonic Systems for Industrial Nondestructive Evaluation*, in *Ultrasonic Nondestructive Evaluation*, T. Kundu, Editor. 2004, CRC Press: Boca Raton, FL.
7. Yenumula, L., et al., *Radiographic evaluation of gas tungsten arc welded joints used in nuclear applications by X- and gamma-rays.* NDT & E International, 2019. **102**: p. 144-152.
8. Addepalli, S., et al., *Non-destructive evaluation of localised heat damage occurring in carbon composites using thermography and thermal diffusivity measurement.* Measurement, 2019. **131**: p. 706-713.
9. Rose, J.L., *Ultrasonic Waves in Solid Media*. The Journal of the Acoustical Society of America. 1999, New York: Cambridge University Press. 1807-1808.
10. Lissenden, C., *Nonlinear ultrasonic guided waves—Principles for nondestructive evaluation.* Journal of Applied Physics, 2021. **129**(2): p. 021101.
11. Chillara, V. and C. Lissenden, *Review of nonlinear ultrasonic guided wave nondestructive evaluation: theory, numerics, and experiments.* Optical Engineering, 2015. **55**(1): p. 011002.
12. Deng, M. and J. Pei, *Assessment of accumulated fatigue damage in solid plates using nonlinear Lamb wave approach.* Applied Physics Letters, 2007. **90**(12): p. 121902.
13. Yang, Y., et al., *Second harmonic generation at fatigue cracks by low-frequency Lamb waves: Experimental and numerical studies.* Mechanical Systems and Signal Processing, 2018. **99**: p. 760-773.
14. Hasanian, M. and C. Lissenden, *Second order harmonic guided wave mutual interactions in plate: Vector analysis, numerical simulation, and experimental results.* Journal of Applied Physics, 2017. **122**(8): p. 084901.
15. Hasanian, M. and C. Lissenden, *Second order ultrasonic guided wave mutual interactions in plate: Arbitrary angles, internal resonance, and finite interaction region.* Journal of Applied Physics, 2018. **124**(16): p. 164904.
16. Ishii, Y., S. Biwa, and T. Adachi, *Non-collinear interaction of guided elastic waves in an isotropic plate.* Journal of Sound and Vibration, 2018. **419**: p. 390-404.

17. Li, W., et al., *Theoretical analysis and experimental observation of frequency mixing response of ultrasonic Lamb waves.* Journal of Applied Physics, 2018. **124**(4): p. 044901.
18. Jingpin, J., et al., *Nonlinear Lamb wave-mixing technique for micro-crack detection in plates.* NDT & E International, 2017. **85**: p. 63-71.
19. Metya, A., S. Tarafder, and K. Balasubramaniam, *Nonlinear Lamb wave mixing for assessing localized deformation during creep.* NDT & E International, 2018. **98**: p. 89-94.
20. Li, W., et al., *Impact damage detection in composites using a guided wave mixing technique.* Measurement Science and Technology, 2019. **31**(1): p. 014001.

Chapter 2

Nonlinear Guided-Wave Mixing for Condition Monitoring of Bolted Joints

Juan Carlos Pineda Allen and Ching Tai Ng

School of Civil, Environmental and Mining Engineering

The University of Adelaide, SA 5005, Australia

Publication: Pineda Allen, J.C.; Ng, C.T. Nonlinear Guided-Wave Mixing for Condition Monitoring of Bolted Joints. Sensors 2021, 21, 5093.

https://doi.org/10.3390/s21155093

Statement of Authorship

Title of Paper	Nonlinear Guided-Wave Mixing for Condition Monitoring of Bolted Joints
Publication Status	☑ Published ☐ Accepted for Publication ☐ Submitted for Publication ☐ Unpublished and Unsubmitted w ork w ritten in manuscript style
Publication Details	Pineda Allen, J.C.; Ng, C.T. Nonlinear Guided-Wave Mixing for Condition Monitoring of Bolted Joints. Sensors 2021, 21, 5093. https://doi.org/10.3390/s21155093

Principal Author

Name of Principal Author (Candidate)	Juan Carlos Pineda Allen
Contribution to the Paper	Performed literature review, derived theoretical equations, developed and prepared the experimental configuration and specimen, performed experiments, data processing and analyses, and prepared the manuscript.
Overall percentage (%)	80%
Certification:	This paper reports on original research I conducted during the period of my Higher Degree by Research candidature and is not subject to any obligations or contractual agreements with a third party that would constrain its inclusion in this thesis. I am the primary author of this paper.
Signature	Date: 23/02/2022

Co-Author Contributions

By signing the Statement of Authorship, each author certifies that:

i. the candidate's stated contribution to the publication is accurate (as detailed above);

ii. permission is granted for the candidate in include the publication in the thesis; and

iii. the sum of all co-author contributions is equal to 100% less the candidate's stated contribution.

Name of Co-Author	Ching Tai Ng
Contribution to the Paper	Supervised the work, reviewed the manuscript, prepared for submission and acted as corresponding author.
Signature	Date: 24/02/2022

Name of Co-Author	
Contribution to the Paper	
Signature	Date:

Please cut and paste additional co-author panels here as required.

Chapter 2: Nonlinear Guided-Wave Mixing for Condition Monitoring of Bolted Joints

Abstract

Bolted joints are fundamental to numerous structural components in engineering practice. Nevertheless, their failure or even their loosening can lead to insufficient performance and reduced structural safety. This study presents a theoretical development and experimental investigation into nonlinear guided-wave mixing for integrity monitoring of bolted joints in plates. Combinational harmonics generated due to nonlinear Lamb wave mixing and contact acoustic nonlinearity at the bolted joints were used to evaluate the applied torque level in the joint. The area of the power spectral density in the region of the sum combinational harmonic bandwidth is found to be highly correlated to the applied torque level at the joint. Moreover, the effect of the number of cycles and thus the time duration of the excitation is investigated. The results show that the combinational harmonics remain robust for different numbers of cycles in detecting bolt loosening. The findings presented in this study also provide physical insight into the phenomena of nonlinear Lamb wave mixing for evaluating applied torque in bolted joints, and the results help further advance the use of nonlinear guided waves for damage detection.

Keywords: wave mixing; bolt loosening; bolted joint; Lamb wave; combination harmonic; guided wave; nonlinear

2.1 Introduction

To evaluate changes in structural performance, the capabilities of both structural health monitoring (SHM) and non-destructive testing (NDT) have been joined to be developed and implemented in real structures. Integrity and safety are paramount to any structural components; hence, there is great interest in early damage and degradation detection. Bolted structural connection is an efficient and versatile connection technique widely used in various engineering structures such as bridges [1], wind turbines [2], and buildings [3]. In these types of structures, the unsatisfactory performance of connections can drastically compromise the structure. Previous studies revealed that bolt loosening can significantly decrease the fatigue life of bolted joints [4].

A direct approach to monitor bolted joints is through the installation of load cells or strain gauges at the bolts. However, this approach requires as many load cells as bolts to monitor the bolted connections. This significantly increases inspection and operational cost for structures. Alternatively, indirect methods have also been studied in the literature. Traditional ultrasonic techniques have been investigated for axial force monitoring in bolts [5, 6]. Transmittance [7], impedance [8], and coda wave [9] methods have also been investigated.

2.1.1 Guided waves for bolt condition assessment

Contrary to traditional NDT techniques, methods based on guided waves (GWs) have the ability to inspect large and inaccessible areas. They have attracted significant research interest for NDT and SHM in recent years. GWs have the ability to propagate in different types of structural elements, such as beams [10], bars [11], pipes [12], and plates [13], and their multimodality [14, 15] provides flexibility in inspecting structures. Wang *et al.* [16] demonstrated that the energy propagated across the bolt can potentially indicate the bolt's status. They also studied a time-reversal linear GW-based method and showed that the bolt

preload values correlate with the peak amplitude for the focused signal [17]. However, nonlinear methods possess advantages over their linear counterparts. Linear features, e.g., time-of-flight, of the scattered waves or mode-converted waves from damage are difficult to extract when there are many wave reflections in the time-domain signals. At the very early stage, time-domain features for linear GW techniques may not be sufficient to detect bolt-loosening effects.

2.1.2 Nonlinear features of guided waves

It was demonstrated that nonlinear features can potentially outperform linear techniques for early bolt-loosening detection. Damage indexes were developed for both linear and nonlinear acoustic/ultrasound approaches, and those were fit by hyperbolic tangent functions [18]. An impact-modulation technique showed a correlation between a modulation index and the bolt condition. It was demonstrated that this index is sensitive to the wave-actuating and -sensing location [19]. Based on the overall dynamic behaviour of the structure, a linear approach and nonlinear vibro-acoustic modulation technique study was conducted in [20]. Van de Abeele *et al.* [21] illustrated the use of nonlinear wave modulation and explored its benefits in detecting crack damage in different materials. Further wave modulation studies with concrete [22] and composite laminates [23] focusing on sideband peak count were also conducted. The aforementioned techniques rely on sideband generation. However, shakers [20] or impact hammers [19] are essential devices for the impact-modulation and vibro-acoustic modulation techniques. They significantly increase the cost of these techniques and restrict the applicability of these techniques for in situ monitoring.

Analogous to bulk waves, nonlinear GW-based methods have proven more effective compared to linear GW-based methods [24, 25], with the benefits of GW methods mentioned earlier, such as increased propagation distances and

accessibility. More recently, Lissenden *et al.* [26] systematically presented the use of nonlinear GWs for NDT, paying special attention to early material degradation detection. They rely on nonlinear acoustic phenomena and are sensitive in detecting early-stage fatigue [27, 28], local debonding [29], and delamination [30]. In the literature, there were very few studies that investigated the use of nonlinear GWs for bolt joints monitoring. Yang *et al.* [31] investigated second harmonic generation due to fatigue crack. They showed that it is possible to differentiate cases when the bolted joint is weakened by fatigue crack. However, the magnitude of the second harmonic is usually very small, which makes it hard to accurately measure. The testing equipment can also introduce nonlinearities that mask harmonics generated by damage-related nonlinearities. Contact between the specimens and the probing transducers can similarly create non-damage-related nonlinearities.

2.1.3 Guided wave mixing

Given the multimodal nature of guided waves, and the existence of higher-order propagation modes, limited work in the field of nonlinear guided-wave mixing can be found in the literature, aiming at fundamentally understanding the mixing phenomenon as in [32-35] and some types of damage-related mechanisms [36-38]. Croxford *et al.* [39] investigated material degradation detection using wave mixing, and Jingpin *et al.* investigated the use of wave mixing to detect fatigue crack [40] and thermal corrosion [41] damage in steel specimens. These studies demonstrated the advantages of wave-mixing techniques in detecting micro-cracks, fatigue, and plasticity damage. Even though researchers have explored the use of bulk waves in wave mixing, conventional ultrasonics can inspect only the area covered by the transducer. This is not cost-effective, and defects or damage can sometimes be missed.

Further research is required not only to understand the mixing phenomenon but also to appreciate and benefit from the advantages of nonlinear wave mixing. The need for premature bolt-loosening detection in structures by an inexpensive, reliable, and prompt detection method has motivated this research. Nonlinear guided-wave mixing in bolted structural joints has not been fully investigated in the literature. As such, this study experimentally explores Lamb wave mixing on a steel bolted joint to demonstrate that bolt-loosening effects can be correlated to the combined sum harmonic. Moreover, the use of small and low-cost piezoceramic transducers, instead of traditional ultrasonic transducers, broadens the applicability of the proposed approach to allow integration into in situ NDT and SHM systems. Using nonlinear guided-wave-mixing techniques, the advantages of mid- to long-range inspection would reduce inspection times, resulting in lower related costs, with the added ability to detect early-stage damage [42, 43]. This study aims to investigate the use of mixed-frequency responses for monitoring bolted joints. The study focuses on using combined frequency responses for assessing the condition of the bolted joint.

The paper is organised as follows. The first section provides a theoretical framework for the wave-mixing phenomenon. The following section outlines the experimental setup, in which the specimen is described and the wave-actuation and -sensing approach is presented. The excitation signal selection is described in the next section, following the mechanisms for the applied torque studies. This is followed by the results comparing the signals in the time domain with their limitations and the analysis of the proposed mixed-frequency technique. The effect of the number of cycles is studied next, and this study is then finished with concluding remarks.

2.2 Theoretical background

When an incident GW containing two sinusoidal pulses propagates through a pristine material, the frequency spectrum of the received wave ideally contains frequency components corresponding only to the central frequencies of the two incident sinusoidal signals. However, when the wave travels through a region where a source of nonlinearity is present (e.g., damage- or material-related), higher and combinational harmonics are present in the amplitude spectra of the received wave pulses, in addition to components at the central frequencies of the two incident sinusoidal pulses. The explanation for this phenomenon is that the incident sinusoidal pulses interact with the nonlinearity source and generate the higher and combinational harmonics.

The bolted joint investigated in this paper is considered as a contact interface whose pressure between contact faces varies according to the applied force between the bolt and nut. A simplified approach is used in this study. We consider the joint behaving as a single-degree-of-freedom system with bilinear stiffness [19, 44] subjected to an excitation consisting of two sinusoidal forces, each one corresponding to each sinusoidal wave. Consider the following input excitation that consists of two tone-burst pulses:

$$P(t) = P_{\mathrm{a}} \cos \omega_{\mathrm{a}} t \left(1 - \frac{\omega_{\mathrm{a}} t}{N_{\mathrm{a}}}\right) + P_{\mathrm{b}} \cos \omega_{\mathrm{b}} t \left(1 - \frac{\omega_{\mathrm{b}} t}{N_{\mathrm{b}}}\right) \tag{1}$$

where P_{a} and P_{b} are the individual forces (with their corresponding amplitudes). ω_{a} and ω_{b} are the central frequencies, and N_{a} and N_{b} are the corresponding numbers of cycles. t represents the time. The equation of motion of the system can be written as follows [20]:

$$P_{\mathrm{a}} \cos \omega_{\mathrm{a}} t \left(1 - \cos \frac{\omega_{\mathrm{a}} t}{N_{\mathrm{a}}}\right) + P_{\mathrm{b}} \cos \omega_{\mathrm{b}} t \left(1 - \cos \frac{\omega_{\mathrm{b}} t}{N_{\mathrm{b}}}\right) = m\ddot{y} + k_1 y - \varphi k_2 y^2 \tag{2}$$

where m denotes the mass and φ is used to scale the nonlinear part in the perturbation solution.

The linear and nonlinear contact stiffnesses are represented by k_1 and k_2, respectively. The incident wave would interact with the imperfect contact interface, and the solution to Equation (2) using perturbation theory can be expressed as:

$$y = y_{\mathrm{l}} + y_{\mathrm{sh}} + y_{\mathrm{ch}} \tag{3}$$

which consists of the linear response y_{l} and nonlinear responses from second and combinational harmonics, y_{sh} and y_{ch}, respectively. Substituting Equation (3) into Equation (2), we obtain the following relation:

$$m\ddot{y}_{\mathrm{l}} + k_1 y_{\mathrm{l}} = P_{\mathrm{a}} \cos\omega_{\mathrm{a}} t \left(1 - \cos\frac{\omega_{\mathrm{a}} t}{N_{\mathrm{a}}}\right) + P_{\mathrm{b}} \cos\omega_{\mathrm{b}} t \left(1 - \cos\frac{\omega_{\mathrm{b}} t}{N_{\mathrm{b}}}\right) \tag{4}$$

$$m\ddot{y}_{\mathrm{sh}} + k_1 y_{\mathrm{sh}} - k_2 y_{\mathrm{l}}^2 = 0 \tag{5}$$

$$y = y_{\mathrm{l}} + y_{\mathrm{sh}} + y_{\mathrm{ch}} \tag{6}$$

Ignoring the transient components, and making the coefficients equal, linear and nonlinear responses are obtained as below:

$$y_{\mathrm{l}} = A_1 \cos\omega_{\mathrm{a}} t \left(1 - \cos\frac{\omega_{\mathrm{a}} t}{N_{\mathrm{a}}}\right) + A_2 \cos\omega_{\mathrm{b}} t \left(1 - \cos\frac{\omega_{\mathrm{b}} t}{N_{\mathrm{b}}}\right) \tag{7}$$

$$y_{\mathrm{sh}} = B_1 k_2 \cos 2\omega_{\mathrm{a}} t \left(1 - \cos\frac{2\omega_{\mathrm{a}} t}{N_{\mathrm{a}}}\right) + B_2 k_2 \cos 2\omega_{\mathrm{b}} t \left(1 - \cos\frac{2\omega_{\mathrm{b}} t}{N_{\mathrm{b}}}\right) \tag{8}$$

$$\begin{aligned} y_{\mathrm{ch}} = {} & C_1 k_2 \cos(\omega_{\mathrm{a}} + \omega_{\mathrm{b}}) t \left(1 - \cos\frac{\omega_{\mathrm{a+b}} t}{N_{\mathrm{a}}}\right) \\ & + C_2 k_2 \cos(\omega_{\mathrm{a}} - \omega_{\mathrm{b}}) t \left(1 - \cos\frac{\omega_{\mathrm{a-b}} t}{N_{\mathrm{b}}}\right) \end{aligned} \tag{9}$$

where:

$$A_1 = \frac{P_{\mathrm{a}} \left(1 - \cos\frac{\omega_{\mathrm{a}} t}{N_{\mathrm{a}}}\right)}{k_1 \left(1 - \cos\frac{\omega_{\mathrm{a}} t}{N_{\mathrm{a}}}\right) + m\omega_{\mathrm{a}}^2 \left(\cos\frac{\omega_{\mathrm{a}} t}{N_{\mathrm{a}}} - 1\right) + \frac{m\omega_{\mathrm{a}}^2}{N_{\mathrm{a}}^2} \cos\frac{\omega_{\mathrm{a}} t}{N_{\mathrm{a}}}} \tag{10}$$

$$A_2 = \frac{P_b\left(1-\cos\frac{\omega_b t}{N_b}\right)}{k_1\left(1-\cos\frac{\omega_b t}{N_b}\right)+m\omega_b^2\left(\cos\frac{\omega_b t}{N_b}-1\right)+\frac{m\omega_b^2}{N_b^2}\cos\frac{\omega_b t}{N_b}} \tag{11}$$

$$B_1 = \frac{0.5A_1^2\left(1-\cos\frac{\omega_a t}{N_a}\right)^2}{k_1\left(1-\cos\frac{2\omega_a t}{N_a}\right)+4m\omega_a^2\left(\cos\frac{2\omega_a t}{N_a}-1\right)+\frac{4m\omega_a^2}{N_a^2}\cos\frac{2\omega_a t}{N_a}} \tag{12}$$

$$B_2 = \frac{0.5A_2^2\left(1-\cos\frac{\omega_b t}{N_b}\right)^2}{k_1\left(1-\cos\frac{2\omega_b t}{N_b}\right)+4m\omega_b^2\left(\cos\frac{2\omega_b t}{N_b}-1\right)+\frac{4m\omega_b^2}{N_b^2}\cos\frac{2\omega_b t}{N_b}} \tag{13}$$

$$C_1 = \frac{A_1A_2\left(1-\cos\frac{\omega_a t}{N_a}\right)\left(1-\cos\frac{\omega_b t}{N_b}\right)}{k_1\left(1-\cos\frac{\omega_{a+b} t}{N_a}\right)+m\omega_{a+b}^2\left(\cos\frac{\omega_{a+b} t}{N_a}-1\right)+\frac{m\omega_{a+b}^2}{N_a^2}\cos\frac{\omega_{a+b} t}{N_a}} \tag{14}$$

$$C_2 = \frac{A_1A_2\left(1-\cos\frac{\omega_a t}{N_a}\right)\left(1-\cos\frac{\omega_b t}{N_b}\right)}{k_1\left(1-\cos\frac{\omega_{a-b} t}{N_b}\right)+m\omega_{a-b}^2\left(\cos\frac{\omega_{a-b} t}{N_b}-1\right)+\frac{m\omega_{a-b}^2}{N_b^2}\cos\frac{\omega_{a+b} t}{N_b}} \tag{15}$$

where $\omega_{(a\pm b)} = \omega_a \pm \omega_b$. It can be seen from Equation (9) that the magnitude of the combinational harmonics is proportional to the nonlinear stiffness k_2 and thus related to the applied torque at the bolted joint. The contact mechanism between interfaces during motion generates the contact acoustic nonlinearity (CAN). The amplitude spectra of the response contain three components. They are: (i) the linear component as shown in Equation (7) that is related to the input frequencies; (ii) a nonlinear component as shown in Equation (8) that consists of higher harmonics; and (iii) a nonlinear component as shown in Equation (9) that consists of combinational harmonics resulting from guided-wave mixing. This phenomenon is schematically illustrated in Figure 2.1. For the incident wave travelling through a linear medium, the response spectrum of the received wave would contain frequency components corresponding only to the two incident waves as shown in Figure 2.1a. In contrast, in the presence of a nonlinearity source, such as the imperfect contact interface between plates, the response spectrum of the received wave would contain higher-order harmonics such as second harmonics and combined harmonics, as shown in Figure 2.1b.

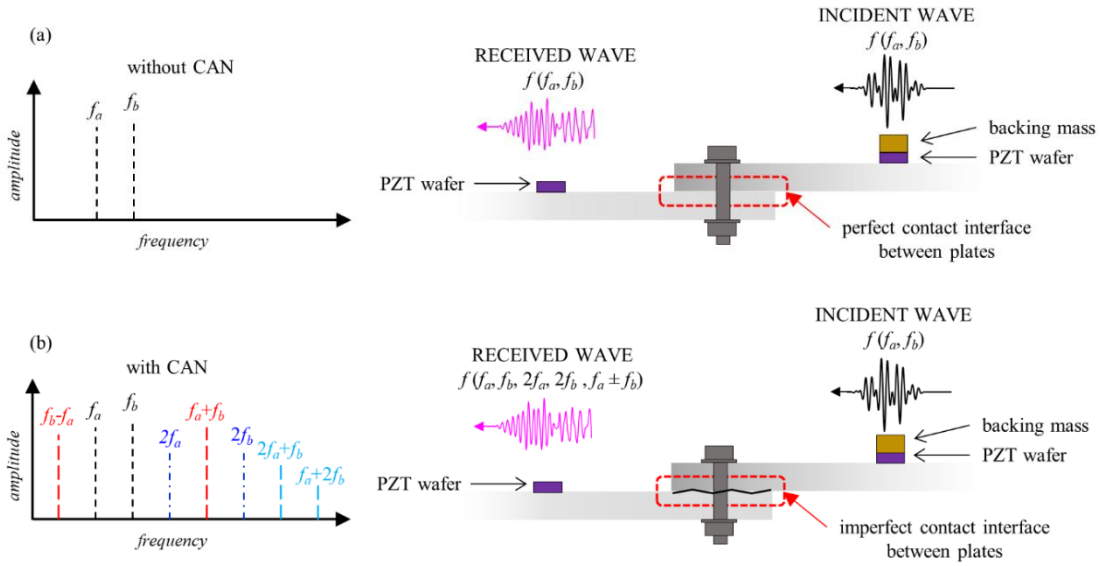

Figure 2.1. Contact acoustic nonlinearity phenomenon in the bolted joint with (a) perfect contact interface and (b) imperfect contact interface

2.3 Experimental setup

2.3.1 Specimen description

Steel plates were chosen in this study, which are among the most commonly used materials in the civil and mechanical engineering industry. In general, the findings of this study are applicable to other metallic specimens. The experiments for demonstrating the proposed method were conducted on bolted joints composed of two steel plates, with each of them having in-plane dimensions of 200 mm × 360 mm and thickness of 3 mm, as shown in Figure 2.2. Both plates are made of G250 mild steel, whose material properties are Young Modulus E_s = 205 GPa; density ρ_s = 7820 kg/m^3; and Poisson ratio ν_s = 0.29. Each plate has three 10 mm drilled holes, and M10 bolts and nuts were used to join the plates with 40 mm overlap.

A digital torque wrench, Sidchrome SCMT26952, was used to gradually tighten the bolts. The torque wrench sensitivity was ± 2%. Different torque levels, eleven in total, were applied, and signals were measured at each torque.

Minimum applied torque was 20 Nm and maximum was 70 Nm, in 5 Nm steps. Once the eleven levels of applied torque were applied, the bolts were loosened, and the process was repeated for the same eleven levels of the applied torque. The experiment was repeated five times independently. The first part of our analysis is conducted for a single measurement to provide an illustration of the signal quality and the proposed method, and the study finally presents the data for the five independent measures.

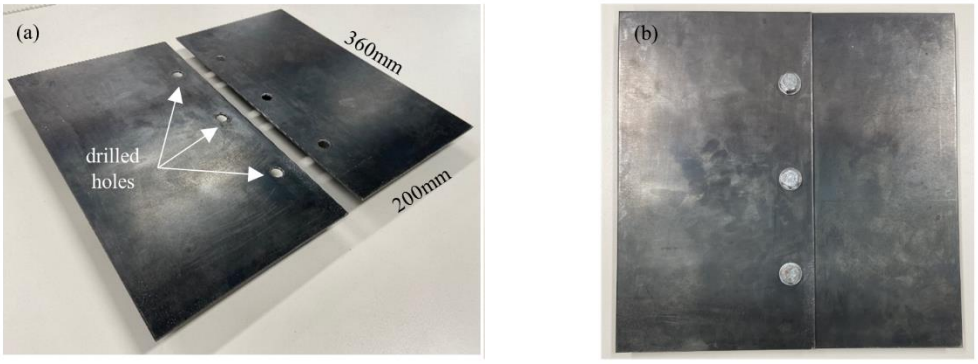

Figure 2.2. Steel specimens (a) before joint; (b) after bolted joint

2.3.2 Equipment setup

A circular piezoceramic transducer (PZT) with 5 mm diameter and 2 mm thick was bonded to one of the steel plates using silver conductive epoxy at a distance of 40 mm from the centre of the machined bolt hole. A pitch-catch GW excitation and sensing approach is used in this study. To increase the out-of-plane excitability of the actuator, a brass backing mass was bonded to the top of the transducer using the same conductive epoxy. Another piezoceramic transducer (5 mm diameter and 2 mm thick) was bonded to the other steel plate to receive the actuated wave signal. Using the pitch-catch approach, the signal received by the sensor was expected to carry information from the bolted joint as this signal was generated at the left-hand side of the plate, passed through the bolted joint,

and was measured by the sensor located at the right-hand side. A schematic diagram of the actuating and sensing arrangement is shown in Figure 2.3.

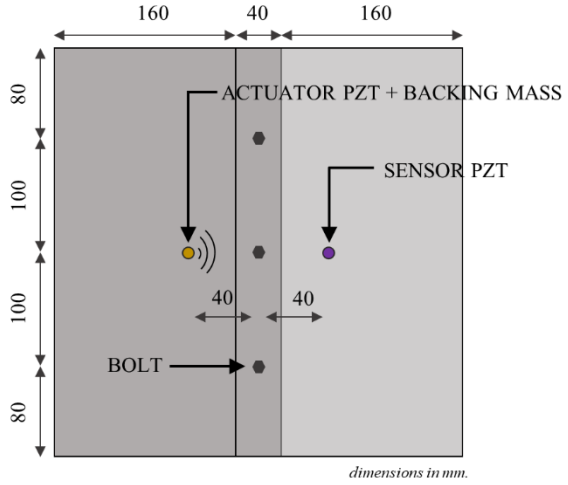

Figure 2.3. Schematic diagram of the actuating and sensing arrangement

An NI PXI-5412 arbitrary wave generator (AWG) was used to generate the excitation signal, which was then fed to a high-power signal amplifier. The signal consists of two sinusoidal tone-burst pulses modulated by Hann windows. These two pulses merged into one signal before sending it to the amplifier. The signal was amplified up to 120 V using a CIPRIAN HVA-400 amplifier and then sent to the actuator. The acquisition was averaged 500 times to improve the signal-to-noise ratio of the measured wave signal. The sensor was connected to an NI PXI-5122 digitiser, and the digitised data were sent to the computer for post-processing. The experimental setup is shown in Figure 2.4.

2.3.3 Excitation signal and frequency selection for wave mixing

Two sinusoidal tone-burst pulses with different central frequencies were merged into one single excitation signal before sending to the amplifier. Preliminary tests with single-frequency pulses were first conducted to evaluate the single-frequency response of the piezoceramic transducers. After that, different

frequency combinations were examined to find a suitable frequency combination for the tests. Central frequencies of both pulses were chosen so that (i) the sum combinational frequency would not be a multiple of any of the input frequencies and, (ii) the frequency response of the piezoceramic transducers would be optimised. The combinational harmonic investigated in this study is generated by contact nonlinearity at the bolted joint due to bolt loosening. This is not required to fulfil the internal resonance conditions necessary for evaluating material nonlinearity. One of the sinusoidal pulses was at 110 kHz with 10 cycles, whereas the other sinusoidal pulse was at 160 kHz with 14 cycles. Then, both sinusoidal pulses were added together. The number of cycles was selected so that the durations of both single-frequency sinusoidal tone-burst pulses would be the same and have similar energy content.

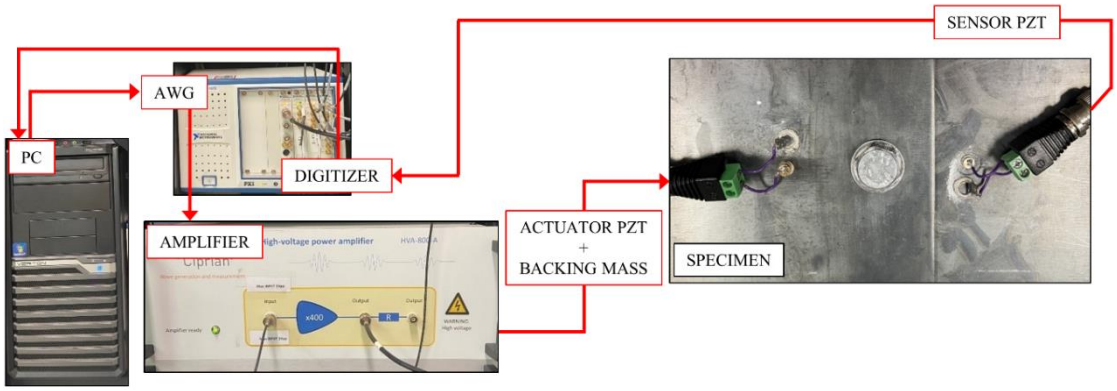

Figure 2.4. Signal generation and acquisition setup.

2.4 Results

A typical input signal for wave mixing is shown in Figure 2.5, which combines two sinusoidal tone bursts with excitation frequencies as described in the last section. The corresponding received signal, which passed through the bolted joint, is shown in Figure 2.6. The figure shows the signals of two levels of applied torque.

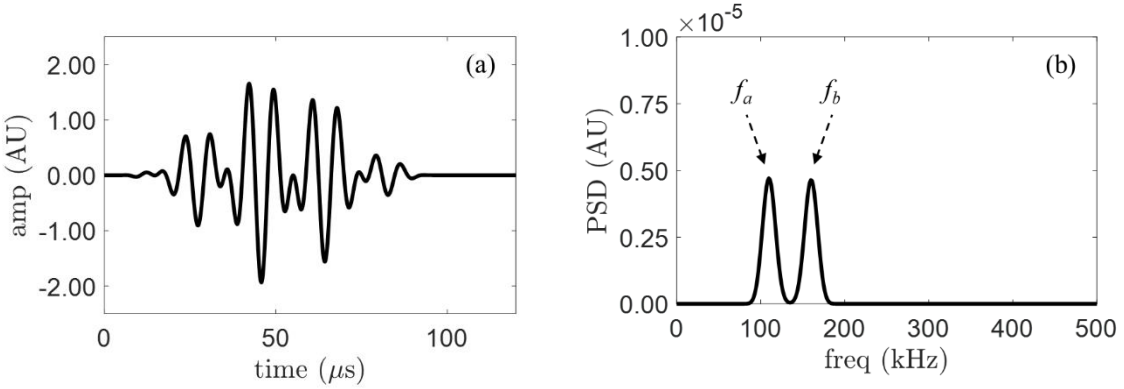

Figure 2.5. (a) Typical time history of the input signal created by merging two signals at different frequencies; (b) Typical spectrum of the input signal.

Signals in the time domain can also be compared to some extent. In Figure 2.6, the received signal for an applied torque of 20 Nm and 50 Nm are plotted together. It can be observed that the signal that travelled through the bolted joint with a greater magnitude of applied torque arrives slightly faster than that which travelled through the bolted joint with a lesser magnitude of applied torque. This can be explained by the fact that when the applied torque of the bolts is increased, the bolted joints tighten the plates. They are in a full-contact situation, and the plates behave like an integrated solid element. Hence, the wave propagates faster. On the other hand, when the bolts are loosened, the interfacial contact between the plates is reduced, and the plates jointed by bolt are less similar to a single solid element. Hence, the wave takes a longer time to arrive at the sensor.

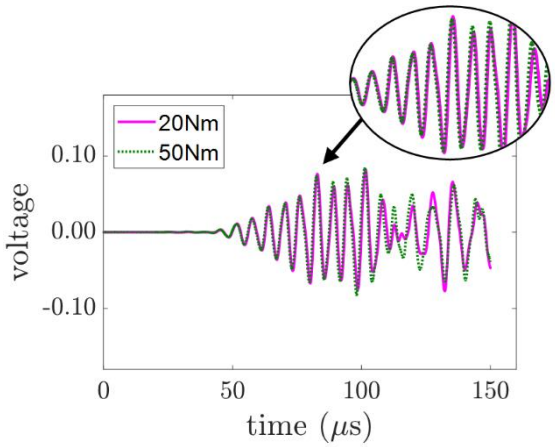

Figure 2.6. Measured responses of two levels of applied torque.

However, time-domain features add extra complexity to the data analysis when complicated pulses and wave reflections are involved, especially when the incident wave is not a single-frequency pulse. It is hard to obtain useful information about the bolt condition from the time-domain signals directly. In this study, the data are analysed in a frequency domain. The power spectral density is calculated using the Welch periodogram for each measurement. Figure 2.7 shows the frequency domain of the signals shown in Figure 2.6. The signal contains frequency components at 110 kHz and 160 kHz. The presence of second harmonics at 220 kHz and 320 kHz and combinational harmonics at 50 kHz, 270 kHz, 380 kHz, and 430 kHz reveal the nonlinear features of the GWs in the frequency domain. By comparing the power spectrum, we can see that the power of the combinational harmonic at the sum frequency, which is 270 kHz, is weaker than that for the signal where the bolt is tightened.

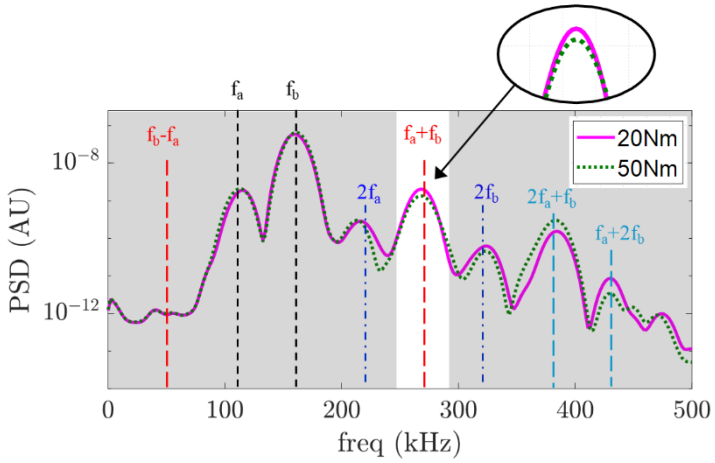

Figure 2.7. PSD comparison between two different applied torques.

Using these two scenarios, we can intuitively predict that when the applied torque is increased from 20 Nm to 50 Nm, the contact interface between the washers and the plates also increases. For the case where the bolted joint is tighter at 50 Nm as compared to the case of 20 Nm, the contact effect produced as a consequence of the guided wave travelling through the bolted joint is lesser for the 50 Nm case; hence, the combinational harmonic for the 50 Nm torque is lower than that for the 20 Nm torque. Given the limitations on second harmonic generation already mentioned in the introduction section, such as the small magnitude of the second harmonic and equipment-related nonlinearities, this study focuses on combinational frequency component, specifically at the sum frequency. In this context, we calculate the power of each measurement for every torque value considered. In fact, it can be observed in Figure 2.8 that there is a relationship between the power of the sum frequency component and the applied torque. For clarity, only 4 of the 11 levels of torque are shown in Figure 2.8.

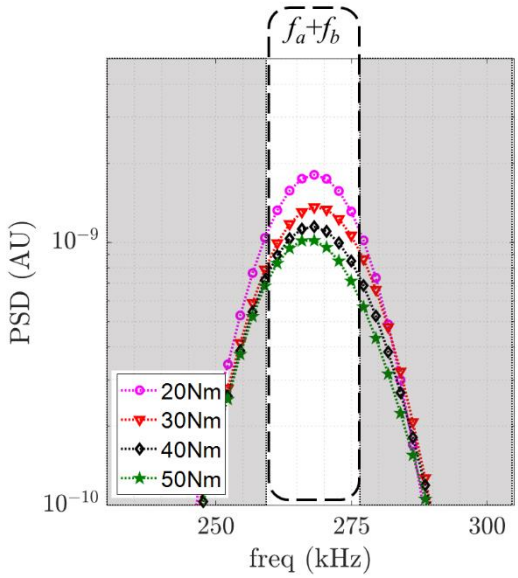

Figure 2.8. PSD comparison between four different levels of applied torque at the sum frequency component.

To further demonstrate the proposed mixed-frequency technique in monitoring bolted joints, the relationship between the applied torque and the areas of power spectral density in the region of the combinational harmonic at the sum frequency within a 32 ± 4 kHz bandwidth were calculated for all five measurements. The averaged values are shown in Figure 2.9. A decreasing trend is notably observed. The results are consistent for all five measurements and show that the proposed approach can be used as an indicator for applied bolt torque.

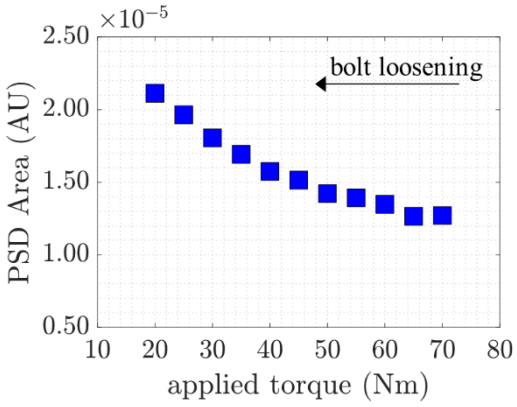

Figure 2.9. Combinational harmonic at sum frequency against applied torque.

As described before, when the bolt is tighter, the contact effect decreases. These steadily decreasing values provide a useful understanding of the nature of the combinational harmonic behaviour when a GW passes through a bolted joint, which provides valuable information for the condition of the applied torque. Moreover, the study also shows that the condition of the joint can be assessed by employing two inexpensive piezoelectric transducers without the need for complicated vibration or impact generator equipment.

2.5 Effect of the number of cycles

In this section, the effect of the duration/number of cycles of the incident wave is investigated. This study was conducted by increasing the number of cycles of the incident pulses. Apart from the signal studied previously (8-cycle 110 kHz signal with a 12-cycle 160 kHz signal), several different sinusoidal tone bursts were generated and measured by the actuator–sensor pair. The pairs consisted of a 6-cycle 110 kHz signal with a 9-cycle 160 kHz signal, an 8-cycle 110 kHz signal with a 12-cycle 160 kHz signal, a 12-cycle 110 kHz signal with a 17-cycle 160 kHz signal, and a 14-cycle 110 kHz signal with a 19-cycle 160 kHz signal. The numbers of cycles were selected so that both single-frequency sinusoidal tone-burst pulses for each pair would have the same duration and have similar energy content. The area under the curve in the power spectrum within a 32 ± 4 kHz bandwidth was calculated for all five frequency pairs. For each of the five frequency pairs, the calculated area values were plotted versus the applied torque in the same way as the previous section and are shown in Figure 2.10.

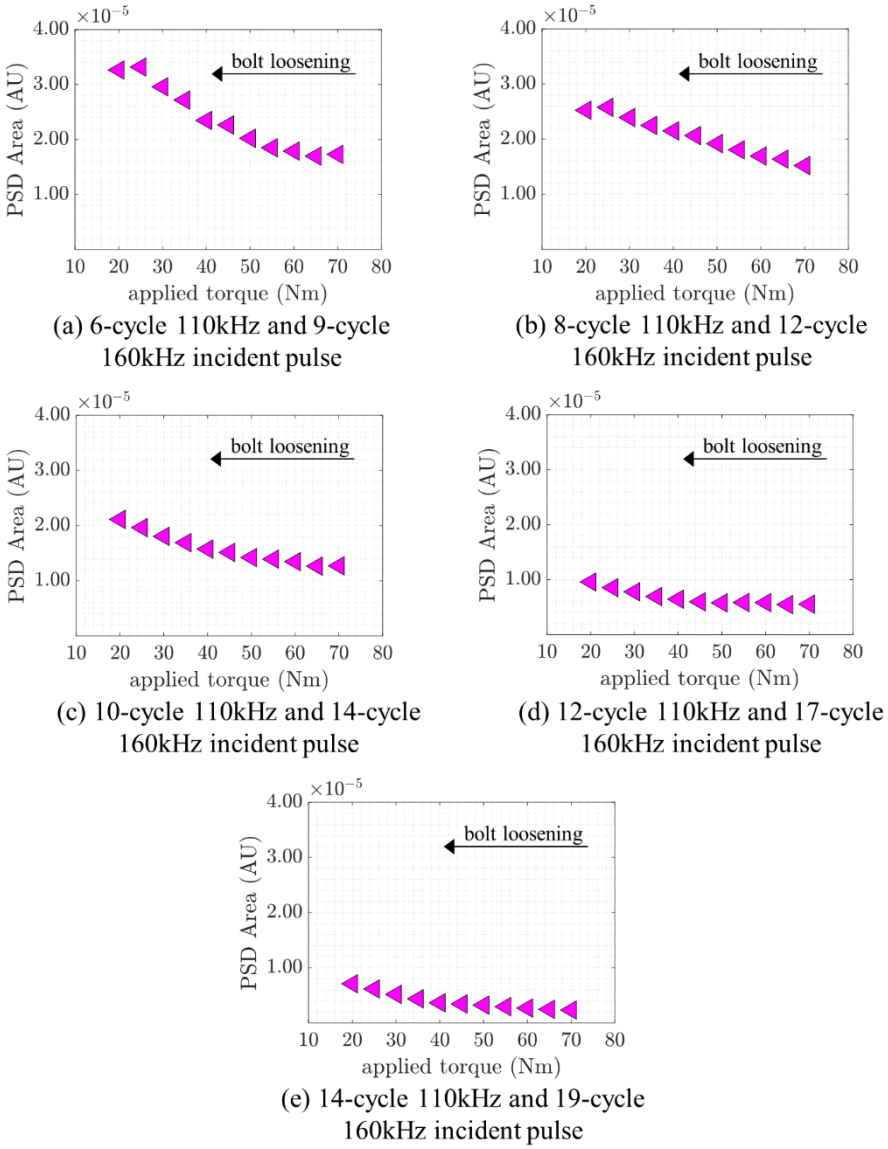

(a) 6-cycle 110kHz and 9-cycle 160kHz incident pulse

(b) 8-cycle 110kHz and 12-cycle 160kHz incident pulse

(c) 10-cycle 110kHz and 14-cycle 160kHz incident pulse

(d) 12-cycle 110kHz and 17-cycle 160kHz incident pulse

(e) 14-cycle 110kHz and 19-cycle 160kHz incident pulse

Figure 2.10. Relationship between PSD area and applied torque.

A decreasing trend is observed for all five frequency pairs. The proposed technique therefore shows that the applied torque in the bolted joint can be used to monitor the mixed-frequency signals regardless of the employed number of cycles. The trend shifts downwards as the number of cycles increases. The explanation for this phenomenon is that the bandwidth of the signal at the sum frequency component becomes sharper when the number of cycles is increased. In turn, when the frequency component reduces its bandwidth, the area under its curve decreases in magnitude, which shifts all values downwards. This

provides a significant insight that even though the proposed monitoring technique is sensitive to the number of cycles, it does not affect its overall performance in monitoring the applied torque using the combinational frequency component.

After processing the signal from all five measurements for each frequency pair, the average values with their respective maximum and minimum values were plotted, as seen in Figure 2.11. The steady decrease for all five cases further demonstrates the robustness of the proposed technique. Particularly, less uncertainty can be observed when the incident pulse is a 14-cycle 110 kHz and 19-cycle 160 kHz wave. In addition, a trend of decreasing variation is observed as applied torque increases. When the bolt becomes loose, many reflections occur as a result of a localized effect, whereas these reflections are less likely to occur and are lesser in magnitude as the torque increases. This phenomenon is echoed in the reduced variation with increasing applied torque.

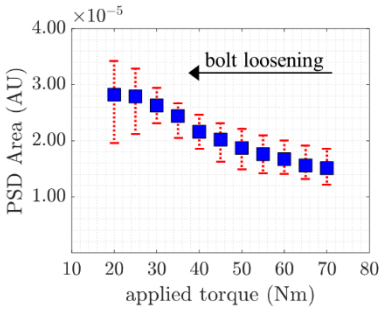

(a) 6-cycle 110kHz and 9-cycle 160kHz incident pulse

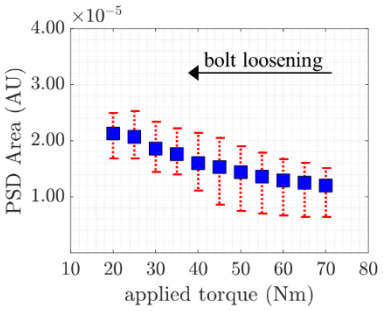

(b) 8-cycle 110kHz and 12-cycle 160kHz incident pulse

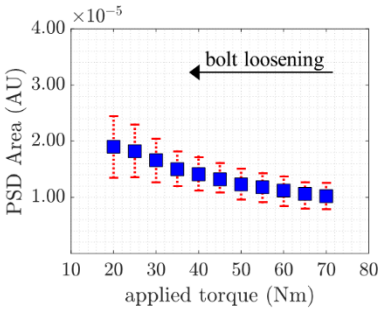

(c) 10-cycle 110kHz and 14-cycle 160kHz incident pulse

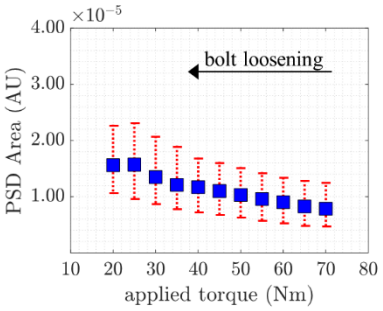

(d) 12-cycle 110kHz and 17-cycle 160kHz incident pulse

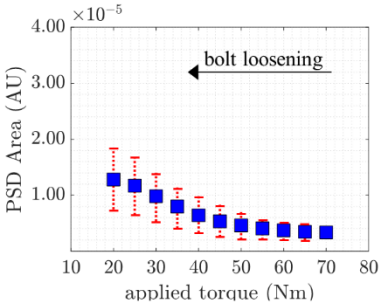

(e) 14-cycle 110kHz and 19-cycle 160kHz incident pulse

Figure 2.11. Mean, minimum, and maximum values of the PSD area against applied torque.

2.6 Conclusions

With the increasing need to detect structural failures or underperformances in civil and mechanical engineering structures, this study has proposed a nonlinear GW-mixing approach to address the bolted-joint monitoring issue in steel plates. A theoretical development has been presented, according to which the applied torque is correlated to the combinational harmonic at sum frequency due to wave mixing. In this study, a signal containing two central frequency components has been used as input signal. The combinational harmonics at sum frequency are induced by contact acoustic nonlinearity of the bolted joints and have been studied under different levels of applied torque. The results show that the frequency spectra of the measured signals carry information on the bolted joint condition. This study has shown that the mixed-frequency signal is sensitive to the applied torque, and the combinational harmonic at sum frequency increases with a decreasing bolt torque, showing that the early bolt loosening can be detected. This study has also demonstrated the effect of the number of cycles of the incident signal on the combinational harmonic at sum frequency. The results show that the correlation between the applied torque and the combinational harmonic at sum frequency of the GW-mixing approach is robust. In addition, by only employing small and inexpensive PZT transducers, this approach could pave the way as a future alternative for online bolted joints monitoring.

2.7 References

1. Zhang, J., N. Ebrahimi, and D. Lai, *Galvanic Corrosion Risk of Using Galvanized A325 Bolts in Corrosion-Resistant Steel Bridges.* Journal of Bridge Engineering, 2019. **24**(6): p. 06019001.
2. Qin, Z., et al., *Design and nonlinear structural responses of multi-bolted joint composite box-beam for sectional wind turbine blades.* Composite Structures, 2018. **206**: p. 801-813.
3. Ye, J., et al., *Efficient design of cold-formed steel bolted-moment connections for earthquake resistant frames.* Thin-Walled Structures, 2020. **150**.
4. Mínguez, J.M. and J. Vogwell, *Effect of torque tightening on the fatigue strength of bolted joints.* Engineering Failure Analysis, 2006. **13**(8): p. 1410-1421.
5. Jhang, K.Y., et al., *Estimation of clamping force in high-tension bolts through ultrasonic velocity measurement.* Ultrasonics, 2006. **44**: p. e1339-e1342.
6. Chaki, S., et al., *Combination of Longitudinal and Transverse Ultrasonic Waves for In Situ Control of the Tightening of Bolts.* Journal of Pressure Vessel Technology, 2006. **129**(3): p. 383-390.
7. Caccese, V., R. Mewer, and S. Vel, *Detection of bolt load loss in hybrid composite/metal bolted connections.* Engineering Structures, 2004. **26**(7): p. 895-906.
8. An, Y.-K. and H. Sohn, *Integrated impedance and guided wave based damage detection.* Mechanical Systems and Signal Processing, 2012. **28**: p. 50-62.
9. Hei, C., et al., *Quantitative evaluation of bolt connection using a single piezoceramic transducer and ultrasonic coda wave energy with the consideration of the piezoceramic aging effect.* Smart Materials and Structures, 2020. **29**(2): p. 027001.
10. Soleimanpour, R., C.T. Ng, and C. Wang, *Higher harmonic generation of guided waves at delaminations in laminated composite beams.* Structural Health Monitoring, 2017. **16**(4): p. 400-417.
11. Hayashi, T., C. Tamayama, and M. Murase, *Wave structure analysis of guided waves in a bar with an arbitrary cross-section.* Ultrasonics, 2006. **44**(1): p. 17-24.
12. Lowe, M.J.S., D.N. Alleyne, and P. Cawley, *Defect detection in pipes using guided waves.* Ultrasonics, 1998. **36**(1): p. 147-154.
13. Ostachowicz, W., et al., *Damage localisation in plate-like structures based on PZT sensors.* Mechanical Systems and Signal Processing, 2009. **23**(6): p. 1805-1829.
14. Lowe, M.J.S. and O. Diligent, *Low-frequency reflection characteristics of the s0 Lamb wave from a rectangular notch in a plate.* The Journal of the Acoustical Society of America, 2002. **111**(1): p. 64-74.
15. Nakamura, N., et al., *Mode conversion behavior of SH guided wave in a tapered plate.* NDT & E International, 2012. **45**(1): p. 156-161.
16. Wang, T., et al., *Proof-of-concept study of monitoring bolt connection status using a piezoelectric based active sensing method.* Smart Materials and Structures, 2013. **22**(8): p. 087001.
17. Tao, C. and et al., *Characterization of fatigue damages in composite laminates using Lamb wave velocity and prediction of residual life.* Compos. Struct., 2017. **166**: p. 219.
18. Amerini, F. and M. Meo, *Structural health monitoring of bolted joints using linear and nonlinear acoustic/ultrasound methods.* Structural Health Monitoring, 2011. **10**(6): p. 659-672.

19. Meyer, J. and D. Adams, *Theoretical and experimental evidence for using impact modulation to assess bolted joints.* Nonlinear Dynamics, 2015. **81**(1): p. 103-117.
20. Zhang, Z., et al., *Quantitative evaluation of residual torque of a loose bolt based on wave energy dissipation and vibro-acoustic modulation: A comparative study.* Journal of Sound and Vibration, 2016. **383**: p. 156-170.
21. Van Den Abeele, K.E.A., P.A. Johnson, and A. Sutin, *Nonlinear Elastic Wave Spectroscopy (NEWS) Techniques to Discern Material Damage, Part I: Nonlinear Wave Modulation Spectroscopy (NWMS).* Research in Nondestructive Evaluation, 2000. **12**(1): p. 17-30.
22. Basu, S., et al., *Nonlinear ultrasonics-based technique for monitoring damage progression in reinforced concrete structures.* Ultrasonics, 2021. **115**: p. 106472.
23. Alnuaimi, H., et al., *Monitoring damage in composite plates from crack initiation to macro-crack propagation combining linear and nonlinear ultrasonic techniques.* Structural Health Monitoring, 2021. **20**(1): p. 139-150.
24. Su, Z., et al., *Acousto-ultrasonics-based fatigue damage characterization: Linear versus nonlinear signal features.* Mechanical Systems and Signal Processing, 2014. **45**(1): p. 225-239.
25. Chillara, V. and C. Lissenden, *Review of nonlinear ultrasonic guided wave nondestructive evaluation: theory, numerics, and experiments.* Optical Engineering, 2015. **55**(1): p. 011002.
26. Lissenden, C., *Nonlinear ultrasonic guided waves—Principles for nondestructive evaluation.* Journal of Applied Physics, 2021. **129**(2): p. 021101.
27. Yang, Y., et al., *Second harmonic generation at fatigue cracks by low-frequency Lamb waves: Experimental and numerical studies.* Mechanical Systems and Signal Processing, 2018. **99**: p. 760-773.
28. Tse, P., F. Masurkar, and N. Yelve, *Estimation of remaining useful life of fatigued plate specimens using Lamb wave-based nonlinearity parameters.* Structural Control and Health Monitoring, 2020. **27**(4): p. e2486.
29. Mohseni, H. and C.T. Ng, *Higher harmonic generation of Rayleigh wave at debondings in FRP-retrofitted concrete structures.* Smart Materials and Structures, 2018. **27**(10): p. 105038.
30. Ng, C.T. and M. Veidt, *Scattering of the fundamental anti-symmetric Lamb wave at delaminations in composite laminates.* The Journal of the Acoustical Society of America, 2011. **129**(3): p. 1288-1296.
31. Yang, Y., C.T. Ng, and A. Kotousov, *Bolted joint integrity monitoring with second harmonic generated by guided waves.* Structural Health Monitoring, 2019. **18**(1): p. 193-204.
32. Hasanian, M. and C. Lissenden, *Second order harmonic guided wave mutual interactions in plate: Vector analysis, numerical simulation, and experimental results.* Journal of Applied Physics, 2017. **122**(8): p. 084901.
33. Hasanian, M. and C. Lissenden, *Second order ultrasonic guided wave mutual interactions in plate: Arbitrary angles, internal resonance, and finite interaction region.* Journal of Applied Physics, 2018. **124**(16): p. 164904.
34. Ishii, Y., S. Biwa, and T. Adachi, *Non-collinear interaction of guided elastic waves in an isotropic plate.* Journal of Sound and Vibration, 2018. **419**: p. 390-404.

35. Li, W., et al., *Theoretical analysis and experimental observation of frequency mixing response of ultrasonic Lamb waves.* Journal of Applied Physics, 2018. **124**(4): p. 044901.
36. Li, W., et al., *Impact damage detection in composites using a guided wave mixing technique.* Measurement Science and Technology, 2019. **31**(1): p. 014001.
37. Jiao, J., et al., *Nonlinear Lamb wave-mixing technique for micro-crack detection in plates.* NDT & E International, 2017. **85**: p. 63-71.
38. Metya, A., S. Tarafder, and K. Balasubramaniam, *Nonlinear Lamb wave mixing for assessing localized deformation during creep.* NDT & E International, 2018. **98**: p. 89-94.
39. Croxford, A., et al., *The use of non-collinear mixing for nonlinear ultrasonic detection of plasticity and fatigue.* The Journal of the Acoustical Society of America, 2009. **126**(5): p. EL117-EL122.
40. Jiao, J., et al., *Micro-crack detection using a collinear wave mixing technique.* NDT & E International, 2014. **62**: p. 122-129.
41. Jiao, J., et al., *Evaluation of the intergranular corrosion in austenitic stainless steel using collinear wave mixing method.* NDT & E International, 2015. **69**: p. 1-8.
42. Nagy, P., *Fatigue damage assessment by nonlinear ultrasonic materials characterization.* Ultrasonics, 1998. **36**(1): p. 375-381.
43. Jhang, K.Y., *Nonlinear ultrasonic techniques for nondestructive assessment of micro damage in material: A review.* International Journal of Precision Engineering and Manufacturing, 2009. **10**(1): p. 123-135.
44. Broda, D., et al., *Modelling of nonlinear crack–wave interactions for damage detection based on ultrasound—A review.* Journal of Sound and Vibration, 2014. **333**(4): p. 1097-1118.

Chapter 3

Debonding Detection at Adhesive Joints using Nonlinear Lamb Waves Mixing

Juan Carlos Pineda Allen and Ching Tai Ng

School of Civil, Environmental and Mining Engineering

The University of Adelaide, SA 5005, Australia

Publication: Pineda Allen, J.C.; Ng, C.T. Debonding detection at adhesive joints using nonlinear Lamb waves mixing. NDT & E International 2021, 125. https://doi.org/10.1016/j.ndteint.2021.102552

Statement of Authorship

Title of Paper	Debonding Detection at Adhesive Joints using Nonlinear Lamb Wave Mixing
Publication Status	☑ Published ☐ Accepted for Publication ☐ Submitted for Publication ☐ Unpublished and Unsubmitted work written in manuscript style
Publication Details	Pineda Allen, J.C.; Ng, C.T. Debonding detection at adhesive joints using nonlinear Lamb waves mixing. NDT & E International 2021, 125. https://doi.org/10.1016/j.ndteint.2021.102552

Principal Author

Name of Principal Author (Candidate)	Juan Carlos Pineda Allen
Contribution to the Paper	Performed literature review, developed numerical model and corresponding cases, developed and prepared the experimental configuration and specimens. Performed numerical simulations and experiments, data processing and analyses, and prepared the manuscript.
Overall percentage (%)	80%
Certification:	This paper reports on original research I conducted during the period of my Higher Degree by Research candidature and is not subject to any obligations or contractual agreements with a third party that would constrain its inclusion in this thesis. I am the primary author of this paper.
Signature	Date: 23/02/2022

Co-Author Contributions

By signing the Statement of Authorship, each author certifies that:

i. the candidate's stated contribution to the publication is accurate (as detailed above);

ii. permission is granted for the candidate in include the publication in the thesis; and

iii. the sum of all co-author contributions is equal to 100% less the candidate's stated contribution.

Name of Co-Author	Ching Tai Ng
Contribution to the Paper	Supervised the work, reviewed the manuscript, prepared for submission and acted as corresponding author.
Signature	Date: 24/02/2022

Name of Co-Author	
Contribution to the Paper	
Signature	Date:

Please cut and paste additional co-author panels here as required.

Chapter 3: Debonding Detection at Adhesive Joints using Nonlinear Lamb Waves Mixing

Abstract

Many engineering structural elements make use of adhesively bonded joints due to its lighter weight, load distribution and transmission mechanisms. The safety of the structure relies greatly on the condition of the adhesive joint. In this paper, the detection of debonding at the adhesive joint is investigated using a nonlinear Lamb wave mixing approach. The method relies on the presence of combined harmonics as indicative of material nonlinearity due to dislocations or anharmonicity in intact specimens or contact nonlinearity produced by the defects. In this study, experiments and three-dimensional finite element simulations were conducted and demonstrated that the presence of combined frequency wave due to contact acoustic nonlinearity is effective for indicating debonding. The effect of the debonding width was investigated and the debonding width was found to correlate well with the combined harmonic energy generated due to debonding. The findings presented in this study provides physical insights into the effect of debonding mechanisms at adhesive joints in related to the nonlinear Lamb wave mixing approach, and can be used to further develop the debonding detection techniques using wave mixing.

Keywords: wave mixing; debonding; adhesive joint; Lamb wave; nonlinear guided wave; combined frequency wave

3.1 Introduction

Layered materials have been commonly used in engineering structures such as aerospace, automotive and civil structures. Adhesive joint is one of the commonly used approaches to manufacture layered structural elements [1, 2] and conduct repairs and reinforcement where light weight is of paramount concern [3]. This type of joint has the advantage of avoiding stress concentration by uniformly distributing the stresses. Lighter weights can also be achieved as compared to traditional mechanical joints. The performance of layered materials greatly relies on the adhesive layer. In the manufacturing process, this layer is susceptible to air inclusions or weak bonding strength. During service stage, delamination or debonding caused by impact or fatigue could lead to catastrophic failure of structures. These manufacturing defects and structural damage are not always visible and hard to be detected by visual inspection, therefore, non-destructive testing techniques were developed to inspect and detect these defects and damages without the need to dismantle the real structure.

In many applications, ultrasonic non-destructive testing methods have advantages compared to other non-destructive testing methods as they possess the ability to mechanically probe the defect. Moreover, ultrasonic guided waves have the potential of being suitable for in-situ inspection and monitoring of plate-like and pipe structures. Ultrasonic piezoelectric wafer transducers can be permanently installed on structures and the inspection and monitoring process do not affect operation of the structures and do not require the presence of a technician for on-site operation [4-6].

3.1.1 Nonlinear phenomena of ultrasonic guided waves

Linear ultrasonic techniques can be used to detect micro-scale defects and damages, such as local bonding degradation, distributed micro-cracks, and

delamination. Nonlinear ultrasonics has the advantage that is more sensitive to smaller size of damage and can detect damage at an earlier state [7]. Detection of these defects and damages are critical for safety inspection and providing early warning. Nonlinear ultrasonics has attracted considerable attention [8] in the past years. This approach relies on nonlinear acoustic phenomena, where nonlinear responses of ultrasonic wave, e.g. higher order harmonics, are generated due to interaction between the incident wave and discontinuities. Higher order harmonic generation can be induced by material nonlinearity due to dislocations or anharmonicity in intact specimens [9, 10] or contact acoustic nonlinearity (CAN) produced by defects [11-13].

Second order harmonic (or simply second harmonic) generated due to material nonlinearity was proven to be capable of detecting microstructural changes, such as plasticity [14] and mechanical fatigue [15] in metallic specimens, and thermal fatigue damage in composites laminates [16]. CAN was investigated for detecting fatigue cracks in metals [17], delamination in composites laminates [18, 19] and debonding in adhesive joints [20] as well as in FRP-retrofitted concrete structures [21]. Adhesive nonlinearity may also generate contact nonlinearity [22].

Despite recent advances, some limitations remain challenging for second harmonics generation techniques. The nonlinearities induced by contact between the structure components under inspection and the ultrasonic transducer can mask the damage-related and material nonlinearities. Secondly, the relatively small magnitude of the higher harmonic is hard to be measured accurately. Lastly, nonlinearities are also introduced by the testing equipment compromising the isolation of the source of the nonlinearity.

To overcome these drawbacks, the wave mixing method utilizing two ultrasonic waves at different single central frequencies has been developed in last few years [23, 24]. Wave mixing method can be primarily classified as collinear [25] and non-collinear [26] depending on the wave propagation angle between

the incident waves. Foreseeing its advantages, mixed-frequency response is the focus of this paper.

3.1.2 Nonlinear mixed-frequency response

Jingpin *et al.* employed collinear wave mixing of bulk waves to study inter-granular corrosion [27] and micro-crack [28] in steel specimens. They also investigated bulk shear wave mixing and non-collinear wave mixing to determine the presence of fatigue cracks [29]. Two-dimensional finite element (FE) method was applied to demonstrate the potential of non-collinear mixing method in detecting closed cracks using bulk shear waves [30]. A time and frequency domain analysis of a slender beam was used to determine crack location with the consideration of dispersion characteristics [31]. Croxford *et al.* [26] employed bulk waves to characterize material nonlinearity due to fatigue and plasticity damage using the non-collinear method. Material nonlinearity was experimentally correlated to plastic deformation of aluminium alloy. An independent nonlinear acoustic parameter using collinear wave mixing of bulk waves, which is strictly related to plastic deformation, was introduced and validated numerically and experimentally [32]. Further experimental studies demonstrated that the collinear method can also measure localized plastic deformation [33]. The bulk waves employed in the aforementioned studies are limited to a very localized inspection area.

Compared to ultrasonic bulk waves, guided waves (Lamb waves) offer advantages such as the ability to inspect inaccessible locations. Specific wave modes can be appropriately selected and generated, even though mainly the fundamental modes were used in long range measurements. Their applications to submerged elements or structures with one side exposed to fluids were investigated [34-36], although to date, viscoelasticity constraints and the Cremer's correspondence principle still limit its further development.

Collinear and non-collinear plane wave mixing was investigated by Hasanian *et al.* [37, 38]. Ishii *et al.* [39] theoretically analysed nonlinear wave propagation in a homogenous and isotropic plate. They elucidated the non-collinear interaction of monochromatic plane waves employing a perturbation analysis and infinite beam widths. They also conducted FE analysis considering finite beam width and time durations to gain further understanding on the scattered wave generation. Further studies were carried out to advance understanding of counter-propagating guided waves [40, 41]. Li *et al.* [42] studied mixed-frequency response induced by collinear codirectional Lamb waves and predicted the generation of second and third order combined harmonics. They also investigated impact damage detection [43]. Codirectional Lamb wave mixing was used to investigate micro crack [44] and localized creep detection in steel plates [45] and thermal related microstructural changes in aluminium plates [46]. Distributed micro-cracks were also investigated using codirectional Lamb wave mixing and FE modeling [47].

For the two aforementioned higher harmonic generation mechanisms, CAN is the focus in this paper. It has potential to detect debonding in layered structures using wave mixing technique. Different to finding triplets and exploring the cumulative nature of the secondary wave as in Refs. [43, 47, 48], we numerically and experimentally investigate CAN due to the clapping mechanisms at the debonded layer when Lamb wave propagates through the plate and generates combined harmonic, and hence, the internal resonance conditions are not assessed in this paper.

3.1.3 Damage detection of adhesive joints using guided waves

The applications of linear Lamb waves for detecting damage in adhesive joints were initially employed to study lap shear joints [49] and explored the use of the anti-symmetric (A_0) mode of Lamb wave for characterization due to its sensitivity

and dominant out-of-plane displacement over its in-plane displacement [50]. Some other studies investigated the use of root-mean-square and non-contact sensing for damage imaging of adhesive joints [51]. The contact phenomenon was investigated for detecting delamination in composites laminates using time domain signals and mode conversion features [52]. Wavenumber analysis was employed to locate and quantify delamination based on trapped energy from the wave [53]. However, these studies only focused on the linear Lamb waves.

More recently, nonlinear guided waves were used to identify the existence of delamination across different plies in composite beams [19]. Yelve *et al.* [18] employed a spectral damage index to correlate with delamination size and a time-frequency method to further determine delamination location. But these studies only focused on higher harmonics generated due to single frequency wave interacting with CAN.

Existing studies focusing on wave mixing phenomenon of adhesive bonds [54-56] were limited to the bulk wave. However, bulk wave interaction is different to wave interaction in plate-like structures as pointed out by de Lima *et al.* [57] and Hasanian *et al.* [37]. Therefore, our study is to investigate a different type of wave mixing, specifically guided waves as their interaction has not yet been fully understood. To date, research on Lamb wave mixing techniques is still very limited, in particular, the Lamb wave mixing phenomenon at debonding in layered materials needs to be investigated. The objective of this paper is to investigate the Lamb wave mixing for detecting local debonding at adhesive joints using three-dimensional (3D) FE simulation and experiment. Debonding detection remains a challenging area in the non-destructive testing community given that debonding (and alike) defects mostly locate under the surface of the structural component, deriving in long inspection times if inspected with traditional point-to-point ultrasonics. By using ultrasonic guided waves, the time of inspection can be reduced as the inspection can be more effective due to the relatively long propagation inspection distance of guided waves. This can

minimize labour related costs. The experimental and numerical studies conducted in this paper help gain insight into the combined harmonic wave generation due to guided wave mixing and interaction with debonding. It further demonstrates that the combined harmonic wave generation due of wave mixing and interaction with debonding can be reliably measured in experiments. Unlike most research in guided wave mixing to date where simplified plane strain models were used, the 3D FE model in this paper ensures the characteristics of the wave can be fully captured and well correlated to the experimental data. The findings of this study help further advance the use of wave mixing for damage detection and characterization.

This paper is organized as follows. Section 2 introduces the Lamb wave mixing phenomenon. Section 3 presents the experimental framework, where the specimen preparation and actuating/sensing set up are described. The theoretically and experimentally obtained dispersion curves are compared and validated. Section 4 describes the details of the FE simulation. The FE model is validated theoretically and experimentally in this study. In Section 5, a series of case studies on Lamb wave mixing and interaction with debonding are presented experimentally and numerically. The effect of debonding size on combined harmonic wave generation is investigated in Section 5. Finally, conclusions are presented in Section 6.

3.2 Lamb wave mixing phenomenon

When two or more propagating waves with different central frequencies interact with a linear system, only incident frequencies will exist in the frequency spectrum of the response. However, when interacting with a nonlinearity source (damage or material related), the total response comprises a linear response, higher harmonics and combined harmonics. This is schematically represented in Fig. 3.1. For a linear system, the frequency spectrum u of the time domain

response only contains the incident frequencies f_a and f_b. Conversely, the spectrum of the response after interaction with a nonlinear system additionally contains higher harmonics $2f_a$ and $2f_b$, and combined harmonics $f_b - f_a$ and $f_a + f_b$.

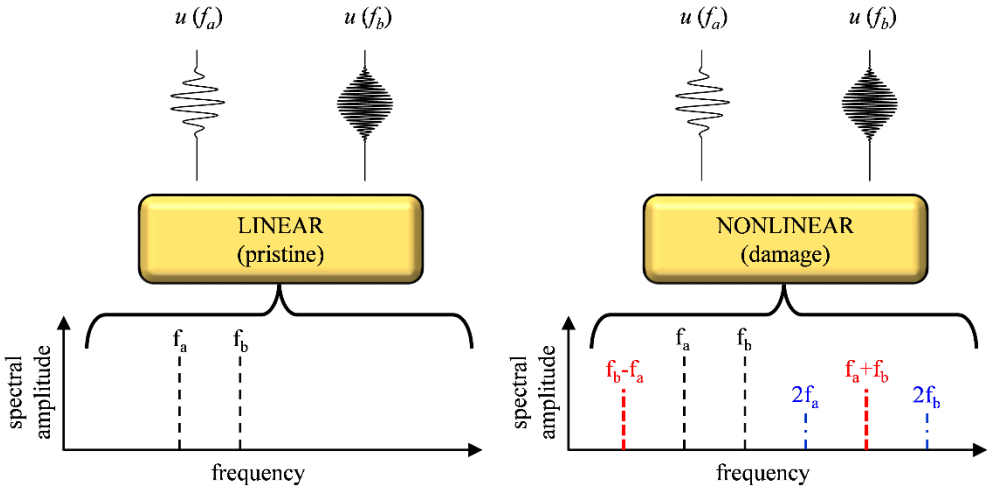

Figure 3.1. Schematic representation of wave-mixing phenomena in linear and nonlinear system

The existence of combined harmonics, specifically the combined frequency wave at the sum harmonic frequency for collinear Lamb wave mixing, and its sensitivity to damage in adhesive joint are experimentally and numerically investigated in this paper. In the rest of the paper, the combined frequency wave at the sum harmonic frequency refers to combined frequency wave unless there is a specific indication on the frequency.

3.3 Experiment

3.3.1 Specimen Description

Specimens used in this study consist of three layers of elements, which are two grade 6061-T6 aluminium plates and one epoxy layer. The dimensions of the two aluminium plates are 300mm × 100mm × 1.02 mm and 300mm × 100mm × 1.60 mm. The plates were cleaned with acetone to remove any impurities and oil, and

then, treated with sandpaper and cleaned with acetone again to remove any dust before applying the epoxy resin to bond them together. The epoxy is a two-part adhesive glue MBrace 4500. Distributed weights were placed on the top of the specimen to ensure equal pressure was applied in the drying process. Although it is difficult to control rigorously the thickness of the glue layer during the curing process, an average thickness of 0.20 mm was obtained once the epoxy layer fully dried and hardened. A digital calliper was used to measure the total thickness of the specimen every 50 mm all around its perimeter.

Three specimens were prepared. One of the specimens was fully bonded, and the other two specimens have debonding and were prepared as follows. For the second specimen, the epoxy resin was not applied to a strip area of approximately 10 mm wide and parallel to the shorter side of the plate in order to create a weak bonding in the specimen after the top and bottom plate were bonded together. For the third specimen, a 10 mm wide Mylar strip was inserted during the epoxy resin application. In the second and third specimens, both modifications were done at the centre of the longer side of the specimens as schematically shown in Fig. 3.2. The purpose of the Mylar insert and the epoxy absence is to create a weak bonding region in the specimens. To induce debonding at the weak bonding region, a three-point bending test under cyclic load was conducted. The bottom plate on the support is a 1.02 mm thick plate while the top plate is 1.60 mm thick. The load was applied on the top surface of the top plate so that the epoxy resin layer was subjected to tensile stress during the bending test.

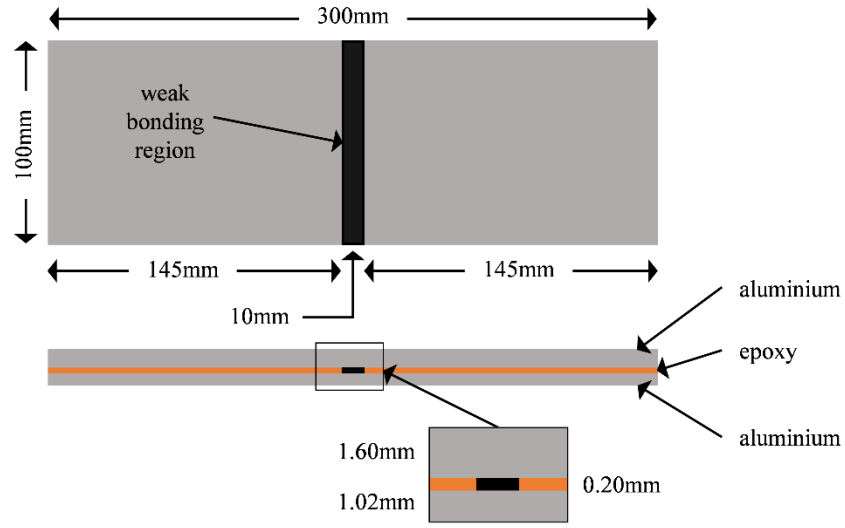

Figure 3.2. Schematic diagram of the adhesively bonded specimen

3.3.2 Equipment setup

A wedge made of Teflon was designed and used with a transducer to generate A_0 Lamb wave. Longitudinal velocity of the Teflon is 1336.37 m/s, the incident angle is calculated using Snell's law. A number of different wedges and two different contact transducers, ULTRAN GC200-D13 and GC350-D13, were used in the experiment. A special fixture was 3D-printed to assemble the transducer to the wedge as shown in Fig. 3.3. Light motor oil was applied at the wedge-specimen interface and the wedge was fixed on the top of the specimen by a clamp. Reflective paint was applied to the specimen surface to increase the optical backscatter reflection of the laser beam. The measured signals were averaged 1000 times and passed through a low-pass filter to increase the quality of the measurements. The signal averaging was to improve the signal to noise ratio by minimizing the measurement white noise. A one-dimensional (1D) scanning Laser Doppler Vibrometer (SLDV) was used to measure the displacement response of the wave. Even though the 1D SLDV could possess a limitation in capturing a symmetric wave mode, previous studies showed the amplitude of the symmetric wave mode generated due to debonding type of

damage is usually weak. For practical application, piezoceramic transducers can be used to measure the wave signals. However, this study aims at investigating the wave mixing phenomenon so the 1D SLDV was used to provide enough flexibility on the measurement location, and hence, the wavenumber-frequency analysis can provide further understanding on the wave phenomenon. A PC-controlled NI PXI-5412 arbitrary function generator was used to generate the incident pulse. The signal was then amplified by a CIPRIAN HVA-800-A amplifier. Fig. 3.4 shows the experimental setup used in this study.

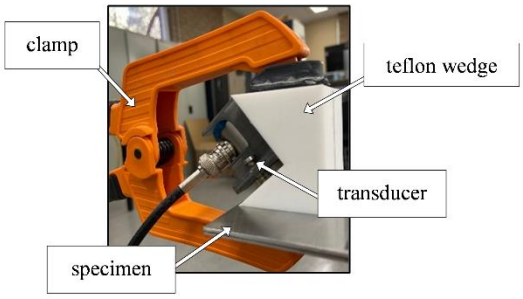

Figure 3.3. Wedge-transducer-specimen assembly

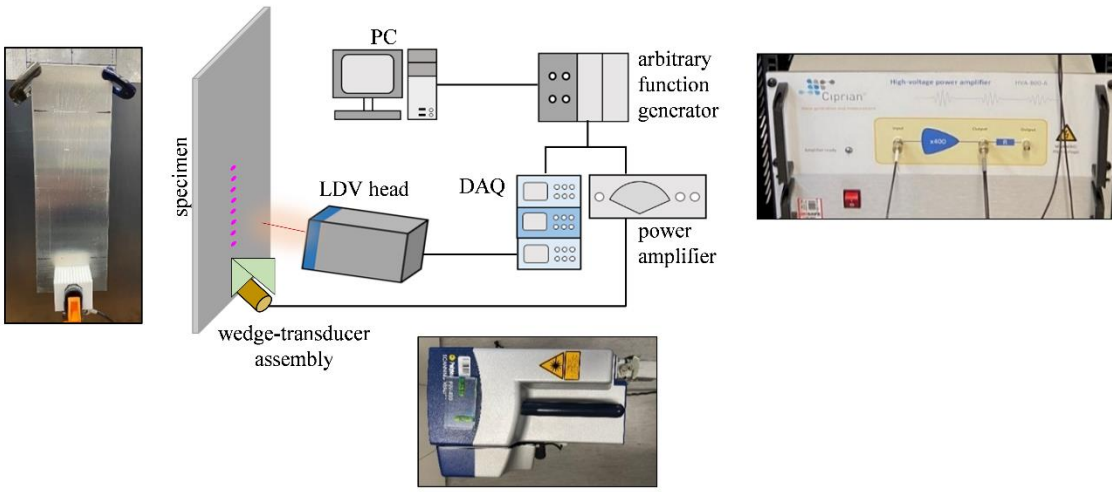

Figure 3.4. Schematic diagram of the experimental setup

3.3.3 Experimentally measured dispersion curves

A number of tests were first conducted to validate the dispersion curves with theoretical solutions. The fully bonded specimen was used in the tests. Eight independent sinusoidal tone-burst pulses with different central frequencies ranging from 150 kHz to 500 kHz in steps of 50 kHz were excited and a line scan of 41 consecutive points with 1 mm distance between points was conducted for each excitation frequency. Eight different wedges corresponding to the eight different phase velocities were used. Each wedge was designed using the corresponding Snell's angle, which are 57°, 50°, 46°, 43°, 41°, 39°, 38° and 37° for the 150 kHz, 200 kHz, 250 kHz, 300 kHz, 350 kHz, 400 kHz, 450 kHz and 500 kHz pulses respectively. Out-of-plane displacement response of the specimen was measured for each line scan and recorded for further processing. Frequency-wavenumber (*f*-*k*) by means of two-dimensional Fourier transform algorithm and frequency-group velocity (*f*-c_g) were calculated for each of the tests.

For a Lamb wave propagating on plate along the x direction, the displacement on the surface can be described by the general analytical expression [58],

$$u(x,t) = A(\omega)e^{i(kx-\omega t-\varphi_0)} \tag{1}$$

where A is the amplitude, ω is the angular frequency, φ_0 is the phase. The wavenumber k is given by $k = \omega/c_p$, for a wave with phase velocity c_p. The two-dimensional transform is given by,

$$H(k,f) = \int\int u(x,t)e^{-i(kx-\omega t)}dxdt \tag{2}$$

In most of the measured Lamb wave signals, more than one propagating Lamb mode exist and travel simultaneously, which hinders the straightforward calculation of phase and group velocity. The graphical representation of the two-dimensional Fourier transform helps identify different propagating modes and it needs data measured at multiple measurement locations. We employed the laser scanning vibrometer to achieve non-contact measurement of the Lamb

wave signals at multiple measurement points. The group velocity was calculated using the time-of-flight of the signal envelope obtained from the Hilbert transform and distance between consecutive measurement points. Theoretical dispersion curves were calculated using DISPERSE under the assumption that the wavefront is an infinite plane and normal to the direction of wave propagation. Material properties used to calculate dispersion curves of the epoxy and aluminium are density $\rho_e = 1200$ kg/m^3 and $\rho_a = 2704$ kg/m^3, Young's modulus E_e = 3.70 GPa and E_a = 69 GPa, and Poisson's ratio ν_e = 0.40 and ν_a = 0.33, respectively. A contour plot of the calculated frequency-wavenumber array and group velocity values for the fully bonded specimen are shown in Fig. 3.5, where the theoretical values are represented by continuous black lines. A_0, S_0, and higher order modes are not antisymmetric or symmetric because the specimens are not symmetric in the thickness direction. Given the accepted terminology in the existing literature, the authors keep the terms "A" and "S" for the antisymmetric and symmetric modes of Lamb waves, respectively.

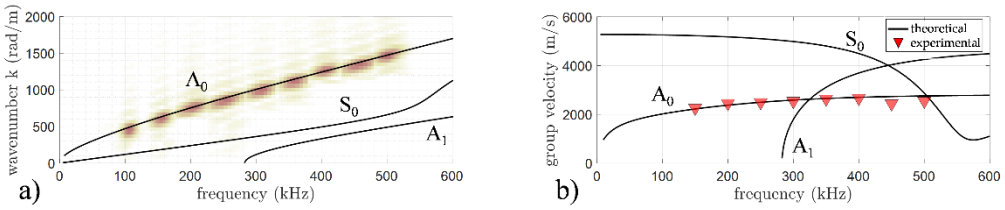

Figure 3.5. Experimentally obtained and theoretically calculated a) frequency-wavenumber and b) group velocity dispersion curve

3.4 3D finite element simulation

3.4.1 Model description

A 3D FE model was developed to simulate the mixed frequency Lamb wave propagation. Although a one-dimensional model has less computational cost, a 3D FE model was employed in this study to ensure the FE prediction is highly

accurate, in particular capturing the wave attenuation effect in the wave propagation and the non-plane wavefront effect of the generated wave. The FE model is experimentally verified and used to gain physical insights into the wave mixing phenomena and interaction with the debonding. The model has three layers, whose top and bottom layer are grade 6061-T6 aluminium plate and mid layer is an epoxy layer with density ρ = 1200 kg/m^3, Young's modulus E = 3.70 GPa and Poisson's ratio ν = 0.40. Even though a nonlinearity coefficient beta is of the same order for the epoxy and aluminium, a linear behaviour of the epoxy layer was assumed because the epoxy layer is thin as compared to the aluminium layers. The assumption was further corroborated when validating the FE model results and the experimental results. Eight-noded brick elements, C3D8R, with each node having three translational degrees-of-freedom and reduced integration were used [59]. The maximum element size was set to 0.20 mm to ensure there are at least 20 elements within the shortest wavelength of interest. There are five element layers for the 1.02 mm thick aluminium plate, two element layers on the epoxy and eight element layers for the 1.60 mm thick plate. The increment time step was automatically controlled by ABAQUS/Explicit. Mechanical constitutive behaviour based on the nonlinear strain energy function of Murnaghan was modelled in ABAQUS/Explicit through a VUMAT subroutine to simulate the material nonlinearity [60]. The material properties of the plates are listed in Table I. Adhesive bond between aluminium layers and epoxy layer is assigned by using tie constraints.

Table 3.1. Material properties used in the FE simulations [61]

Density (kg/m^3)	E (GPa)	ν	l (GPa)	m (GPa)	n (GPa)	λ (GPa)	μ (GPa)
2704	69	0.33	-281.50	-339.00	-416.00	54.30	27.30

3.4.2 Absorbing layers

Absorbing layers by increased damping (ALID) was implemented in the FE model to avoid the wave reflected from the edges of the plate. ALID contains layers with increasing value of damping so that the energy of the Lamb wave is gradually absorbed when approaching the ALID at the edges of the plate. This significantly reduces the computational cost of the FE simulations, and hence, the model is computationally efficient for investigating the Lamb wave propagation and interaction at the debonding. The ALID was modelled at all perimeters of the plate. The ALID have 100 layers, each has 0.5 mm wide, making the total width of the ALID to be 50 mm. In this study, mass proportional damping was used to model the ALID. The damping value of at each ALID layer is obtained by the following power-law formulation [62]:

$$C_M(x) = C_{max} \times X(x)^P \tag{3}$$

where x is the location between the edge of the plate without the ALID and the ALID itself, $P = 3$ and $C_{max} = 2.5 \times 10^6$. The total in-plane dimensions of the model with the ALID is 400 mm × 250 mm.

3.4.3 Numerically calculated dispersion curves

A_0 Lamb wave is excited by applying out-of-plane nodal displacement at the top and bottom nodes in a region of the transducer. Firstly, eight simulations with the identical FE model but different central frequencies of the incident pulse were used. Each incident signal is a Hanning-windowed tone burst pulse with central frequency ranging from 150 kHz to 500 kHz in steps of 50 kHz. Out-of-plane displacement response u_t at the top surface of the three-layered plate model was calculated at 41 consecutive points with 1 mm spacing. Frequency-wavenumber (f-k) and frequency-group velocity (f-c_g) were calculated for each of the simulations. A contour plot of the FE calculated frequency-wavenumber and

group velocity values are shown in Fig. 3.6, where the theoretical values are represented by continuous black lines.

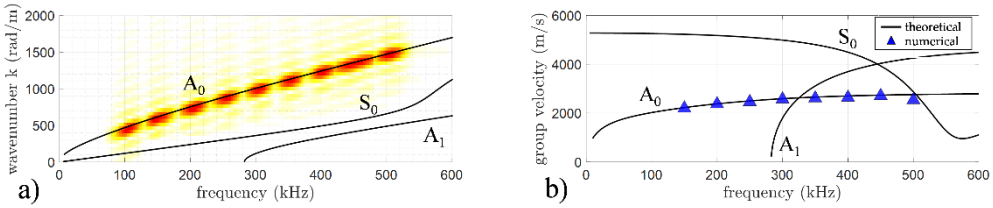

Figure 3.6. Numerically and theoretically calculated a) frequency-wavenumber and b) group velocity dispersion curve.

The results confirm the dispersion characteristics of the FE model of the fully bonded specimen are able to represent the A_0 Lamb wave propagation. Due to the multi-modal characteristics of Lamb waves, the use of the fundamental modes below the cut-off frequency is preferred. In this study, the cut-off frequency is 285 kHz. Research demonstrated that incident antisymmetric Lamb waves have great sensitivity to delamination [19], debonding [63] and low velocity impact damage [64] given its quasi-flexural propagation nature. They also have better capability of detecting small discontinuities in the propagating media given their shorter wavelengths comparing to symmetric Lamb waves at the same frequency. Therefore, incident A_0 mode was chosen in this study to explore the interaction of the antisymmetric Lamb wave with the local debonding.

3.5 Experimental and numerical wave-mixing case studies

Ten case studies were carried out experimentally and numerically. Different specimens, FE models and excitation frequencies were considered in these case studies. The purpose of these case studies is to explore the feasibility and reliability of using wave mixing approach for detecting debonding in layered

structures. The case studies are summarized in Table II. Case E1 considered a fully bonded specimen under A_0 incident Lamb waves with frequencies 150 kHz and 250 kHz, named f_a and f_b, respectively. In Case E2, 200 kHz and 300 kHz were used as excitation frequencies for the fully bonded specimen. Case E3 considered a specimen with debonding, and 150 kHz and 250 kHz excitation frequencies. Case E4 used the same specimen, but the excitation frequencies were 200 kHz and 300 kHz. The remaining specimen with debonding was used in Cases E5 and E6, which consider different excitation frequencies. Fully bonded FE model was used in Cases N1 and N2. Cases N3 and N4 considered FE models with a debonding.

To model the debonding, tie constraints were removed between the aluminium and epoxy layer along a 10 mm width strip parallel to the shorter side of the model. To avoid interpenetration between debonded surfaces so that the CAN effect can be simulated, a hard contact and surface-to-surface contact interaction is implemented in the FE model. The strip was located at the centre of the plate. The incident signal consists of a tone burst pulse composed of two sinusoidal pulses with different central frequencies, or in other words, two sinusoidal tone burst pulses with different central frequencies were created separately and then merged to generate a single excitation signal. The number of cycles of the excitation signals was selected so that the durations of the pulses are the same, they are 8 cycle for 150 kHz, 13 cycle for 250 kHz, 10 cycle for 200 kHz and 15 cycle for 300 kHz. The mixing zone is approximately 86 mm. Frequencies selection was based on two main reasons, on the one hand to take advantage of the operative frequency bandwidth of the used transducers, and on the other hand, such as the combined frequency wave was not multiple of any of the input frequencies. Since generated signals have different group velocities, further numerical simulations, which are not presented in this paper, have indicated they are separated at approximately 450 mm. For the additional simulations, an 8-

cycle 150 kHz pulse was actuated first, then an independent 13-cycle 250 kHz pulse, and lastly both pulses concomitantly.

Table 3.2. Experimental and numerical Lamb wave mixing case studies

	Case	Specimen	Incident frequencies	
			f_a (kHz)	f_b (kHz)
Experimental Study	E1	fully bonded	150	250
	E2	fully bonded	200	300
	E3	debonded (mylar inserted at debonding region)	150	250
	E4	debonded (mylar inserted at debonding region)	200	300
	E5	debonded (no epoxy applied at debonding region)	150	250
	E6	debonded (no epoxy applied at debonding region)	200	300
Numerical Study	N1	fully bonded	150	250
	N2	fully bonded	200	300
	N3	debonded (untied constraints at epoxy layer in the debonding region)	150	250
	N4	debonded (untied constraints at epoxy layer in the debonding region)	200	300

A similar experimental setup used in the previous section was employed for the wave generation and data acquisition (Figs. 3.3 and 3.4). However, different set of wedges were used in this section. A 52° Teflon wedge with the GC200-D13 transducer actuated the 8-cycle 150 kHz and 13-cycle 250 kHz pulse. In contrast, the GC350-D13 transducer with the 46° Teflon wedge was used to actuate the 10-cycle 200 kHz and 15-cycle 300 kHz pulse. Wedges were chosen considering either (a) the average angle of the two Snell's angles of the two incident frequencies, or (b) the Snell's angle corresponding to the average frequency value of the two incident frequencies. Using the SLDV, the out-of-

plane displacement was measured at a point located 60 mm from the centre of the debonding region in the forward propagating direction. To improve the signal-to-noise ratio, the measured signals were averaged 1000 times and pass through a low-pass filter. The signal averaging is to improve the signal to noise ratio by minimizing the measurement white noise. In the FE model, top out-of-plane displacement for nodes located at 60 mm from the debonding centre in the forward propagating direction were calculated. A snapshot of the displacement response of the FE model with debonding when the incident A_0 Lamb wave interacts with the debonding (Case N3) is shown in Fig. 3.7a. The figure also shows a zoom-in of the cross-section along the Z axis at the debonding region. To investigate the harmonic generation in the measured signals from the experiments and FE models, the Fast Fourier Transform was used to transfer the data from time domain to frequency domain for all cases (Cases E1 to E6 and N1 to N4), and the results are shown in Fig. 3.9.

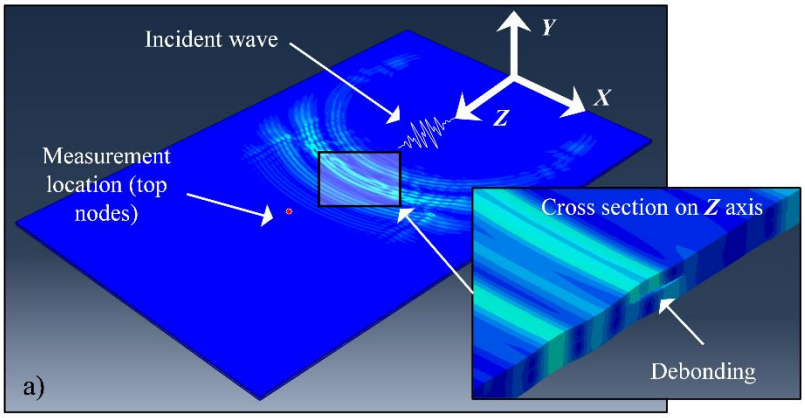

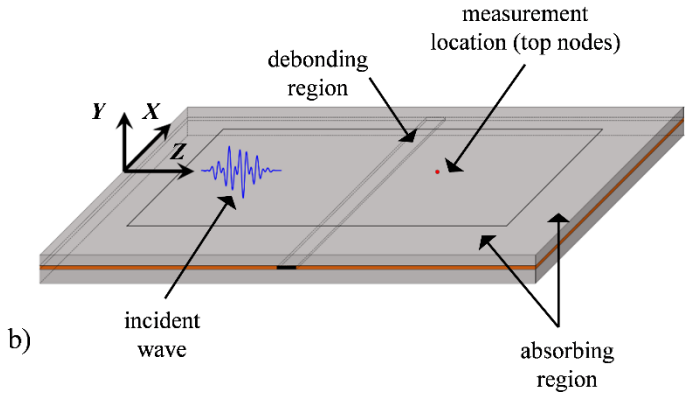

Figure 3.7. a) Snapshot of the A_0 Lamb wave interacts with debonding, b) Schematic layout of the debonding plate with debonding.

Two preliminary numerical cases (not listed in Table II) were first conducted to confirm the combined frequency wave is A_0 mode, one case for the fully bonded model and the other case for the debonded model. The out-of-plane displacement for a total of 41 points separated every 1 mm were calculated. In Fig. 3.8, the frequency-wavenumber curves for the two cases are shown. It is noted that the generated combined frequency wave due to debonding corresponds to the A_0 mode as expected.

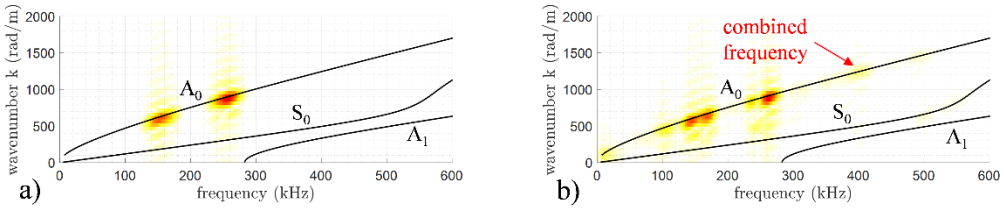

Figure 3.8. Frequency-wavenumber a) fully bonded, b) debonded

We continue the study with the cases listed in Table II. Fig. 3.9a shows the spectral content of incident frequencies at 150 kHz and 250 kHz. The results show that additional frequency components appear for signals obtained from the debonded specimens in experiment and FE simulation. Higher harmonics and combined harmonics, including the combined frequency wave $f_a + f_b$ can be

observed. These harmonics can be associated with material nonlinearity and nonlinearity generated by CAN. However, CAN-induced harmonics by debonding are expected to be much larger than material nonlinearity-induced harmonics [7, 65]. Similar phenomenon is observed in Fig. 3.9b when 200 kHz and 300 kHz were the central frequencies of the incident wave signal, which reveals the frequency components at 500 kHz. The combined frequency wave at the difference harmonic frequency is also observed, mostly for the 200 kHz and 300 kHz pulse. This is not obvious for the 150 kHz and 250 kHz pulse, as the combined frequency at the difference harmonic frequency is masked by the 150 kHz component.

The results indicate that mixed frequency response is effective for local debonding detection at adhesive joints, which do not have any obvious visual evidence on the surface as it is internal damage. The results show that there is good agreement on the experimentally measured and numerically calculated combined frequency wave induced by the debonding. Therefore, the 3D FE model can provide reasonable accuracy in predicting the combined frequency wave in wave mixing.

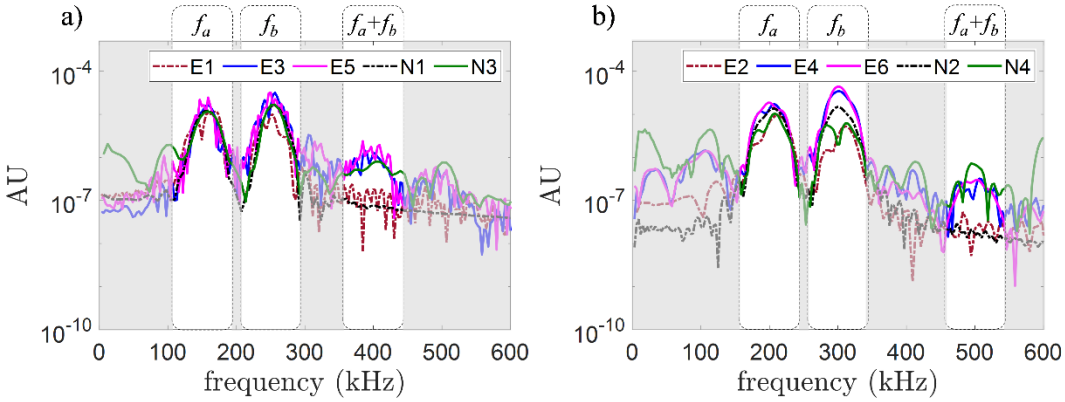

Figure 3.9. Experimentally measured and numerically calculated Fourier spectra for a) 150 kHz and 250 kHz, and b) 200 kHz and 300 kHz incident frequencies

3.6 Effect of debonding size

In this section, the experimentally verified FE model was used to provide a parametric study to investigate the effect of debonding size on the combined harmonics. Sixteen cases with different debonding length-to-wavelength ratios, d/λ, were considered. They are summarized in Table III and a schematic diagram is shown in Fig. 3.7b. λ is the wavelength of the combined frequency wave of the A_0 Lamb wave. The centre of the debonding region is located at 100 mm from the excitation location, and the measurement points are located at 60 mm from the debonding centre in the z direction.

Table 3.3. Summary of debonding length-to-wavelength ratios considered

d/λ	0.125	0.250	0.375	0.500	0.625	0.750	0.875	1.000
d/λ	1.125	1.250	1.375	1.500	1.625	1.750	1.875	2.000

Frequency pair of 150 kHz and 250 kHz was selected in this study. Out-of-plane nodal displacements at the top of the model were calculated for each of the simulations. A typical time domain response for the cases of models having a debonding with $d/\lambda = 1.00$ and $d/\lambda = 2.00$, and fully bonded model are shown in Fig. 3.10a. The corresponding frequency spectra are shown in Fig. 3.10b. It can be observed that the response is distorted due to the debonding. Additionally, a shift in energy content from the incident wave to the generated pulse within the debonding is expected from the observation of the maximum displacement. The time-frequency analysis in Fig. 3.11 also reveals information of the combined frequency wave.

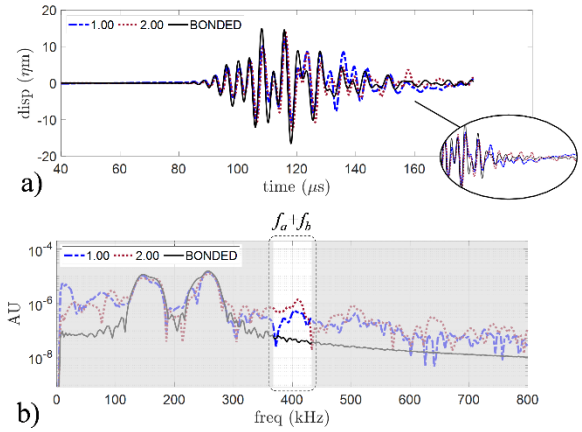

Figure 3.10. Typical a) time domain and b) frequency spectra of displacement responses measured at 60 mm from debonding region.

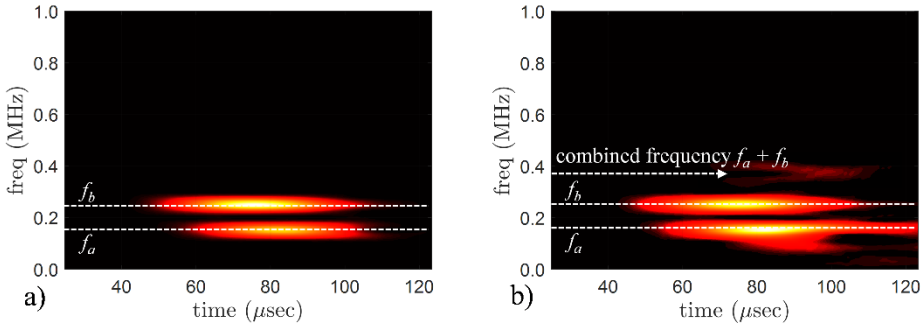

Figure 3.11. Time frequency spectrum for a) fully bonded specimen and b) case with d/λ = 2.00 debonding.

Previous research investigated time domain features of the response to analyse contact mechanisms in composites laminates [52, 66]. However, analyses were conducted using single frequency pulses with the mode conversion phenomenon. The converted modes are able to travel long enough distances and the newly converted modes can separate from the incident waves once it interacts with the damage. However, for mixed-frequency analyses, the effect in time domain becomes more complicated which deserves a separate and dedicated study. Once the incident wave containing f_a and f_b reaches the debonding, $f_a + f_b$ and $f_b - f_a$ are generated. However, part of these newly generated waves travel back to the debonding location and interact with the damage, and again

propagate in both forward and backward direction. This backward and forward process is repeated multiple times, so the waves contain multiple frequencies components at incident and combined frequencies. This effect can also be observed in the frequency domain in Fig. 3.10b, where spectral contents for d/λ = 1.00, d/λ = 2.00 and the fully bonded model are plotted.

Given the difficulty in analysing time domain features with respect to debonding size due the aforementioned reasons, the Fourier spectrum was used in this study. As explained before, multiple reflections occur at the debonding location, but the transmitted energy content could be an indicator of the extent of the debonding. This idea is further implemented by calculating the area under the Fourier amplitude spectrum and then it is correlated with the debonding region. Area under the curve was calculated using the trapezoidal rule for a frequency band equivalent to that of the input frequencies.

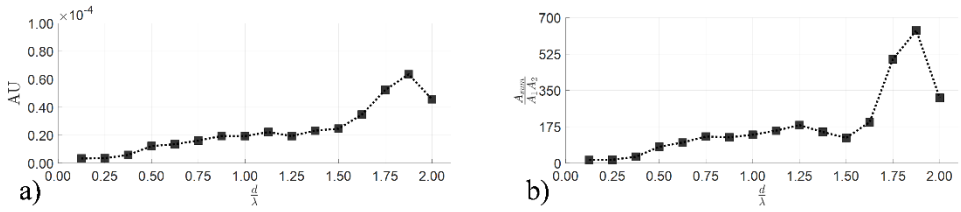

Figure 3.12. a) Transmitted energy and b) nonlinear parameter $A_{\text{sum}}/A_1 \times A_2$ in relation to debonding length-to-wavelength ratios.

Fig. 3.12a shows the relationship between d/λ and energy calculated for the sixteen debonding to wavelength ratios. The responses are nodal displacements located at 60 mm of the top of the model from the debonding centre in the forward propagating direction. A steady increasing trend is observed from d/λ = 0.125 to d/λ = 1.000, but the trend then decreases and fluctuates right after d/λ = 1.125 and greater d/λ ratios. It is because when the debonding width increases, the overall contact area also increases and generates

more energy when the wave excites and travels through the contact area. For greater values of d/λ, however, the wavelength of the generated wave at the combined frequency wave is shorter than the debonding width. Even though the contact area increases, the effect of the overall contact area is not necessarily correlated to the energy that is generated by the contact effect for d/λ greater than 1.125. A nonlinear parameter $A_{\text{sum}}/A_1 \times A_2$ is then calculated, where the amplitude of the combined frequency wave, A_{sum}, is divided by the product between amplitudes at the incident frequencies A_1 and A_2, and plotted against d/λ, as shown in Fig. 3.12b. Similar steady increase trend is observed, but the trend is not further observed for values of d/λ greater than 1.25. The relationship between the nonlinear parameter and d/λ can be further researched for indicating the debonding extent in a certain debonding range when the wavelength of the combined frequency wave is known. This is always the case since the input frequencies are always chosen in advance before conducting the tests.

3.7 Conclusion

Nonlinear Lamb wave mixing and its interaction with local debonding has been investigated in this paper using experiments and numerical simulations. It has been demonstrated that wave mixing technique can detect local debonding at adhesive metallic joints by observing generation of the combined frequency wave. The harmonics generated due to the contact effect at the debonding have been extracted in the frequency domain for the experimental samples and used to validate the 3D FE model. The presence of the combined harmonic has been demonstrated to be effective and reliable for indicating local debonding. Furthermore, the effect of the debonding width has been investigated in the frequency domain given the complicated mechanisms when mixed frequency Lamb waves interacts with the damage. The numerical results have shown that the debonding width can be correlated with the energy generated due to

debonding. This indicates that the proposed technique is also sensitive to different debonding widths within a specific range of d/λ. The study has also gained physical insight into the nonlinear Lamb wave mixing phenomena in adhesive joints. The findings presented can be used to further advance the debonding detection techniques using wave mixing.

3.8 References

1. Piekarczyk, M. and R. Grec, *Application of Adhesive Bonding in Steel and Aluminium Structures.* Archives of Civil Engineering, 2012. **58**.
2. Cavezza, F., et al., *A Review on Adhesively Bonded Aluminium Joints in the Automotive Industry.* Metals, 2020. **10**(6): p. 730.
3. Chester, R.J., K.F. Walker, and P.D. Chalkley, *Adhesively bonded repairs to primary aircraft structure.* International Journal of Adhesion and Adhesives, 1999. **19**(1): p. 1-8.
4. Lim, H.J., et al., *Development and field application of a nonlinear ultrasonic modulation technique for fatigue crack detection without reference data from an intact condition.* Smart Materials and Structures, 2016. **25**(9): p. 095055.
5. Masserey, B. and P. Fromme, *In-situ monitoring of fatigue crack growth using high frequency guided waves.* NDT & E International, 2015. **71**: p. 1-7.
6. Giurgiutiu, V., A. Zagrai, and J. Jing Bao, *Piezoelectric Wafer Embedded Active Sensors for Aging Aircraft Structural Health Monitoring.* Structural Health Monitoring, 2002. **1**(1): p. 41-61.
7. Jhang, K.Y., *Overview—Nonlinear Ultrasonic Characteristics*, in *Measurement of Nonlinear Ultrasonic Characteristics*, K.Y. Jhang, et al., Editors. 2020, Springer: Singapore.
8. Chillara, V. and C. Lissenden, *Review of nonlinear ultrasonic guided wave nondestructive evaluation: theory, numerics, and experiments.* Optical Engineering, 2015. **55**(1): p. 011002.
9. Yeung, C. and C.T. Ng, *Nonlinear guided wave mixing in pipes for detection of material nonlinearity.* Journal of Sound and Vibration, 2020. **485**: p. 115541.
10. Broda, D., et al., *Modelling of nonlinear crack–wave interactions for damage detection based on ultrasound—A review.* Journal of Sound and Vibration, 2014. **333**(4): p. 1097-1118.
11. Solodov, I.Y., N. Krohn, and G. Busse, *CAN: an example of nonclassical acoustic nonlinearity in solids.* Ultrasonics, 2002. **40**(1): p. 621-625.
12. Jhang, K.Y., *Nonlinear ultrasonic techniques for nondestructive assessment of micro damage in material: A review.* International Journal of Precision Engineering and Manufacturing, 2009. **10**(1): p. 123-135.
13. Aseem, A. and C.T. Ng, *Debonding detection in rebar-reinforced concrete structures using second harmonic generation of longitudinal guided wave.* NDT & E International, 2021. **122**: p. 102496.

14. Pruell, C., et al., *A nonlinear-guided wave technique for evaluating plasticity-driven material damage in a metal plate.* NDT & E International, 2009. **42**(3): p. 199-203.
15. Deng, M. and J. Pei, *Assessment of accumulated fatigue damage in solid plates using nonlinear Lamb wave approach.* Applied Physics Letters, 2007. **90**(12): p. 121902.
16. He, S., C.T. Ng, and C. Yeung, *Time-Domain Spectral Finite Element Method for Modeling Second Harmonic Generation of Guided Waves Induced by Material, Geometric and Contact Nonlinearities in Beams.* International Journal of Structural Stability and Dynamics, 2020. **20**(10): p. 2042005.
17. Yi, Y., et al., *Second harmonic generation at fatigue cracks by low-frequency Lamb waves: Experimental and numerical studies.* Mechanical Systems and Signal Processing, 2018. **99**: p. 760-773.
18. Yelve, N., M. Mitra, and P.M. Mujumdar, *Detection of delamination in composite laminates using Lamb wave based nonlinear method.* Composite Structures, 2017. **159**: p. 257-266.
19. Soleimanpour, R., C.T. Ng, and C. Wang, *Higher harmonic generation of guided waves at delaminations in laminated composite beams.* Structural Health Monitoring, 2017. **16**(4): p. 400-417.
20. Yan, D., B.W. Drinkwater, and S.A. Neild, *Measurement of the ultrasonic nonlinearity of kissing bonds in adhesive joints.* NDT & E International, 2009. **42**(5): p. 459-466.
21. Mohseni, H. and C.T. Ng, *Rayleigh wave propagation and scattering characteristics at debondings in fibre-reinforced polymer-retrofitted concrete structures.* Structural Health Monitoring, 2019. **18**(1): p. 303-317.
22. Shan, S., L. Cheng, and P. Li, *Adhesive nonlinearity in Lamb-wave-based structural health monitoring systems.* Smart Materials and Structures, 2016. **26**(2): p. 025019.
23. Van Den Abeele, K.E.A., P.A. Johnson, and A. Sutin, *Nonlinear Elastic Wave Spectroscopy (NEWS) Techniques to Discern Material Damage, Part I: Nonlinear Wave Modulation Spectroscopy (NWMS).* Research in Nondestructive Evaluation, 2000. **12**(1): p. 17-30.
24. Donskoy, D., et al. *N-SCAN: new vibromodulation system for detection and monitoring of cracks and other contact-type defects*. in *Smart Structures and Materials*. 2003. SPIE.
25. Sun, M., et al., *Experimental and numerical investigations of nonlinear interaction of counter-propagating Lamb waves.* Applied Physics Letters, 2019. **114**(1): p. 011902.
26. Croxford, A., et al., *The use of non-collinear mixing for nonlinear ultrasonic detection of plasticity and fatigue.* The Journal of the Acoustical Society of America, 2009. **126**(5): p. EL117-EL122.
27. Jiao, J., et al., *Evaluation of the intergranular corrosion in austenitic stainless steel using collinear wave mixing method.* NDT & E International, 2015. **69**: p. 1-8.
28. Jiao, J., et al., *Micro-crack detection using a collinear wave mixing technique.* NDT & E International, 2014. **62**: p. 122-129.
29. Jiao, J., et al., *Fatigue crack evaluation using the non-collinear wave mixing technique.* Smart Materials and Structures, 2017. **26**(6): p. 065005.
30. Blanloeuil, P., A. Meziane, and C. Bacon, *2D finite element modeling of the non-collinear mixing method for detection and characterization of closed cracks.* NDT & E International, 2015. **76**: p. 43-51.
31. Joglekar, D.M. and M. Mitra, *Time domain analysis of nonlinear frequency mixing in a slender beam for localizing a breathing crack.* Smart Materials and Structures, 2017. **26**(2): p. 025009.

32. Liu, M., et al., *Measuring acoustic nonlinearity parameter using collinear wave mixing.* Journal of Applied Physics, 2012. **112**(2): p. 024908.
33. Tang, G., et al., *Detecting Localized Plastic Strain by a Scanning Collinear Wave Mixing Method.* Journal of Nondestructive Evaluation, 2014. **33**(2): p. 196-204.
34. Chen, J., Z. Su, and L. Cheng, *Identification of corrosion damage in submerged structures using fundamental anti-symmetric Lamb waves.* Smart Materials and Structures, 2009. **19**(1): p. 015004.
35. Sharma, S. and A. Mukherjee, *Ultrasonic guided waves for monitoring corrosion in submerged plates.* Structural Control and Health Monitoring, 2015. **22**(1): p. 19-35.
36. Aristégui, C., M.J.S. Lowe, and P. Cawley, *Guided waves in fluid-filled pipes surrounded by different fluids.* Ultrasonics, 2001. **39**(5): p. 367-375.
37. Hasanian, M. and C. Lissenden, *Second order harmonic guided wave mutual interactions in plate: Vector analysis, numerical simulation, and experimental results.* Journal of Applied Physics, 2017. **122**(8): p. 084901.
38. Hasanian, M. and C. Lissenden, *Second order ultrasonic guided wave mutual interactions in plate: Arbitrary angles, internal resonance, and finite interaction region.* Journal of Applied Physics, 2018. **124**(16): p. 164904.
39. Ishii, Y., K. Hiraoka, and T. Adachi, *Finite-element analysis of non-collinear mixing of two lowest-order antisymmetric Rayleigh–Lamb waves.* The Journal of the Acoustical Society of America, 2018. **144**(1): p. 53-68.
40. Chen, H., et al., *Modeling and simulation of frequency mixing response of two counter-propagating Lamb waves in a two-layered plate.* Ultrasonics, 2020. **104**: p. 106109.
41. Aslam, M., et al., *Numerical and Experimental Investigation of Nonlinear Lamb Wave Mixing at Low Frequency.* Journal of Aerospace Engineering, 2020. **33**(4): p. 04020037.
42. Li, W., et al., *Theoretical analysis and experimental observation of frequency mixing response of ultrasonic Lamb waves.* Journal of Applied Physics, 2018. **124**(4): p. 044901.
43. Li, W., et al., *Impact damage detection in composites using a guided wave mixing technique.* Measurement Science and Technology, 2019. **31**(1): p. 014001.
44. Jiao, J., et al., *Nonlinear Lamb wave-mixing technique for micro-crack detection in plates.* NDT & E International, 2017. **85**: p. 63-71.
45. Metya, A., S. Tarafder, and K. Balasubramaniam, *Nonlinear Lamb wave mixing for assessing localized deformation during creep.* NDT & E International, 2018. **98**: p. 89-94.
46. Shan, S. and L. Cheng, *Mode-mixing-induced second harmonic A0 mode Lamb wave for local incipient damage inspection.* Smart Materials and Structures, 2020. **29**(5): p. 055020.
47. Ding, X., et al., *One-way Lamb mixing method in thin plates with randomly distributed micro-cracks.* International Journal of Mechanical Sciences, 2020. **171**: p. 105371.
48. Shan, S., et al., *New nonlinear ultrasonic method for material characterization: Codirectional shear horizontal guided wave mixing in plate.* Ultrasonics, 2019. **96**: p. 64-74.
49. Lowe, M.J.S., R.E. Challis, and C.W. Chan, *The transmission of Lamb waves across adhesively bonded lap joints.* The Journal of the Acoustical Society of America, 2000. **107**(3): p. 1333-1345.

50. Lanza di Scalea, F., P. Rizzo, and A. Marzani, *Propagation of ultrasonic guided waves in lap-shear adhesive joints: Case of incident a0 Lamb wave.* The Journal of the Acoustical Society of America, 2004. **115**(1): p. 146-156.
51. Wojtczak, E. and M. Rucka, *Wave Frequency Effects on Damage Imaging in Adhesive Joints Using Lamb Waves and RMS.* Materials, 2019. **12**(11): p. 1842.
52. Ramadas, C., et al., *Interaction of the primary anti-symmetric Lamb mode (Ao) with symmetric delaminations: numerical and experimental studies.* Smart Materials and Structures, 2009. **18**(8): p. 085011.
53. Tian, Z., L. Yu, and C. Leckey, *Delamination detection and quantification on laminated composite structures with Lamb waves and wavenumber analysis.* Journal of Intelligent Material Systems and Structures, 2015. **26**(13): p. 1723-1738.
54. Koissin, V., A. Demčenko, and V.A. Korneev, *Isothermal epoxy-cure monitoring using nonlinear ultrasonics.* International Journal of Adhesion and Adhesives, 2014. **52**: p. 11-18.
55. Escobar-Ruiz, E., et al., *Non-linear Ultrasonic NDE of Titanium Diffusion Bonds.* Journal of Nondestructive Evaluation, 2014. **33**(2): p. 187-195.
56. Ju, T., et al., *Nondestructive evaluation of thermal aging of adhesive joints by using a nonlinear wave mixing technique.* NDT & E International, 2019. **103**: p. 62-67.
57. de Lima, W.J.N. and M.F. Hamilton, *Finite-amplitude waves in isotropic elastic plates.* Journal of Sound and Vibration, 2003. **265**(4): p. 819-839.
58. Alleyne, D. and P. Cawley, *A two-dimensional Fourier transform method for the measurement of propagating multimode signals.* The Journal of the Acoustical Society of America, 1991. **89**(3): p. 1159-1168.
59. Hu, X., C.T. Ng, and A. Kotousov, *Scattering characteristics of quasi-Scholte waves at blind holes in metallic plates with one side exposed to water.* NDT & E International, 2021. **117**: p. 102379.
60. Yang, Y., et al., *Finite element prediction of acoustoelastic effect associated with Lamb wave propagation in pre-stressed plates.* Smart Materials and Structures, 2019. **28**(9): p. 095007.
61. Willberg, C., et al., *Comparison of different higher order finite element schemes for the simulation of Lamb waves.* Computer Methods in Applied Mechanics and Engineering, 2012. **241-244**: p. 246-261.
62. Rajagopal, P., et al., *On the use of absorbing layers to simulate the propagation of elastic waves in unbounded isotropic media using commercially available Finite Element packages.* NDT & E International, 2012. **51**: p. 30-40.
63. Ng, C.T. and M. Veidt, *Scattering characteristics of Lamb waves from debondings at structural features in composite laminates.* The Journal of the Acoustical Society of America, 2012. **132**(1): p. 115-123.
64. Diamanti, K., J.M. Hodgkinson, and C. Soutis, *Detection of Low-velocity Impact Damage in Composite Plates using Lamb Waves.* Structural Health Monitoring, 2004. **3**(1): p. 33-41.
65. Lee, Y., Y. Lu, and R. Guan, *Nonlinear guided waves for fatigue crack evaluation in steel joints with digital image correlation validation.* Smart Materials and Structures, 2020. **29**(3): p. 035031.
66. Li, B., et al., *Quantitative identification of delamination at different interfaces using guided wave signals in composite laminates.* Journal of Reinforced Plastics and Composites, 2015. **34**(18): p. 1506-1525.

Chapter 4

Damage detection in composite laminates using nonlinear guided wave mixing

Juan Carlos Pineda Allen and Ching Tai Ng
School of Civil, Environmental and Mining Engineering
The University of Adelaide, SA 5005, Australia

Manuscript: Pineda Allen, J.C.; Ng, C.T. Damage detection in composites laminates using nonlinear guided wave mixing.

Statement of Authorship

Title of Paper	Damage detection in composite laminates using nonlinear guided wave mixing.
Publication Status	☐ Published ☐ Accepted for Publication ☐ Submitted for Publication ☑ Unpublished and Unsubmitted w ork w ritten in manuscript style
Publication Details	Pineda Allen, J.C.; Ng, C.T. Damage detection in composite laminates using nonlinear guided wave mixing.

Principal Author

Name of Principal Author (Candidate)	Juan Carlos Pineda Allen
Contribution to the Paper	Performed literature review, developed and prepared the experimental configuration, performed experiments, developed numerical model, data processing and analyses, and prepared the manuscript.
Overall percentage (%)	80%
Certification:	This paper reports on original research I conducted during the period of my Higher Degree by Research candidature and is not subject to any obligations or contractual agreements with a third party that would constrain its inclusion in this thesis. I am the primary author of this paper.
Signature	Date: 23/02/2022

Co-Author Contributions

By signing the Statement of Authorship, each author certifies that:

i. the candidate's stated contribution to the publication is accurate (as detailed above);

ii. permission is granted for the candidate in include the publication in the thesis; and

iii. the sum of all co-author contributions is equal to 100% less the candidate's stated contribution.

Name of Co-Author	Ching Tai Ng
Contribution to the Paper	Supervised the work, reviewed the manuscript, prepared for submission and acted as corresponding author.
Signature	Date: 24/02/2022

Name of Co-Author	
Contribution to the Paper	
Signature	Date:

Please cut and paste additional co-author panels here as required.

Chapter 4: Damage Detection in Composite Laminates Using Nonlinear Guided Wave Mixing

Abstract

This paper presents a delamination damage detection technique based on the nonlinear response on Lamb waves in composite laminates. In the approach, a network of transducers is used to locate the damage and reconstruct its location using combined frequency waves originated due to contact nonlinearity when the incident wave interacts with the damage. An experimentally validated numerical model is used to verify the proposed damage detection technique. The results show that the proposed method can effectively predict the damage location, and it does not require baseline measurements, which makes it suitable for reference-free damage detection techniques.

Keywords: wave mixing; combined frequency wave; delamination; Lamb wave; nonlinear; composite laminate.

4.1 Introduction

Advances in the civil, aerospace and automotive industry have pushed the development of innovative materials that can enhance mechanical properties. However, developing new materials need to further understand its physical properties, as well as its performance and sustainability demands. Composite laminates materials are lightweight, corrosion-resistant, and high-strength materials manufactured with fibres within an epoxy matrix. Despite excelling mechanically in the in-plane direction, composite laminates suffer from relatively weak out-of-plane mechanical properties, which makes it susceptible to delamination defects. Moreover, in-service operation of composite structural components increases the probabilities of several types or combination of damage. Depending on the undertaken task, composite laminate is vulnerable to cracks, fibre breakage, warping, delamination and disbonds, etc. The presence of service-related stresses can further change the degree of damage. Delamination refers to the partial separation between adjoining plies, and can be attributed to manufacturing process defects (e.g. air entrapment) or damage related mechanisms (e.g. impact) and can derive into poor performance such as loss of carrying capacity [1] or changed vibration characteristics [2]. Furthermore, delamination is internal and barely visible.

Multiple efforts have been put together within the non-destructive testing (NDT) and structural health monitoring (SHM) communities to address delamination-related damage in composite structures. Non-destructive testing techniques such as eddy current [3], thermography [4], and traditional ultrasonics [5] have shown potential in evaluating such type of damage. Likewise SHM systems have also been developed using fibre optics [6] and guided waves [7]. Guided waves have been particularly attractive for its ability to inspect long distance, capability to inspect inaccessible areas and low-energy consumption.

Moreover, guided waves have the advantage of being suitable for on-site inspection.

Guided waves can be classified in linear guided waves and nonlinear guided waves. Linear guided waves rely on information such as attenuation, reflection, wave velocity and other temporal parameters and have demonstrated effectiveness in detecting damage in composite laminates [8] [9]. Nonlinear guided waves rely on nonlinear acoustic phenomena [10]. Its advantage over linear guided waves is they have proven to be more efficient for early damage detection [11], micro-structural damage [12], and even undamaged material characterization [13]. Recent developments using nonlinear guided waves were achieved using second harmonic generation [14]. Yang *et al.* investigated crack-type of damage using low frequency Lamb waves in isotropic plates [15]. Horizontal cracks due to fatigue damage and impact damage in composites were investigated using second harmonics in [16] and [17] respectively. Soleimanpour *et al.* [18] studied second harmonic generation due to delamination defect in composites. Temperature-related damage in composites by means of second harmonic generation were also investigated [19]. Nevertheless, second harmonics could also be generated by equipment nonlinearities. The order of magnitude of the second harmonic is often of small magnitude which hinders its extraction for further analysis.

To overcome the issues of second harmonic generation, mixed-frequency response utilizes two waves of different frequencies to generate combined harmonic waves when the incident waves interact with a source of nonlinearity, either with material or damage-related nonlinearity. Early stage studies exploring the use of third order mixed-frequency response for damage detection have been reported [20] [21] [22] although these are beyond the scope of this paper. Normally known as vibro-acoustic modulation, this approach makes use of a high frequency probing wave and low frequency pumping wave. Early studies explored the potential for material characterization and damage

detection [23]. Klepka *et al.* carried out studies to detect cracks [24] and impact damage [25]. Lim *et al.* also conducted extensive research and proposed a field development for crack detection in aluminium plates [26].

Different to vibro-acoustic modulation, if two high frequency waves are used the technique is wave-mixing. Researchers have explored the use of bulk wave mixing for characterization of materials with fatigue and plasticity [27], corroded specimens [28] or thermal aging in adhesive joints [29]. More recently, fundamental theoretical and analytical development further enriched the body of literature extending the wave-mixing studies into guided waves [30] [31] [32]. Some studies were carried out to detect different types of damage [33] [34] [35]. However, there is still much research ahead to take full advantage and to develop in-situ monitoring techniques using guided wave-mixing. As such, this research explores wave-mixing for damage detection and localization in composite laminates.

This study proposes an imaging algorithm for delamination damage detection in a quasi-isotropic laminate. Experimental and finite element studies are conducted to evaluate the proposed technique and the experimentally verified finite element model is used to further investigate the performance of the proposed method.

The paper is organized as follow. Section 4.2 presents a background of the nonlinear ultrasonic waves due to contact acoustic nonlinearity. The proposed approach for detection of damage and its localization is presented in Section 4.3. Next, Section 4.4 describes the experimental setup, where Lamb wave mode tuning curves, group velocity and displacement amplitude are calculated. Section 4.5 follows, where a three-dimensional numerical model is described and further validated with experimental results. The imagining algorithm is implemented for various damage locations, and the results and performance are discussed in Section 4.6. Finally, a conclusion is presented in Section 4.7.

4.2 Nonlinear ultrasonic waves due to contact acoustic nonlinearity

Nonlinear acoustic phenomena can be classified into material nonlinearity and contact nonlinearity. Nonlinear waves have been widely used in the literature to evaluate material nonlinearity due to its advantage to detect micro-scale damage such as dislocations in intact specimens [36] [37]. Some studies addressed fatigue damage using bulk waves [38], others evaluated material nonlinearity using guided waves [39] [40], creep damage [11] and plasticity [12] driven damage, which proved efficient for detecting incipient or early stage damage. Contact acoustic nonlinearity (CAN) occurs when the propagating wave induces repetitive collision between the internal surfaces of the damage [41]. It is associated with a stiffness asymmetry at contact-type damage during interaction with the wave. It has been widely investigated for guided wave-based cracks detection in metals [15] [42], impact damage in composite laminates [43] and also for bulk waves interaction with damage [44] [45]. The effect is schematically shown in Figure 4.1 for a dual frequency incident wave $x\,(f_a, f_b)$. During the interaction, the compressive part of the incident wave can travel from one interface to the adjoining interface only during closure of the damage whereas the discontinuity between interfaces when the damage is open does not allow the wave to pass through, thus generating second and combined harmonics in the output response $y\,(f_a, f_b, 2f_a, 2f_b, f_{a\pm b})$ of the system. Given the shortcomings using second harmonic generation such as its small magnitude and equipment-related nonlinearities, combined harmonics will be the attention of this study.

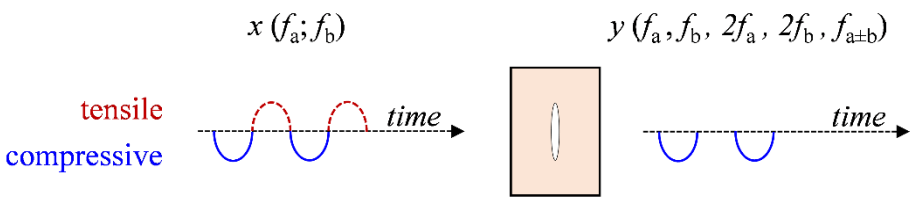

Fig. 4.1. Schematic representation of the CAN effect

4.3 Delamination detection using guided-wave mixing

In the proposed damage detection method, a network of transducers is required to scan the inspected component. Each transducer can be used both as actuator and sensor for actuating and measuring the signal. The scan is carried out in sequence. In other words, when one transducer actuates the signal, the remaining transducers serve as sensors. A four-transducer network is implemented in this study. A representative diagram is shown in Figure 4.2a. In the first step, P_1 is the actuator and the signal is received by P_2, P_3 and P_4. Following, P_2 actuates the signal, and P_1, P_3 and P_4 are the sensors. This process is sequentially repeated until all four transducers are actuated. When the incident wave interacts with the damage, contact nonlinearity is generated and manifested through the existence of combined frequency waves. The signals collected from the network of transducers are expected to contain information regarding the presence and location of the damage. Signals are recorded for post processing.

The inspection area is discretised into image pixels (IP) as in Figure 4.2b. When the incident guided wave interacts with the damage, the combined frequency waves are generated. Under the assumption that the IP is the damage location, the process can be split into two stages: (i) when the incident wave is generated at the transducer P_n, propagates and arrives at the IP (x, y) and (ii) when the combined frequency wave is generated at the IP (assumed damage location) and propagates to the transducer P_m. Locations of the transducers and IP are known before carrying out the inspection. The group velocity values for the incident waves is obtained experimentally and numerically and their values are presented in Sections 4.4.4 and 4.5.2, respectively. Group velocities corresponding to the combined frequency waves are calculated numerically. They are not included in this paper for the sake of brevity. To calculate the arrival time of the combined frequency wave:

$$t_{mn}(x,y) = \frac{\sqrt{(x-x_m)^2+(y-y_m)^2}}{c_g^{f_i}(\theta_m)} + \frac{\sqrt{(x_n-x)^2+(y_n-y)^2}}{c_g^{f_c}(\theta_n)} \quad (1)$$

where x_m and y_m are the coordinates of the actuator and x_n and y_n are the coordinates of the sensor as shown in Figure 4.2. The first term on the right-hand side of the Equation (1) is the arrival time of the incident frequency wave from transducer P_n to the image pixel IP (x, y) and the second term is the arrival time of the combined frequency wave from the image pixel IP (x, y) to the transducer P_m. The average value of the group velocities of the incident frequencies is $c_g^{f_{if}}(\theta_m)$ and $c_g^{f_{cf}}(\theta_n)$ is the group velocity of the combined frequency wave. Given that the structural component under study is not perfectly isotropic, group velocity values are angular dependent, indicated by θ_m for the propagation direction between actuator and damage, and θ_n for the propagation direction between damage and sensor.

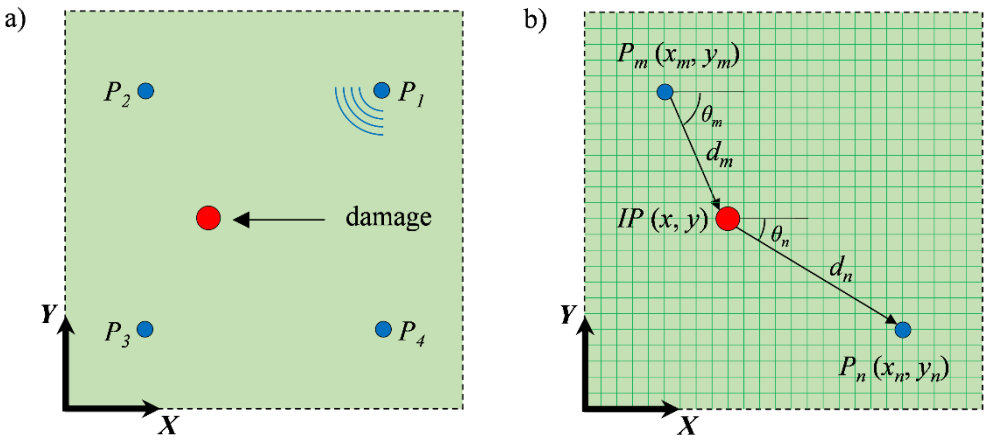

Fig. 4.2. a) Transducers network actuation and sensing, b) discretization of inspection area for damage image reconstruction

A time-frequency analysis using a short-time Fourier transform is carried out to extract data corresponding to the incident frequency and those corresponding to the combined frequency waves. Cross-correlation between the

incident pulse actuated at P_n and the measured signal at P_m is carried out in this study. It is defined as:

$$C_{mn}(t) = \int_0^T A_{mn}\left(\tau, f_{\frac{a+b}{2}}\right) S_{mn}(t+\tau, f_{a\pm b}) \quad (2)$$

where A_{mn} is the averaged time-frequency data of the actuated pulse at frequencies f_a and f_b. S_{mn} is the time-frequency data of the scattered pulse at combined frequencies $f_{a\pm b}$, when P_m and P_n are actuator and sensor, respectively. Then, by superimposing the power flux of all the actuator-sensor path images [46], the damage detection is reconstructed as:

$$I(x,y) = \sum_{m=1}^{N} \sum_{n\neq m}^{N} \beta_{mn}\left(C_{mn}(t_{mn})\right)^2 \quad (3)$$

where β_{mn} is a factor that takes into consideration the varying sensitivities for each signal path of image. An experimental verification is presented in Section 4.4 and a finite element model is developed in Section 4.5 and is validated using experimental measurement to assess the performance of the proposed method in determining existence and location of damage based on the nonlinear combined frequency waves. To ensure the damage detection practical for development and implementation small and inexpensive piezoceramic discs transducers, instead of the SLDV used in Section 4.4.2, are employed.

4.4 Experiment

This section provides detailed descriptions of the experimental setup, which includes composite laminate specimen, and the actuators and sensors.

4.4.1 Specimen description

A composite laminate with in-plane dimensions of 800 mm × 800 mm was manufactured using eight layers of unidirectional carbon/epoxy Eporite EHM-32 prepeg lamina with stacking sequence $[-45/45/0/90]_s$.. The fibre volume fraction is 0.55, density is 1300 kg/m^3 density and thickness is 0.25 mm. The total thickness

of the composite laminate is 2.00 mm. The elastic properties of the lamina are listed in Table 4.1.

Table 4.1. Elastic properties of the lamina

E_{11} (GPa)	$E_{22}=E_{23}$ (GPa)	$G_{12}=G_{13}$ (GPa)	G_{23} (GPa)	$\nu_{12}=\nu_{13}$	ν_{23}
111	7.16	3.62	2.20	0.33	0.44

4.4.2 Actuating and sensing

The guided wave was excited by an adhesively bonded piezoceramic transducer with 5 mm diameter and 2 mm thickness. A backing mass was bonded on top of the piezoceramic transducer to increase the out-of-plane excitability. To conduct the guided waves experiments in this section, an actuating and sensing system was employed in this study. The system, which consists of a computer-controller arbitrary waveform generator, a power amplifier and a Scanning Laser Doppler Vibrometer (SLDV), is schematically shown in Figure 4.3. The angle between the laser beam and the specimen surface is α.

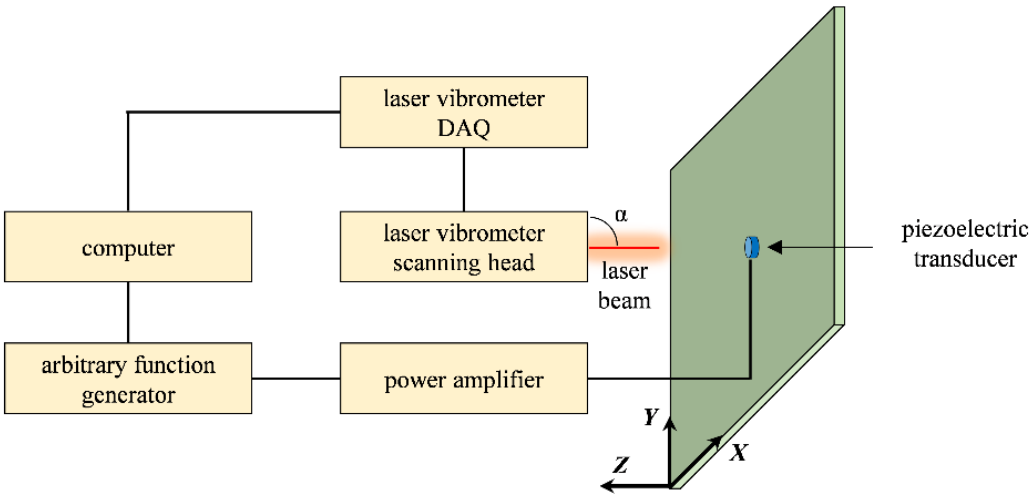

Fig. 4.3. Experimental configuration

4.4.3 Mode-tuning curve

A mode-tunning analysis was first carried out to determine the excitability of both the anti-symmetric (A_0) and symmetric (S_0) Lamb wave modes at different

excitation frequencies. A 5-cycle sinusoidal tone burst pulse modulated by Hann window was created by the computer-controller arbitrary function generator and amplified up to 160Vpp (peak-to-peak output voltage) and then sent to the piezoceramic transducer. The generated Lamb waves range from 60kHz to 400Hz in steps of 20kHz are measured using a one-dimensional laser scan, with the laser head positioned at a α=30° angle with respect to the specimen surface such as the laser beam out-of-plane sensitivity can capture both the S_0 and A_0 modes. A fixed location 100mm away from the transducer in the θ=0° direction of the composite plate orientation is chosen for measurement. Preliminary tests indicated that A_0 mode is separated from S_0 mode at the selected distance. Low-pass filter and averaging are used in the acquisition of the data. The obtained mode tuning curve is shown in Figure 4.4. For the purpose of the studies, we can see that the amplitude of the A_0 mode is reasonably larger that the S_0 for a frequency band ranging from 140 to 280 kHz.

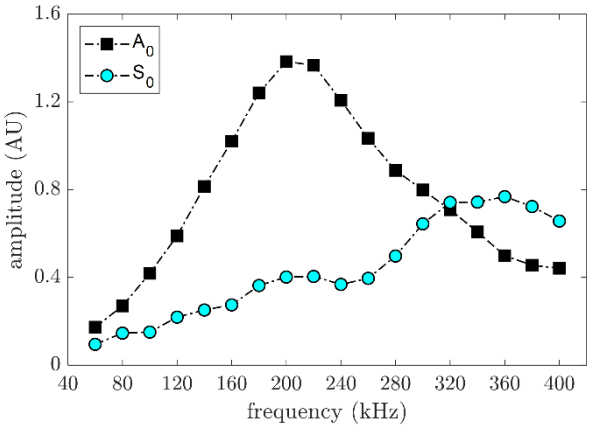

Fig. 4.4. Mode tuning curve at θ=0°

4.4.4 Amplitude, group velocity and frequencies selection

Based on the obtained mode tuning curve from the previous section, a number of preliminary tests were conducted in order to determine a suitable frequency pair for the damage detection studies. Given its sensitivity and dominant out-of-plane displacement, the two frequencies should have similar excitability of the

A_0 mode, and the chosen frequency pair is 170 kHz and 250 kHz. In addition, the combined harmonic of this frequency pair is not a multiple of the incident wave frequency as this could help distinguish the second harmonics from the combined harmonics in frequency domain. The tests of this section were carried out to calculate group velocity and amplitude values of the A_0 mode. The measurements of this section were conducted using a SLDV with the laser head positioned at α=90° angle, such as the laser beam is perpendicular to the surface of the composite plate. This setup allows flexibility to scan many points using non-contact sensing. Out-of-plane displacement were obtained for 36 points, at 10 degrees from each other and located at r = 80 mm from the centre of the piezoceramic transducer, another 36 points at r = 90 mm and 36 more points at r = 120 mm. In total, the scan comprised 108 points. A 6-cycles 170 kHz tone burst pulse was created using an arbitrary waveform generator and sent to a power amplifier. The signal was amplified up to 160Vpp and fed to the piezoceramic transducer. The signal acquisition was averaged 1,000 times to minimize the noise effect and filtered using low-pass filter. Similar experiments were also conducted for a 6-cycles 250 kHz tone burst pulse.

4.5 Three-dimensional explicit finite element simulation

4.5.1 Model description

To simulate the guided wave propagation in the quasi-isotropic composite laminate, a three-dimensional finite element (FE) model is developed using ABAQUS software. The dimension of the model is 375 × 375 × 2 mm^3. Each of the 8 plies is modelled as a unidirectional layer and orientated according to the stacking sequence $[-45/45/0/90]_s$, and tied with its corresponding top and bottom layer using tie constrains. Eight-noded solid brick elements with reduced integration were used. The maximum element size was set to be 0.20 × 0.20 × 0.25 mm^3. There is one element through the thickness of each ply and there are 8

layers of element in the thickness direction of the composite laminate. To avoid wave reflections from the edge, absorbing layers by increased damping (ALID) are modelled all around the four sides of the plate. There are 50 layers in total, each layer is 1 mm wide. Thus, the total width of the absorbing layer is 50mm and the dimension of the plate without ALID is 275 × 275 mm². Mass-proportional damping was used in ALID. The power-law formulation in Eq. (4) calculates the value of damping at each layer.

$$\varphi_M(x) = \varphi_{max} \times Y(x)^P \tag{4}$$

where the location from the edge of the plate to a location of ALID is indicated by x. In the study, $P = 3$ and $\varphi_{max} = 250{,}000$.

A_0 mode Lamb wave is excited by applying out-of-plane displacement to a circular area of 5 mm diameter and centered at ($x = 187.5mm; y = 187.5mm$), which is the same area covered by the piezoelectric disc transducer in the experiment as described in Section 4.4.2. Out-of-plane displacement was obtained for 36 points located at r = 80mm from the centre of the excitation area, another 36 points at r = 90mm and 36 additional points at r = 120mm, as shown in Figure 4.5.

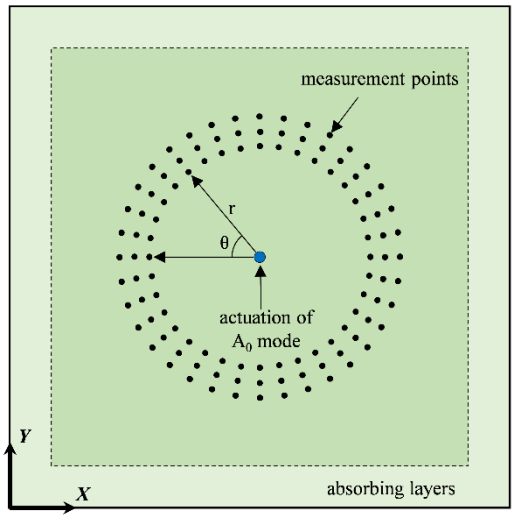

Fig. 4.5. Schematic diagram of the FE model with actuation and sensing points.

4.5.2 Amplitude and group velocity

A typical numerically simulated time domain signal with its corresponding frequency spectra is shown in Figure 4.6 together with the experimental data, which was measured at the location r = 80mm from the centre of the actuator and θ=0° of the composite plate. The excitation is 170 kHz. Further, normalized displacements and group velocity were calculated and are shown in Figure 4.7. Group velocity was calculated using the envelope of the time domain signal and the distance between consecutive points for all values of θ. Normalized displacements were calculated for 36 points located at r = 80mm from the actuator. Therefore, based on the time domain and frequency domain data, together with the group velocity and normalized amplitude, it can be concluded that the FE model can accurately predict the Lamb wave propagation.

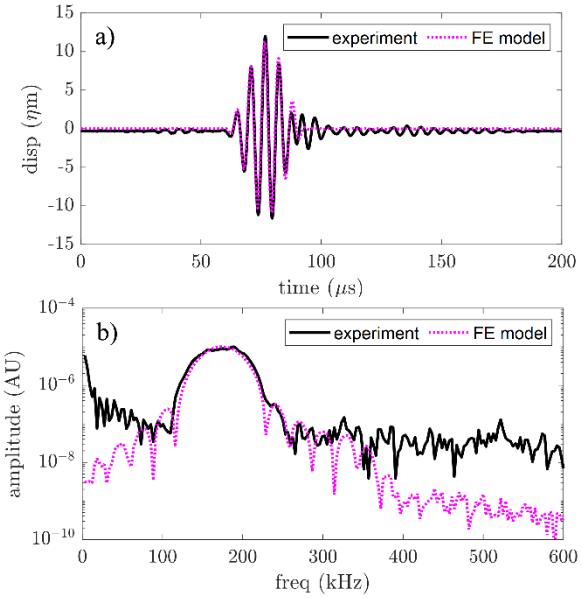

Fig. 4.6. Typical a) time domain, and b) frequency domain data for a point located at r=80mm and θ=0° from actuator

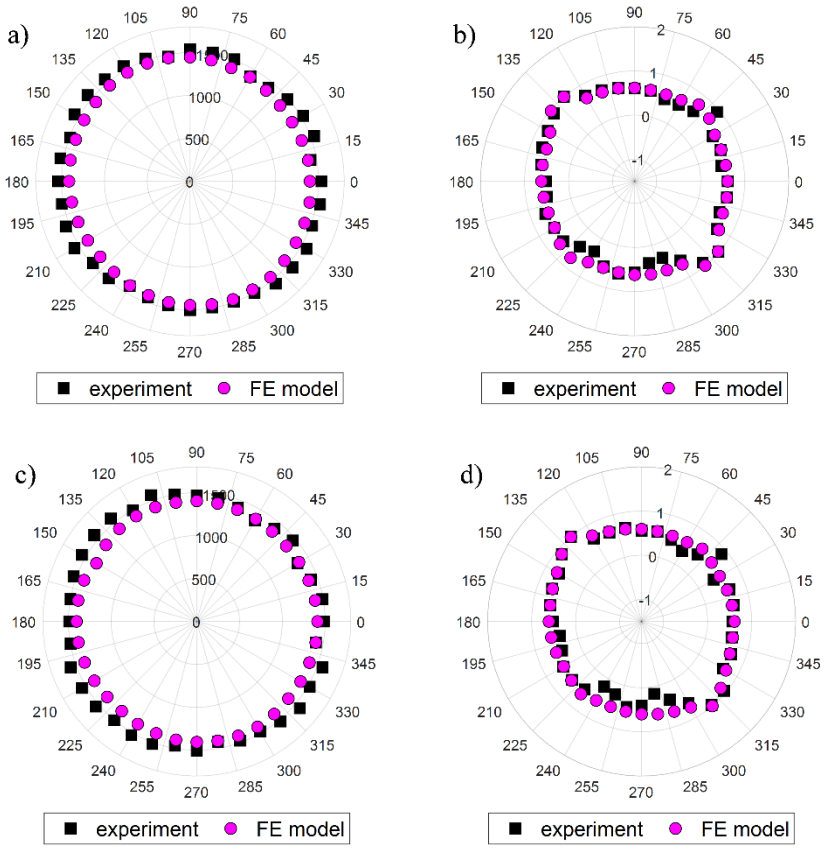

Fig. 4.7. a) group velocity 170 kHz pulse, b) normalized amplitude 170 kHz pulse, c) group velocity 250 kHz pulse, and d) normalized amplitude 250 kHz pulse.

4.6 Finite element studies

To implement the proposed damage detection technique, a series of finite element simulations were conducted. The model is similar to the validated finite element model described in Section 4.5.1 in terms of stacking sequence, mesh element size and material properties. However, for the purpose of the studies of this section, a four-transducer network and a delamination damage were introduced. Coordinates of the transducers are $x_{\mathrm{P1}} = 212.5mm\ y_{\mathrm{P1}} = 212.5mm$; $x_{\mathrm{P2}} = 62.5mm\ y_{\mathrm{P2}} = 212.5mm$; $x_{\mathrm{P3}} = 62.5mm\ y_{\mathrm{P3}} = 62.5mm$ and $x_{\mathrm{P4}} = 212.5mm\ y_{\mathrm{P4}} = 62.5mm$. Each transducer is excited sequentially while the rest of the transducers are used as the sensors. A_0 mode is excited by applying out-of-plane displacement to a circular area of 5 mm diameter, which is the same area covered by the piezoelectric disc transducer. Three different damage locations

were evaluated and are listed in Table 4.2. In general, a symmetrically located delamination would result in a zero-strain state at the middle plane, and thus, A_0 would be unable to detect [47]. A 15mm-diameter delamination is introduced in the model by relaxing the tie constrains between the third and fourth layer of the composite laminate, which is asymmetrically located in the thickness direction of the composite laminate.

Table 4.2. Damage location coordinates in each damage cases

	x_d (mm)	y_d (mm)
Case A	187.5	147.5
Case B	232.5	92.5
Case C	87.5	107.5

A contact effect is expected when the incident wave interacts with the damage, which can be observed in Figure 4.8 when the signal is excited by P_2 when the damage is located at $x_d = 87.5mm\, y_d = 107.5mm$. As a result, the signals received in the remaining transducers contain fundamental frequencies and combined frequencies, which were originated due to contact nonlinearity. A typical out-of-plane signal received at transducer P_3 when P_2 is excited in Case C is shown in Figure 4.8a. In the corresponding frequency spectrum of Figure 4.8b, the incident and combined frequency waves are observed.

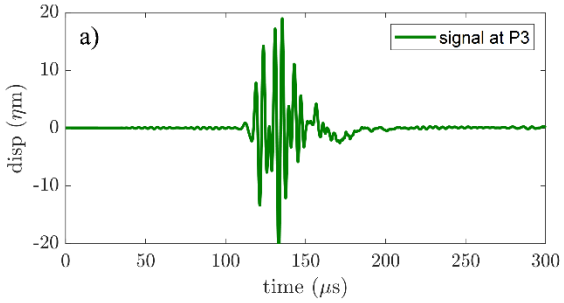

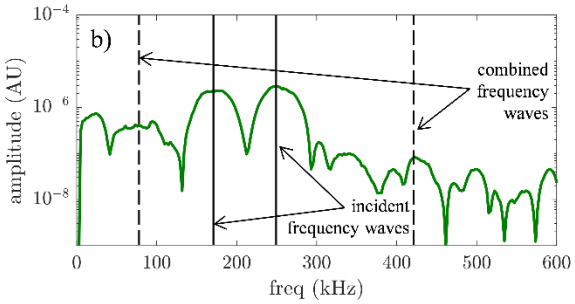

Fig. 4.8. a) Out-of-plane response at P_3 when P_2 is excited, b) corresponding frequency spectrum.

Given that the proposed damage detection technique requires time-frequency data, special attention is necessary when selecting the number of windows. As such, we studied different number of windows and the effect of this in the proposed detection technique. A typical spectrogram, or time-frequency analysis is shown in Figure 4.9a for Case C when P_2 is excited and signal is received by P_3, the incident frequencies and combined frequency wave are observed. For this case, the total number of windows is $n_w = 6$.

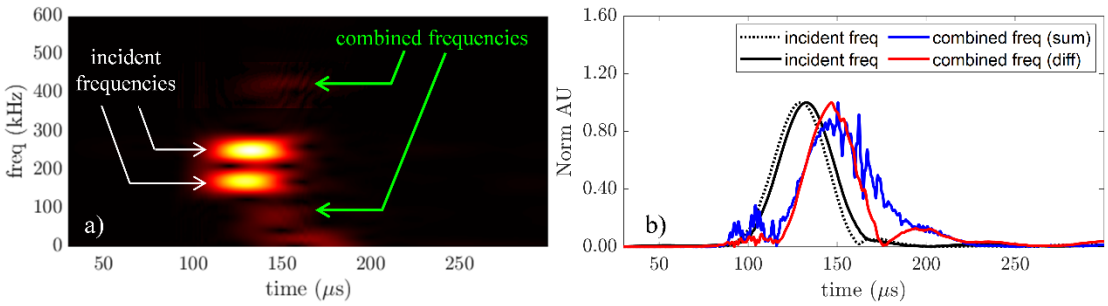

Fig. 4.9. a) Spectrogram for the signal actuated by P_2 and received by P_3, b) extracted amplitudes for of the harmonics of interest.

Once the sequential scan process is completed, all the signals are collected and processed using the time-frequency analysis, then signals are extracted as shown in Figure 4.9b. With this information, each actuator-sensor contributes to the total reconstructed image. By using Equation (3), and the combined frequency wave at the sum frequency harmonic, the reconstructed image for Case A is shown in Figures 4.10a)-10c), for three different number of windows n_w. Using

the combined frequency wave at the difference frequency harmonic, a similar image can also be also reconstructed as in Figures 4.10d)-10f). To provide a more robust image location of the damage, a binary image is created by filtering out minor intensity peaks of the reconstructed image using an arbitrary threshold value [48]. In this study, a threshold value of 85% is used. The centroid of the binary image is calculated (indicated with a cross mark) and compared to the centroid of the actual damage (indicated with a hollow black circle). Location of the transducers is marked with a white circle. To quantify the error between the estimated damage location and actual damage location, an error is defined as $\text{Err} = \sqrt{(x_\text{e} - x_\text{r})^2 + (y_\text{e} - y_\text{r})^2}$, which is indicated for each of the binary images from the reconstructed images. It is observed that for the three cases shown in Figure 4.10 ($\text{n}_w = 4$; $\text{n}_w = 6$; $\text{n}_w = 8$), detection error decreases for the reconstructed images using combined frequency wave at sum frequency harmonic. This effect is not visible for the reconstructed images using the combined frequency wave at difference frequency harmonic. The performance under different window numbers was evaluated. It was found that while increasing the window number, detection error for Case A using the combined frequency wave at the sum frequency harmonic steadily decreases. But its counterpart using the difference frequency harmonic decreases at the beginning reaching a plateau and then the error increase.

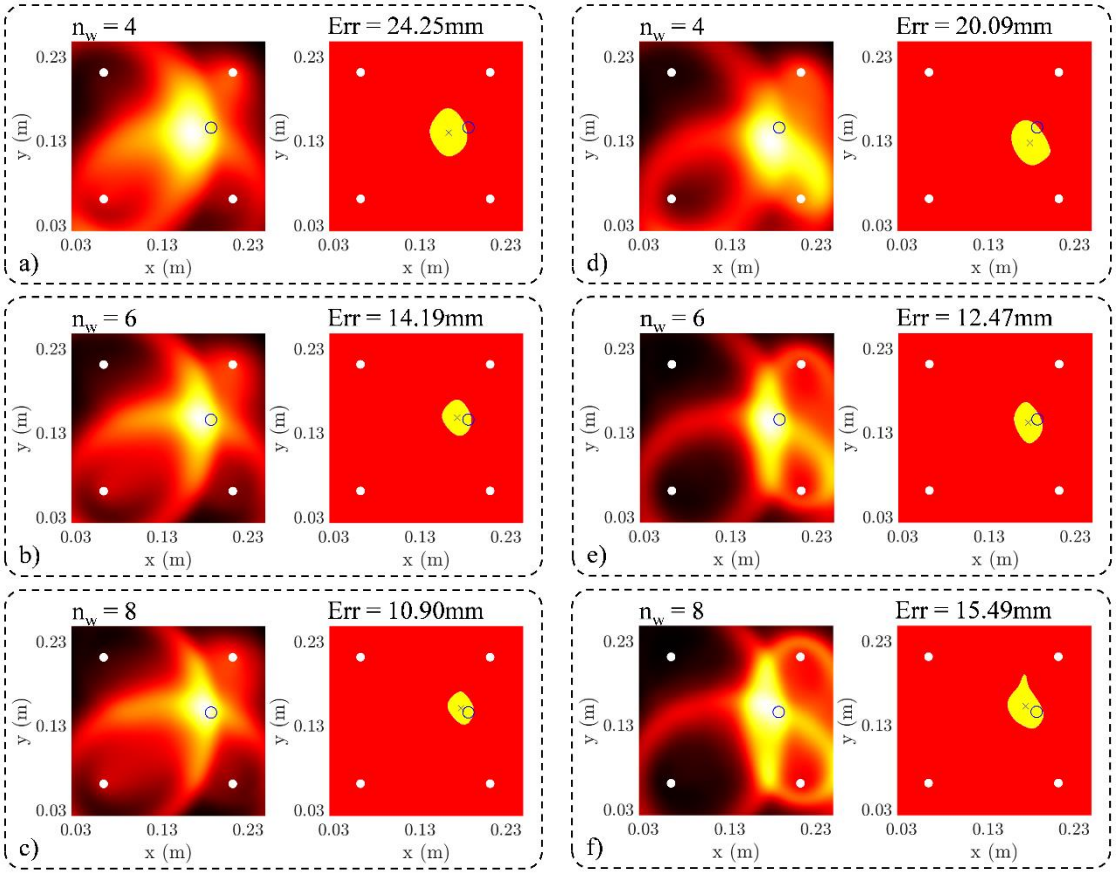

Fig. 4.10. Reconstructed images and binary images of the estimated damage location for Case A using a) n_w=4 with combined frequency wave at sum frequency, b) n_w=6 with combined frequency wave at sum frequency, c) n_w=8 with combined frequency wave at sum frequency, d) n_w=4 with combined frequency wave at difference frequency, e) n_w=6 with combined frequency wave at difference frequency and f) n_w=8 with combined frequency wave at difference frequency (hollow circle: actual damage location, cross: predicted damage location)

Figure 4.11 shows results for Case B, where the damage is located outside of the transducers area. The error is also lesser using the sum frequency harmonic as compared to the difference frequency harmonic, although the performance of the imaging algorithm seems to be slightly reduced. For Case C results shown in Figure 4.12, the error decreases using the sum frequency harmonic and using the difference frequency harmonic. However, for the difference frequency harmonic, error is around doubled or tripled. Special attention must be paid while reducing the error by increasing the number of windows, as some frequency information could be neglected if the number of windows is increased indefinitely. Using wave mixing approach possess the advantage that it is potentially baseline free

approach. Moreover, wave mixing approach can avoid equipment nonlinearities, which is an issue for second harmonic approaches.

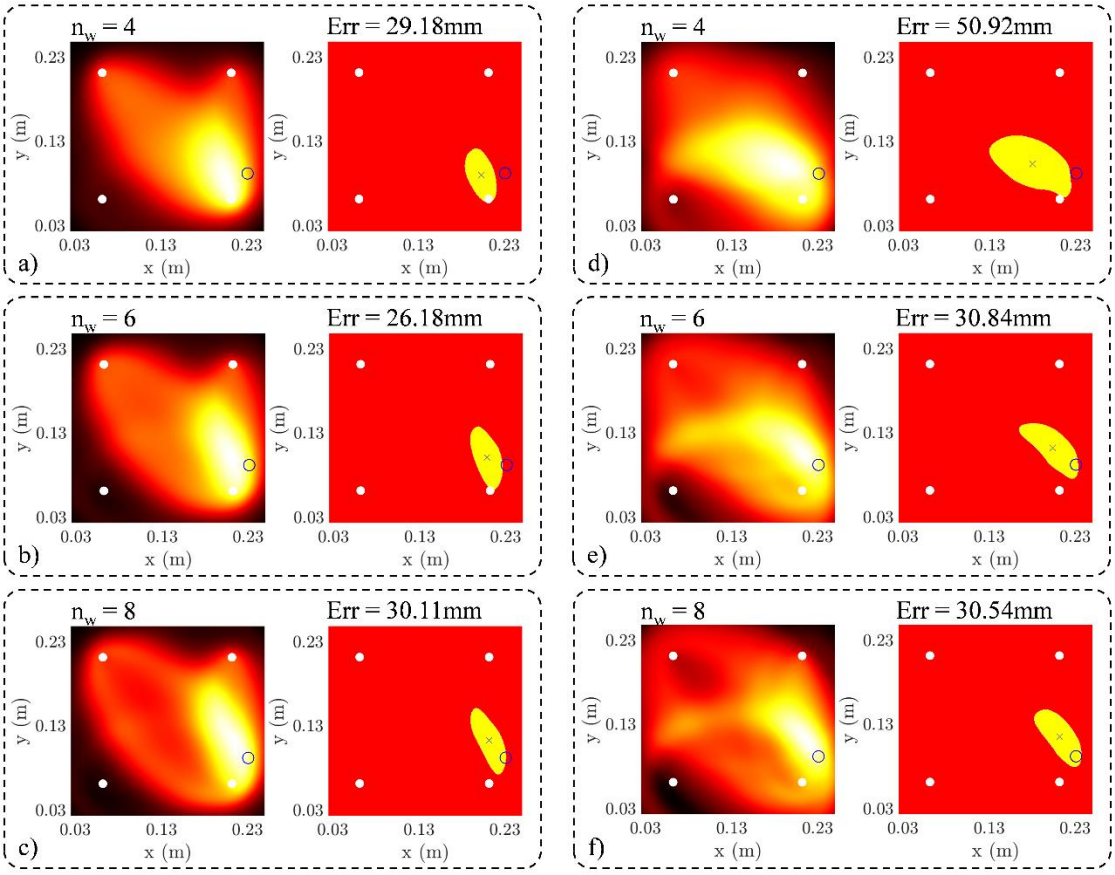

Fig. 4.11. Reconstructed images and binary images of the estimated damage location for Case B using a) n_w=4 with combined frequency wave at sum frequency, b) n_w=6 with combined frequency wave at sum frequency, c) n_w=8 with combined frequency wave at sum frequency, d) n_w=4 with combined frequency wave at difference frequency, e) n_w=6 with combined frequency wave at difference frequency and f) n_w=8 with combined frequency wave at difference frequency (hollow circle: actual damage location, cross: predicted damage location)

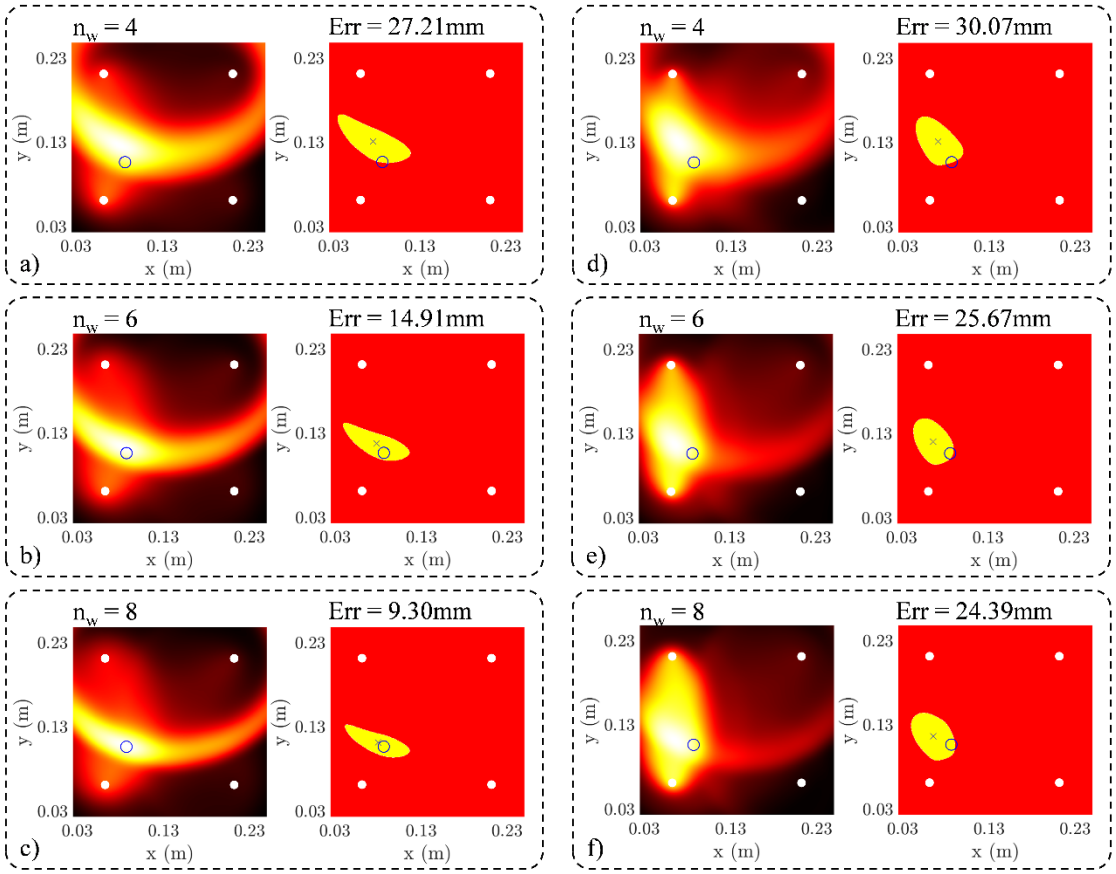

Fig. 4.12. Reconstructed images and binary images of the estimated damage location for Case C using a) n_w=4 with combined frequency wave at sum frequency, b) n_w=6 with combined frequency wave at sum frequency, c) n_w=8 with combined frequency wave at sum frequency, d) n_w=4 with combined frequency wave at difference frequency, e) n_w=6 with combined frequency wave at difference frequency and f) n_w=8 with combined frequency wave at difference frequency (hollow circle: actual damage location, cross: predicted damage location)

Figure 4.13 compares the effect of the number of windows for each of the cases. It is observed that by using the sum frequency harmonic, the damage detection technique is more robust than using the difference frequency harmonic. One possible reason is that in general, the extracted time-frequency signals from the sum frequency harmonic are more evident as compared to the difference frequency harmonic for the selected frequencies in this study. The authors believe this effect is due to the magnitude of the difference frequency harmonic, its bandwidth and how separated it is from the incident frequency harmonics.

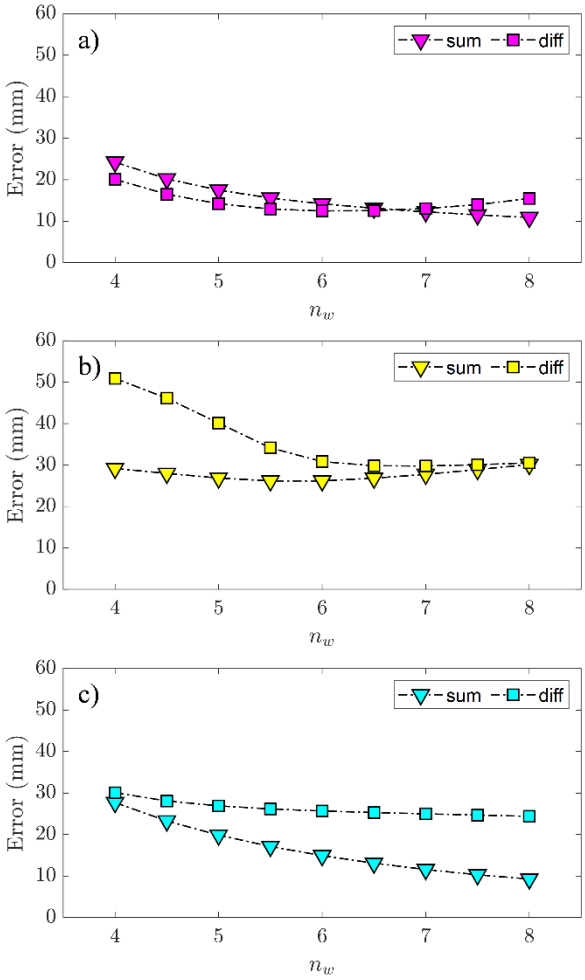

Fig. 4.13. Relationship between error and number of windows when using combined frequency wave at sum frequency harmonic and using difference frequency harmonic for a) Case A, b) Case B and c) Case C

4.7 Conclusions

A reference-free delamination damage detection in composite laminates using nonlinear combined frequency waves has been proposed in this paper. The proposed approach employs a time-frequency analysis and the combined frequency wave generated due to contact nonlinearity at the damage. Several damage cases with different damage locations have been investigated both within and beyond the area enclosed by the transducer network. The effect of the number of windows in the time-frequency analysis has been investigated and demonstrated that, for the cases studied in this paper, employing the sum harmonic frequency could provide more robust results, although there are some

limitations if the damage is located outside of the transducer network. Moreover, the time-frequency analysis in the proposed approach allows extraction of the signals without relying on baseline data and pave the way for in-situ damage localization and monitoring techniques as it has the potential to be implemented using multiplexing technology in the data acquisition system.

4.8 References

1. İpek, G., Y. Arman, and A. Çelik, *The effect of delamination size and location to buckling behavior of composite materials.* Composites Part B: Engineering, 2018. **155**: p. 69-76.
2. Klepka, A., et al., *Impact damage detection in composite chiral sandwich panels using nonlinear vibro-acoustic modulations.* Smart Materials and Structures, 2013. **22**(8): p. 084011.
3. He, Y., et al., *Non-destructive testing of low-energy impact in CFRP laminates and interior defects in honeycomb sandwich using scanning pulsed eddy current.* Composites Part B: Engineering, 2014. **59**: p. 196-203.
4. Addepalli, S., et al., *Non-destructive evaluation of localised heat damage occurring in carbon composites using thermography and thermal diffusivity measurement.* Measurement, 2019. **131**: p. 706-713.
5. Nesvijski, E., *Some aspects of ultrasonic testing of composites.* Composite Structures, 2000. **48**(1): p. 151-155.
6. Jang, B.-W. and C.-G. Kim, *Real-time detection of low-velocity impact-induced delamination onset in composite laminates for efficient management of structural health.* Composites Part B: Engineering, 2017. **123**: p. 124-135.
7. Mei, H., et al., *Vibration-Based In-Situ Detection and Quantification of Delamination in Composite Plates.* Sensors, 2019. **19**(7): p. 1734.
8. Ramadas, C., et al., *Interaction of guided Lamb waves with an asymmetrically located delamination in a laminated composite plate.* Smart Materials and Structures, 2010. **19**(6): p. 065009.
9. Su, Z. and L. Ye, *Fundamental Lamb Mode-based Delamination Detection for CF/EP Composite Laminates Using Distributed Piezoelectrics.* Structural Health Monitoring, 2004. **3**(1): p. 43-68.
10. Jhang, K.Y., *Nonlinear ultrasonic techniques for nondestructive assessment of micro damage in material: A review.* International Journal of Precision Engineering and Manufacturing, 2009. **10**(1): p. 123-135.
11. Xiang, Y., et al., *Effect of precipitate-dislocation interactions on generation of nonlinear Lamb waves in creep-damaged metallic alloys.* Journal of Applied Physics, 2012. **111**(10): p. 104905.
12. Pruell, C., et al., *A nonlinear-guided wave technique for evaluating plasticity-driven material damage in a metal plate.* NDT & E International, 2009. **42**(3): p. 199-203.
13. Bermes, C., et al., *Experimental characterization of material nonlinearity using Lamb waves.* Applied Physics Letters, 2007. **90**(2): p. 021901.

14. Matlack, K.H., et al., *Review of Second Harmonic Generation Measurement Techniques for Material State Determination in Metals.* Journal of Nondestructive Evaluation, 2014. **34**(1): p. 273.
15. Yang, Y., et al., *Second harmonic generation at fatigue cracks by low-frequency Lamb waves: Experimental and numerical studies.* Mechanical Systems and Signal Processing, 2018. **99**: p. 760-773.
16. Rauter, N., R. Lammering, and T. Kuhnrich, *On the detection of fatigue damage in composites by use of second harmonic guided waves.* Compos. Struct., 2016. **152**: p. 247.
17. Rauter, N. and R. Lammering, *Impact Damage Detection in Composite Structures Considering Nonlinear Lamb Wave Propagation.* Mechanics of Advanced Materials and Structures, 2015. **22**(1-2): p. 44-51.
18. Soleimanpour, R. and C.-T. Ng, *Locating delaminations in laminated composite beams using nonlinear guided waves.* Engineering Structures, 2017. **131**: p. 207-219.
19. Li, W., Y. Cho, and J. Achenbach, *Detection of thermal fatigue in composites by second harmonic Lamb waves.* Smart Materials and Structures, 2012. **21**(8): p. 085019.
20. Shan, S. and L. Cheng, *Mixed third harmonic shear horizontal wave generation: interaction between primary shear horizontal wave and second harmonic Lamb wave.* Smart Materials and Structures, 2019. **28**(8): p. 085042.
21. Li, W., et al., *Detection and Location of Surface Damage Using Third-Order Combined Harmonic Waves Generated by Non-Collinear Ultrasonic Waves Mixing.* Sensors, 2021. **21**(18): p. 6027.
22. Sampath, S. and H. Sohn, *Detection and localization of fatigue crack using nonlinear ultrasonic three-wave mixing technique.* International Journal of Fatigue, 2022. **155**: p. 106582.
23. Donskoy, D. and A. Sutin, *Vibro-Acoustic Modulation Nondestructive Evaluation Technique.* Journal of Intelligent Material Systems and Structures, 1998. **9**(9): p. 765-771.
24. Klepka, A., et al., *Nonlinear acoustics for fatigue crack detection – experimental investigations of vibro-acoustic wave modulations.* Structural Health Monitoring, 2012. **11**(2): p. 197-211.
25. Klepka, A., et al., *Impact damage detection in laminated composites by non-linear vibro-acoustic wave modulations.* Composites Part B: Engineering, 2014. **65**: p. 99-108.
26. Lim, H.J., et al., *Development and field application of a nonlinear ultrasonic modulation technique for fatigue crack detection without reference data from an intact condition.* Smart Materials and Structures, 2016. **25**(9): p. 095055.
27. Croxford, A., et al., *The use of non-collinear mixing for nonlinear ultrasonic detection of plasticity and fatigue.* The Journal of the Acoustical Society of America, 2009. **126**(5): p. EL117-EL122.
28. Jiao, J., et al., *Evaluation of the intergranular corrosion in austenitic stainless steel using collinear wave mixing method.* NDT & E International, 2015. **69**: p. 1-8.
29. Ju, T., et al., *Nondestructive evaluation of thermal aging of adhesive joints by using a nonlinear wave mixing technique.* NDT & E International, 2019. **103**: p. 62-67.
30. Hasanian, M. and C. Lissenden, *Second order ultrasonic guided wave mutual interactions in plate: Arbitrary angles, internal resonance, and finite interaction region.* Journal of Applied Physics, 2018. **124**(16): p. 164904.
31. Li, W., et al., *Theoretical analysis and experimental observation of frequency mixing response of ultrasonic Lamb waves.* Journal of Applied Physics, 2018. **124**(4): p. 044901.

32. Ishii, Y., S. Biwa, and T. Adachi, *Non-collinear interaction of guided elastic waves in an isotropic plate.* Journal of Sound and Vibration, 2018. **419**: p. 390-404.
33. Jiao, J., et al., *Nonlinear Lamb wave-mixing technique for micro-crack detection in plates.* NDT & E International, 2017. **85**: p. 63-71.
34. Metya, A., S. Tarafder, and K. Balasubramaniam, *Nonlinear Lamb wave mixing for assessing localized deformation during creep.* NDT & E International, 2018. **98**: p. 89-94.
35. Pineda-Allen, J.C. and C.T. Ng, *Nonlinear Guided-Wave Mixing for Condition Monitoring of Bolted Joints.* Sensors, 2021. **21**(15): p. 5093.
36. Yeung, C. and C.T. Ng, *Nonlinear guided wave mixing in pipes for detection of material nonlinearity.* Journal of Sound and Vibration, 2020. **485**: p. 115541.
37. Broda, D., et al., *Modelling of nonlinear crack–wave interactions for damage detection based on ultrasound—A review.* Journal of Sound and Vibration, 2014. **333**(4): p. 1097-1118.
38. Cantrell, J. and W. Yost, *Nonlinear ultrasonic characterization of fatigue microstructures.* International Journal of Fatigue, 2001. **23**: p. 487-490.
39. Deng, M. and J. Pei, *Assessment of accumulated fatigue damage in solid plates using nonlinear Lamb wave approach.* Applied Physics Letters, 2007. **90**(12): p. 121902.
40. Bermes, C., et al., *Nonlinear Lamb waves for the detection of material nonlinearity.* Mechanical Systems and Signal Processing, 2008. **22**(3): p. 638-646.
41. Solodov, I.Y., N. Krohn, and G. Busse, *CAN: an example of nonclassical acoustic nonlinearity in solids.* Ultrasonics, 2002. **40**(1): p. 621-625.
42. Yelve, N., M. Mira, and P. Mujumdar, *Spectral damage index for estimation of breathing crack depth in an aluminum plate using nonlinear Lamb wave.* Structural Control and Health Monitoring, 2014. **21**(5): p. 833-846.
43. Shkerdin, G. and C. Glorieux, *Nonlinear clapping modulation of lamb modes by normally closed delamination.* IEEE Transactions on Ultrasonics, Ferroelectrics, and Frequency Control, 2010. **57**(6): p. 1426-1433.
44. Biwa, S., S. Nakajima, and N. Ohno, *On the Acoustic Nonlinearity of Solid-Solid Contact With Pressure-Dependent Interface Stiffness.* Journal of Applied Mechanics, 2004. **71**(4): p. 508-515.
45. Yan, D., B.W. Drinkwater, and S.A. Neild, *Measurement of the ultrasonic nonlinearity of kissing bonds in adhesive joints.* NDT & E International, 2009. **42**(5): p. 459-466.
46. Ng, C.T. and M. Veidt, *A Lamb-wave-based technique for damage detection in composite laminates.* Smart Materials and Structures, 2009. **18**(7): p. 074006.
47. Wilcox, P.D., M.J.S. Lowe, and P. Cawley, *Mode and Transducer Selection for Long Range Lamb Wave Inspection.* Journal of Intelligent Material Systems and Structures, 2001. **12**(8): p. 553-565.
48. Pratt, W.K., *Digital image processing*. 4th ed. 2001, New York: Wiley-Interscience.

Chapter 5

Mixing of non-collinear Lamb wave pulses in plates with material nonlinearity

Juan Carlos Pineda Allen and Ching Tai Ng
School of Civil, Environmental and Mining Engineering
The University of Adelaide, SA 5005, Australia

Manuscript: Pineda Allen, J.C.; Ng, C.T. Mixing of non-collinear Lamb wave pulses in plates with material nonlinearity.

Statement of Authorship

Title of Paper	Mixing of non-collinear Lamb wave pulses in plates with material nonlinearity
Publication Status	☐ Published ☐ Accepted for Publication ☐ Submitted for Publication ☑ Unpublished and Unsubmitted work written in manuscript style
Publication Details	Pineda Allen, J.C.; Ng, C.T. Mixing of non-collinear Lamb wave pulses in plates with material nonlinearity

Principal Author

Name of Principal Author (Candidate)	Juan Carlos Pineda Allen
Contribution to the Paper	Performed literature review, developed numerical model, developed and prepared the experimental configuration. Performed numerical simulations and conducted experiments, data processing and analyses, and prepared the manuscript.
Overall percentage (%)	80%
Certification:	This paper reports on original research I conducted during the period of my Higher Degree by Research candidature and is not subject to any obligations or contractual agreements with a third party that would constrain its inclusion in this thesis. I am the primary author of this paper.
Signature	Date: 23/02/2022

Co-Author Contributions

By signing the Statement of Authorship, each author certifies that:

i. the candidate's stated contribution to the publication is accurate (as detailed above);

ii. permission is granted for the candidate in include the publication in the thesis; and

iii. the sum of all co-author contributions is equal to 100% less the candidate's stated contribution.

Name of Co-Author	Ching Tai Ng
Contribution to the Paper	Supervised the work, reviewed the manuscript, prepared for submission and acted as corresponding author.
Signature	Date: 24/02/2022

Name of Co-Author	
Contribution to the Paper	
Signature	Date:

Please cut and paste additional co-author panels here as required.

Chapter 5: Mixing of non-collinear Lamb wave pulses in plates with material nonlinearity.

Abstract

Guided waves have been extensively studied in the past few years, and more recently nonlinear guided wave have attracted significant research interest for its potential in early damage detection and material state characterization. Combinational harmonic generation due to wave mixing can offer some advantages over second harmonic generation. However, studies focused on Lamb wave mixing are still very limited and have mainly focused on collinear wave mixing and used plane wave assumption. In this paper, numerical simulation and experiments are conducted to understand interaction of mixing non-collinear Lamb wave pulses with non-planar wavefront. The results demonstrate that the generated secondary wave is cumulative under internal resonance conditions and sum-frequency component of the combinational harmonics is useful for characterizing material nonlinearities.

Keywords: wave mixing; non-collinear; Lamb wave; material nonlinearity; non-planar wavefront.

5.1 Introduction

Traditional guided wave (GW) testing is based on linear features, e.g. time-of-flight and amplitude of the scattered wave, which has been widely employed to evaluate materials and detect defects due to its outstanding capabilities, such as (a) ability to inspect inaccessible locations, (b) ability to inspect the entire cross-sectional area of the element, (c) excellent sensitivity, (d) cost-effectiveness, and (e) low energy-consumption. Ultrasonic techniques based on linear features are sensitive to macro scale-damage, such as gross defect or open cracks. However, they are insensitive to micro-scale damage, such as degradation or distributed micro-cracks, which are early-stage damage mechanisms.

5.1.1 Nonlinear guided waves

An alternative solution to this limitation is nonlinear ultrasonics [1], where the incident wave interacts with materials and generates nonlinear responses, e.g. higher harmonics and combinational harmonics, due to nonlinear mechanical behaviour. Harmonic generation is governed by two physical mechanisms, material nonlinearity and contact acoustic nonlinearity [2]. Material-related second order harmonic generation (or simply second harmonic generation) has been proven efficient in detecting microstructural changes, such as plasticity [3] and fatigue [4] in metallic specimens. Damage-related second harmonics generated by contact acoustic nonlinearity phenomenon has also been studied for detecting damage, such delamination in composites [5] and fatigue crack in metals [6]. However, second harmonics generation possess a difficulty in isolating the source of nonlinearity generated by testing equipment. Contact between the structure under inspection and the ultrasonic transducer also introduce nonlinearities that can mask the material and damage-related

nonlinearities. In addition, the magnitude of the second harmonic is usually very small, which is hard to be measured accurately.

5.1.2 Guided wave mixing

To overcome these aforementioned drawbacks, wave mixing method utilizing two ultrasonic waves at different single central frequencies has been developed in last few years [7]. Wave mixing method can be classified as collinear [8] and non-collinear [9] depending on the angle between the incident (primary) waves that generate the resonant (secondary) wave at combinational harmonics, and offer advantages in selecting wave modes, excitation frequencies and wave propagating directions.

Croxford *et al.* [9] employed bulk waves to characterize material nonlinearity due to fatigue and plasticity damage using the non-collinear method. Material nonlinearity was experimentally correlated to plastic deformation of aluminium alloy. A nonlinear acoustic parameter for collinear bulk wave mixing and strictly related to plastic deformation was introduced and validated numerically and experimentally [10]. Experimental studies demonstrated that the collinear method can measure localized plastic deformation [11]. Jiao *et al.* [12] determined the presence of fatigue crack using bulk shear waves and the non-collinear method. Codirectional Lamb wave mixing was used to investigate micro crack [13] and localized creep [14] detection in steel plates.

5.1.3 Lamb wave mixing

Ultrasonic Lamb waves, offer significant advantages for evaluation of structures, such as the ability to inspect in inaccessible locations, multimodality, flexibility in wave mode selection, ability to inspect multilayered or submerged structures, etc. Hasanian *et al.* [15] conducted comprehensive vector analyses for both

collinear and non-collinear methods using Lamb waves. However, they assumed the guided wave is a plane wave to explore the possible wave-modes combination triplets. Arbitrary angles between primary waves and secondary angle were studied, and internal resonant conditions were also assessed for wave mixing [16]. Ishii *et al.* [17] theoretically analysed nonlinear wave propagation in an homogenous and isotropic plate in order to elucidate the non-collinear interaction of monochromatic plane waves employing a perturbation analysis and infinite beam widths. They also conducted finite element analyses considering finite beam width and time durations to gain further understanding on the scattered wave generation. Li *et al.* [18] studied mixed-frequency response induced by codirectional Lamb waves and predicted generation of second and third order combinational harmonics.

Collinear wave mixing has the advantage that the wave mixing zone is larger than non-collinear wave mixing, but this makes it less suitable for inspecting localized regions. Counter-propagating waves mixing offer advantage for evaluating localized regions in structures [8]. However, non-collinear wave mixing offers more flexibility in the selection of the primary and secondary wave modes [16]. Analytical solutions for plane waves were developed for Lamb waves mixing but they are insufficient to capture the real testing conditions, such as non-planar wave front and influence of finite ultrasonic beam width on wave interaction. For practical applications, it needs to take into account these practical factors in Lamb waves mixing. Gaining physical insight of Lamb waves mixing phenomenon will expand the already recognized benefits and further advance in wave mixing methods.

The main objective of this paper is to investigate the feasibilty and capability of combinational harmonics measurement with non-collinear Lamb wave mixing under practical conditions. It focuses on gaining insight into the physical phenomena of secondary symmetric Lamb wave generation at combinational sum frequency when two fundamental modes of antisymmetric

Lamb waves (A_0), which have finite beam width, non-planar wavefront and finite time duration, interact with each other over a localized region under resonance conditions. The interaction of the two A_0 Lamb waves are expected to generate a secondary fundamental mode of symmetric Lamb wave (S_0) and this will be studied in details under practical situation. The cumulative nature of the secondary Lamb wave at combinational sum frequency is further investigated as this feature has proven to be a useful indication of material nonlinearity, fatigue and plasticity.

5.2 Theoretical background

Second order harmonics generated due to interaction between two primary waves are cumulative when internal resonance criteria are satisfied [19-21]. The two internal resonance criteria are (i) non-zero power flux from the primary to the secondary mode and (ii) phase matching. The non-zero power flux condition in Eq. (1) guarantees that power is transmitted through the surface and through the volume of the plate due to the primary wave, while the phase matching condition guarantees a sustaining power flux from the primary to the secondary waves.

$$f_n^{vol} + f_n^{surf} \neq 0 \tag{1}$$

The terms f_n^{vol} and f_n^{surf} are the driving forces transmitting power from the primary waves to the secondary wave through the volume and through the surface respectively.

Phase matching condition in Eq. (2), also known as synchronism, requires knowledge of the dispersion characteristics represented in the dispersion curves of Fig. 5.1. In this study, dispersion curves were calculated using DISPERSE®, under the assumption that the wavefront is an infinite plane and normal to the

direction of wave propagation. Waves can propagate in different directions; thus, when seeking triplets that are phase matched, wave vectors containing wave number and wave direction information are used. The wavenumber obtained from the interaction between primary wave must correspond to a propagating mode, and the phase velocity is then calculated with the relation $c_{ph} = 2\pi f/\kappa$, where c_{ph} is the phase velocity. κ_a, κ_b and κ_n are wavenumber for primary waves a, b and secondary wave n.

$$\kappa_a \pm \kappa_b = \kappa_n \tag{2}$$

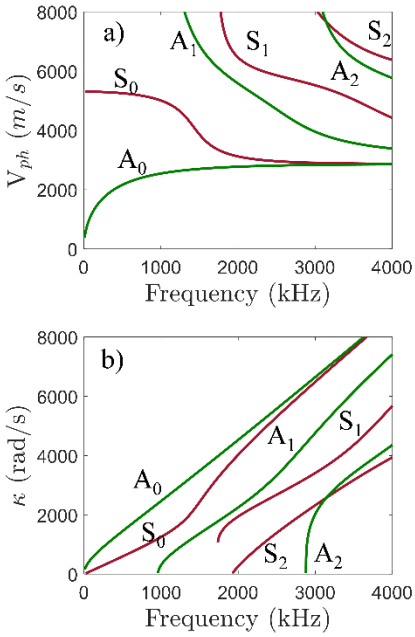

Fig. 5.1. a) Phase velocity, and b) wavenumber dispersion curves for 1.60mm thick aluminium plate

Most of the work developed to date is derived from plane waves with infinite beam width, aimed at analytically understanding the basis of wave mixing phenomena, however, they are not fully practical for real applications. Therefore, finite element simulations and experiments are needed for further understanding Lamb wave mixing under practical situation.

5.3 Finite element simulation

A three-dimensional (3D) finite element model developed using ABAQUS/Explicit was used in order to investigate non-collinear Lamb wave mixing. The model consists of a 6061-T6 aluminium plate. The material properties of the 6061-T6 are listed in Table 5.1. The dimensions of the plate are 270mm × 320mm × 1.60mm. The in-plane dimensions of the element used in the finite element model are 0.25mm × 0.25mm. There are seven layers of elements in the thickness direction of the plate and each element is 0.228mm thick. Approximately 20 elements/wavelength is the recommended spatial resolution for representing the propagation of Lamb wave [22]. Mechanical constitutive behaviour based on the nonlinear strain energy function of Murnaghan was modelled in ABAQUS through a VUMAT subroutine [23]. Eight-noded brick elements, C3D8I, with each node having three translational degrees-of-freedom and reduced integration were used.

Table 5.1. Material properties used in the simulations [24]

Density (kg/m^3)	l (GPa)	m (GPa)	n (GPa)	λ (GPa)	μ (GPa)
2704	-281.50	-339.00	-416.00	54.30	27.30

To contemplate practical applications, primary Lamb wave excitations consist of tone burst pulses applied as nodal displacement in the z direction to the nodes covered by the assumed ultrasonic transducer as indicated in the Fig. 5.2a. The interaction angle between the primary waves is defined by θ. The maximum applied displacement is 20 ηm. All the the remaining edges and boundaries of the plate are stress-free. An appropriate time delay was applied to the pulse excitation of the Lamb wave with faster group velocity in order to ensure both wave pulses arrive simultaneously at the region of interest.

Moreover, the distance between each excitation source and the mixing zone, whose centre is defined as the point P, is equal to each other. The primary waves are expected to interact at a finite region, and hence, it is not limited at the point P only.

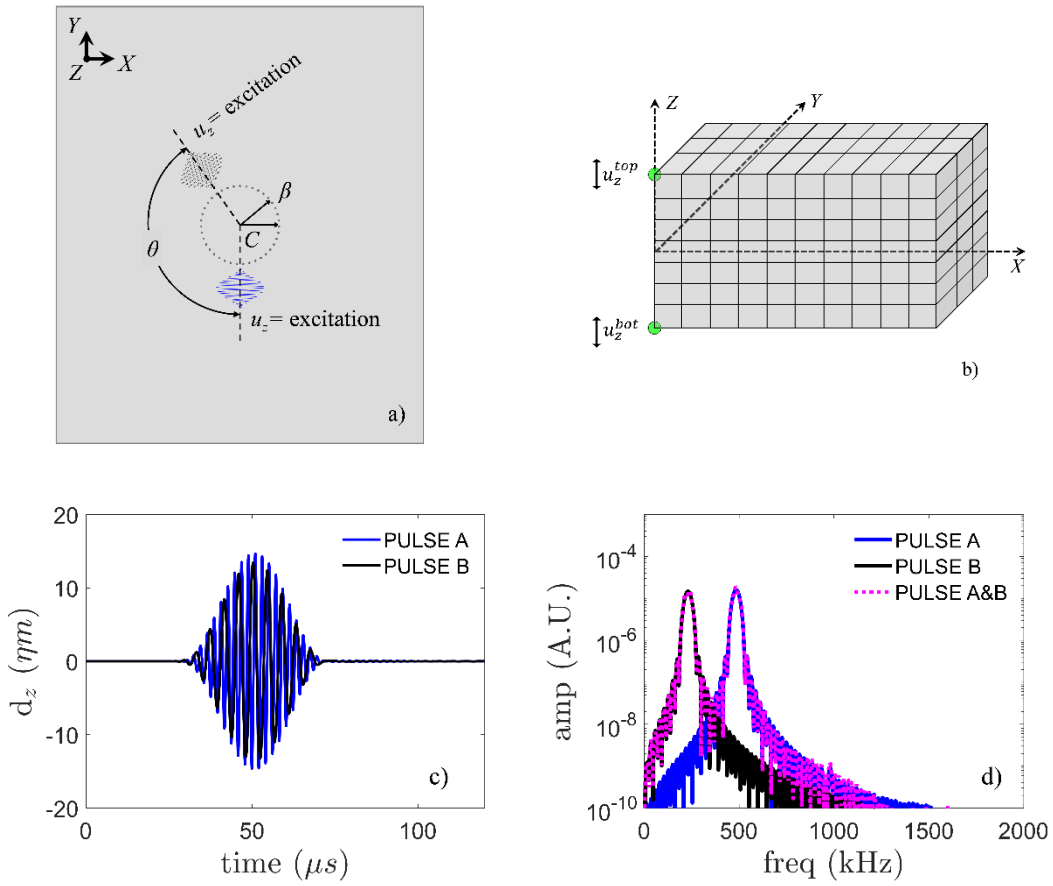

Fig. 5.2. a) schematic diagram of the non-collinear FE model, b) top and bottom nodal displacements, c) time-domain and d) frequency spectra of out-of-plane displacement of incident waves at point P.

To extract the scattered wave field, a substraction technique [15] is employed. Three different finite element simulations are carried out separately. In this approach all three simulations are performed with the identical finite element model except the generated wave is different. Three different generated waves are considered: (i) primary waves are generated simultaneously ($T_{A\&B}$), (ii) only primary wave A (T_A) is generated, and (iii) only primary wave B (T_B) is generated. The scattered wave field can be extracted by

$$T_{sca} = T_{A\&B} - T_A - T_B \tag{3}$$

Out-of-plane nodal displacement at top and bottom surfaces of the plate, as shown Fig. 5.2b, are obtained from each simulation. Displacement is obtained from nodes located along a circle of 30mm radius for a range of β angles from 5° to 360° in steps of 5°. The secondary symmetric Lamb wave is obtained by Eq. (4)

$$u_{sca} = \frac{1}{2} \times \left[u_{sca}^{top} - u_{sca}^{bot}\right] \tag{4}$$

where

$$u_{sca}^{top} = u_{z_{A\&B}}^{top} - u_{z_A}^{top} - u_{z_B}^{top} \tag{5a}$$

$$u_{sca}^{bot} = u_{z_{A\&B}}^{bot} - u_{z_A}^{bot} - u_{z_B}^{bot} \tag{5b}$$

In Eq. (5a), the first summand corresponds to the out-of-plane nodal displacement at the top surface of the plate when primary waves A and B are excited simultaneously, the subtrahends correspond to the out-of-plane nodal displacement at the top surface of the plate when primary wave A only and primary wave B only are excited separately. Similar interpretation is applied for Eq. (5b), although these values are obtained from the bottom surface of the plate.

Similarly, Eq. (6) can be used to obtain antisymmetric incident Lamb wave

$$u_{inc}^{A} = \frac{1}{2} \times \left[u_{inc}^{top} + u_{inc}^{bot}\right] \tag{6}$$

where

$$u_{inc}^{top} = u_{z_A}^{top} \tag{7a}$$

$$u_{inc}^{bot} = u_{z_A}^{bot} \tag{7b}$$

for simulation A. Correspondingly for simulation B,

$$u_{inc}^{B} = \frac{1}{2} \times \left[u_{inc}^{top} + u_{inc}^{bot}\right] \tag{8}$$

where

$$u_{inc}^{top} = u_{z_B}^{top} \tag{9a}$$

$$u_{inc}^{bot} = u_{z_B}^{bot} \tag{9b}$$

Excitation frequencies are selected so that the internal resonance conditions derived from plane waves assumption are theoretically satisfied. Additionally, wave modes selection is a determining factor for practical applications of nondestructive testing, and unwanted higher order wave modes can be avoided by employing fundamental modes. Hence, fundamental mode below the cut-off frequency is employed in this study. In particular, we are interested in primary A_0 waves that are expected to generate a secondary cumulative wave S_0 propagating mode [21], where nonzero power flux condition for non-collinear wave-mixing is satisifed by choosing the appropriate wave modes. Synchronism condition is employed to find dispersion relations based on frequency and direction. Triplet selected is: $f_a = 484\ kHz$ $(c_{ph} = 2141{,}9\ m/s,$ $\kappa_a = 1419{,}8\ rad/m)$, $f_b = 230\ kHz$ $(c_{ph} = 1658{,}9\ m/s,\ \kappa_b = 871{,}1\ rad/m)$ and $f_{sca} = 714\ kHz (c_{ph} = 5186{,}5\ m/s,\ \kappa_{sca} = 864{,}9\ rad/m)$. Interaction angle θ is 145° and expected direction γ of resonant wave is at $\beta = 55°$. The number of cycle is 31 and 15 for pulse A and B, respectively.

A_0 wave fields T_A and T_B at point P are shown in Fig. 5.2c. Maximum interaction occurs, with the maximum displacement of both incident pulses happening just after $50\mu s$. Frequency spectra of the A_0 component for wave fields T_A, T_B and $T_{A\&B}$ are shown in Fig. 5.2d, which shows the excitation frequencies acting separately as well as concurrently.

The non-planar primary Lamb waves are expected to propagate over a region that is not limited to point P. A snapshot of the displacement in the z direction of the top surface of the plate is shown in Fig. 5.3a. The displacement over a region of the plate must contain frequency components at excitation frequencies. The A_0 primary wave A and primary B were obtained by summing the out-of-plane nodal displacement at the top and bottom surface of the plate and their amplitude spectra at the corresponding f_a and f_b are calculated. Fig. 5.3b shows the polar plots of the directivity pattern of the incident wave amplitudes, which are obtained from the magnitudes at the excitation frequencies of amplitude spectra.

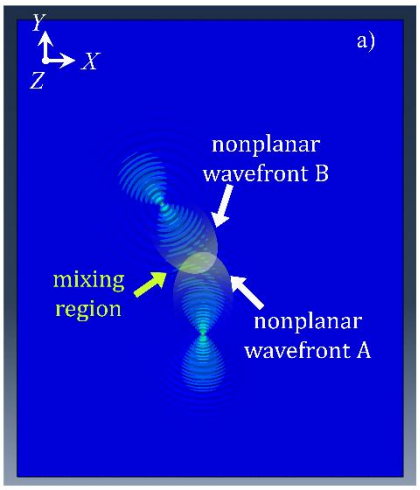

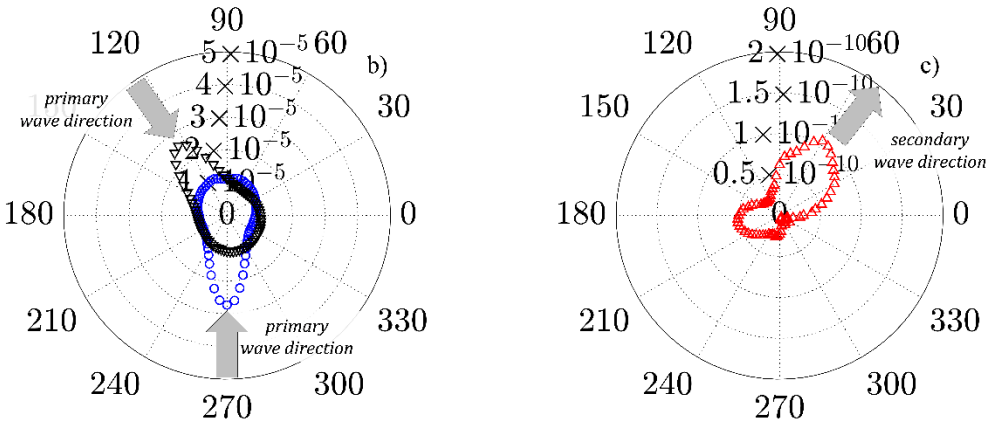

Fig. 5.3. a) Out-of-plane displacement at the top surface when A and B occur simultaneously, b) amplitude of A_0 component of simulations A at f_a and B at f_b, c) amplitude of S_0 component at f_{sca}

Interaction between two antisymmetric propagating Lamb waves are expected to produce symmetric Lamb wave at combinational harmonics due to wave mixing effect. Interaction occurs over a mixing region is shown in Fig. 5.3a, and hence, the secondary symmetric mode of Lamb wave due to local interaction effect is expected over this region. The combinational harmonic is expected to be cumulative along the scattered wave angle in view of the resonance condition. The S_0 is obtained using Eq. (4) and the amplitude spectra at the corresponding f_{sca} is calculated as shown in Fig. 5.3c.

Theory based on plane waves assumption can predict the direction of the scattered wave, but it has the limitation that is not fully practical for real applications. However, with numerical simulations we are able to understand how wave mixing phenomenon occurs when primary Lamb waves with finite beam width and non-planar wavefront interact with each other. It can be seen from Fig. 5.3c that directivity pattern of the secondary S_0 at the combinational sum frequency f_{sca} shows that maximum amplitude occurs towards the resonant angle. Some deviation could be expected given that dispersion curves from Fig. 5.1 were calculated based on plane wave assumption. Cumulative nature of the secondary wave at the combinational frequency is then evaluated at the expected

resonant direction ($\beta = 55°$) by extracting the S_0 component of the scattered Lamb wave, and normalizing its amplitude at f_{sca} by the product of the amplitudes at f_a and f_b of the A_0 component incident waves along ten points every 20mm. The results are shown in Fig. 5.4, which has linearly increasing trend with cumulative nature due to material nonlinearity.

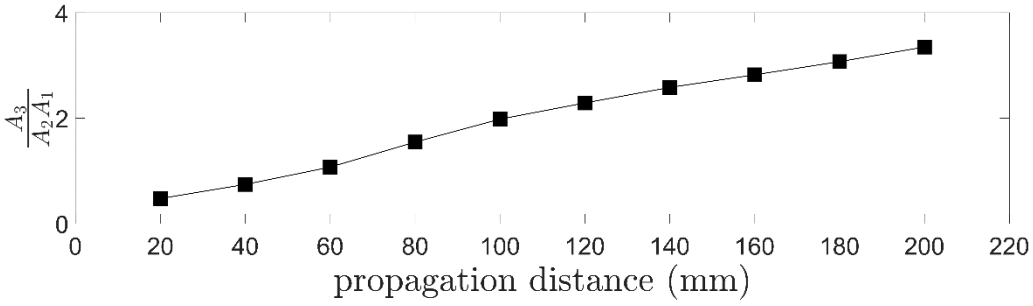

Fig. 5.4. Cumulative behaviour of the secondary wave

5.4 Experimental study

A 300mm×300mm×1.60mm 6061-T6 aluminium plate was used in experiment to observe the wave mixing responses of two primary non-collinear Lamb waves due to their mutual interaction under resonance conditions. Two wedge tranducers designed for generating antisymmetric propagating mode Lamb wave were used. The wedge transducer consists of a teflon wedge and longitudinal wave transducer. Using Snell's law, the oblique angles of the wedges are calculated as $\theta_a = 38°$ (f_a=484kHz) and $\theta_b = 53°$ (f_b=230kHz). Two PC-controlled NI PXI-5412 waveform generators were used to generate two independent signals. Both signals consist of sinusoidal tone-burst waves modulated by Hann window. Signals are amplified by two separate amplifiers. Transducer-wedge interface and wedge-specimen interface were coupled with light motor oil and clamped to the surface of the plate. Since the pulse with f_a frequency propagates faster than the pulse with f_b frequency, an appropiate time delay was applied during the excitation signal generation; distance between

wedge tranducers and measurement point was kept constant. A schematic diagram is shown in Fig. 5.5.

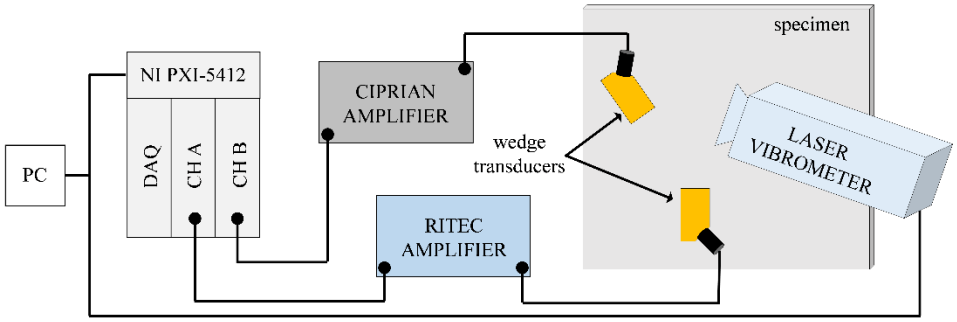

Fig. 5.5. Schematic representation of the experimental setup

Tests to explore the generation of the antisymmetric Lamb wave were conducted first to confirm successful generation of the primary waves. In order to confirm this, each transducer was actuated separately and the out-of-plane displacements at different locations were measured using a 1D scan by Polytec PSV-400-M2-20 scanning laser vibrometer. Group velocity was calculated using the time-of-flight of the signal envelope obtained from the Hilbert transform and distance between consecutive measurement points. Group velocity is $V_{gr} = 3032\, m/s$ for the pulse A and $V_{gr} = 2701\, m/s$ for the pulse B, which are in good agreement with the analytical values from the dispersion curve corresponing to the A_0 wave ($V_{gr} = 3036\, m/s$ and $V_{gr} = 2697\, m/s$).

Pulses A and B are excited simultaneously to study their mutual interaction. Also, pulses A and B are excited separately, so as to extract combinational harmonic that only ocurrs when Lamb waves interact simultaneously. Frequency content of the out-of-plane displacement in the mixing zone is shown in Fig. 5.6a. Additional frequency components due to mutual interaction are observed at two combinational frequencies, namely $f_a + f_b$ and $2f_a + f_b$. They do not appear when pulses are excited separately. In this paper, we aim to report the secondary wave at combinational sum frequency $f_a +$

f_b as indicative of material nonlinearity. To assess the cumulative nature of the generated seconday pulse, a different set of measurements was conducted along a line of ten sensing points in 10mm intervals at the expected direction of the resonant wave, $\gamma = 55°$. Then, the amplitude spectrum of the secondary wave is normalized by the product of the amplitude spectrum of the primary waves and plotted as function of propagation distance as shown in Fig. 5.6b. This linear increase indicates that the secondary wave can grow cumulatively [19], thereby validating its cumulative nature with propagation distance. As such, in plate-like structures, this practical phenomenon has proven to be practical and useful for characterizing weak material nonlinearity, plasticity and fatigue [9].

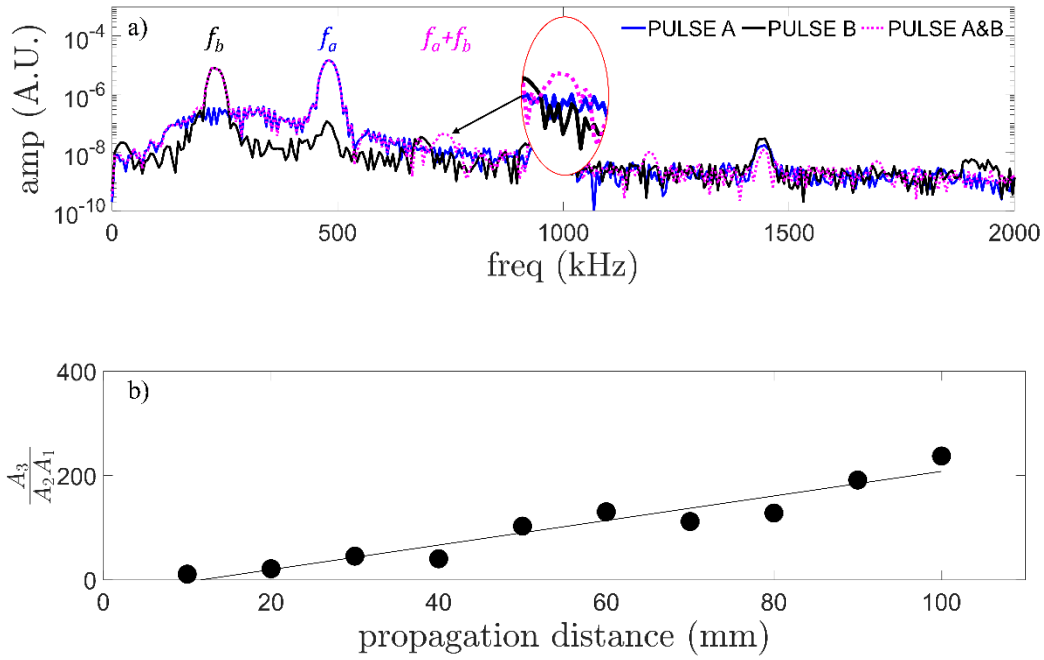

Fig. 5.6. a) Frequency spectra when pulses are excited simultaneously and separately, b) experimental cumulative behaviour of the secondary wave.

5.5 Conclusions

This paper has shown that combinational harmonic generated from Lamb waves mixing under practical conditions of finite beam width, finite pulse duration and finite interaction region can be used as an indication of material nonlinearity

based on the internal resonance. Given the non-planar wavefront generated by the incident pulse, an important physical insight indicates that combinational harmonics generation takes place due to local interaction effect over the mixing region, and that the magnitude distribution of this local effect is further consistent with the internal resonance criteria. It has been demonstrated that cumulative nature of the combinational harmonic are effective and practical for measuring plastic deformation and fatigue-related material degradation, as such this particular study takes a significant step towards real world applications. Moreover, the use of A_0 Lamb waves brings potential for advancing wave mixing damage detection techniques, like debonding, delamination or impact, which have not been fully investigated in the literature.

5.6 References

1. Chillara, V. and C. Lissenden, *Review of nonlinear ultrasonic guided wave nondestructive evaluation: theory, numerics, and experiments.* Optical Engineering, 2015. **55**(1): p. 011002.
2. Jhang, K.Y., *Nonlinear ultrasonic techniques for nondestructive assessment of micro damage in material: A review.* International Journal of Precision Engineering and Manufacturing, 2009. **10**(1): p. 123-135.
3. Pruell, C., et al., *A nonlinear-guided wave technique for evaluating plasticity-driven material damage in a metal plate.* NDT & E International, 2009. **42**(3): p. 199-203.
4. Deng, M. and J. Pei, *Assessment of accumulated fatigue damage in solid plates using nonlinear Lamb wave approach.* Applied Physics Letters, 2007. **90**(12): p. 121902.
5. Soleimanpour, R., C.T. Ng, and C. Wang, *Higher harmonic generation of guided waves at delaminations in laminated composite beams.* Structural Health Monitoring, 2017. **16**(4): p. 400-417.
6. Yang, Y., C.T. Ng, and A. Kotousov, *Influence of crack opening and incident wave angle on second harmonic generation of Lamb waves.* Smart Materials and Structures, 2018. **27**(5): p. 055013.
7. Van Den Abeele, K.E.A., P.A. Johnson, and A. Sutin, *Nonlinear Elastic Wave Spectroscopy (NEWS) Techniques to Discern Material Damage, Part I: Nonlinear Wave Modulation Spectroscopy (NWMS).* Research in Nondestructive Evaluation, 2000. **12**(1): p. 17-30.
8. Sun, M., et al., *Experimental and numerical investigations of nonlinear interaction of counter-propagating Lamb waves.* Applied Physics Letters, 2019. **114**(1): p. 011902.

9. Croxford, A., et al., *The use of non-collinear mixing for nonlinear ultrasonic detection of plasticity and fatigue.* The Journal of the Acoustical Society of America, 2009. **126**(5): p. EL117-EL122.
10. Liu, M. and et al., *Measuring acoustic nonlinearity parameter using collinear wave mixing.* J. Appl. Phys., 2012. **112**: p. 24908.
11. Tang, G., et al., *Detecting Localized Plastic Strain by a Scanning Collinear Wave Mixing Method.* Journal of Nondestructive Evaluation, 2014. **33**(2): p. 196-204.
12. Jiao, J., et al., *Fatigue crack evaluation using the non-collinear wave mixing technique.* Smart Materials and Structures, 2017. **26**(6): p. 065005.
13. Jiao, J., et al., *Nonlinear Lamb wave-mixing technique for micro-crack detection in plates.* NDT & E International, 2017. **85**: p. 63-71.
14. Metya, A., S. Tarafder, and K. Balasubramaniam, *Nonlinear Lamb wave mixing for assessing localized deformation during creep.* NDT & E International, 2018. **98**: p. 89-94.
15. Hasanian, M. and C. Lissenden, *Second order harmonic guided wave mutual interactions in plate: Vector analysis, numerical simulation, and experimental results.* Journal of Applied Physics, 2017. **122**(8): p. 084901.
16. Hasanian, M. and C. Lissenden, *Second order ultrasonic guided wave mutual interactions in plate: Arbitrary angles, internal resonance, and finite interaction region.* Journal of Applied Physics, 2018. **124**(16): p. 164904.
17. Ishii, Y., K. Hiraoka, and T. Adachi, *Finite-element analysis of non-collinear mixing of two lowest-order antisymmetric Rayleigh–Lamb waves.* The Journal of the Acoustical Society of America, 2018. **144**(1): p. 53-68.
18. Li, W., et al., *Theoretical analysis and experimental observation of frequency mixing response of ultrasonic Lamb waves.* Journal of Applied Physics, 2018. **124**(4): p. 044901.
19. Ishii, Y., S. Biwa, and T. Adachi, *Non-collinear interaction of guided elastic waves in an isotropic plate.* Journal of Sound and Vibration, 2018. **419**: p. 390-404.
20. de Lima, W.J.N. and M.F. Hamilton, *Finite-amplitude waves in isotropic elastic plates.* Journal of Sound and Vibration, 2003. **265**(4): p. 819-839.
21. Chillara, V. and C. Lissenden, *Interaction of guided wave modes in isotropic weakly nonlinear elastic plates: Higher harmonic generation.* Journal of Applied Physics, 2012. **111**(12): p. 124909.
22. Moser, F., L.J. Jacobs, and J. Qu, *Modeling elastic wave propagation in waveguides with the finite element method.* NDT & E International, 1999. **32**(4): p. 225-234.
23. Yang, Y., et al., *Finite element prediction of acoustoelastic effect associated with Lamb wave propagation in pre-stressed plates.* Smart Materials and Structures, 2019. **28**(9): p. 095007.
24. Willberg, C., et al., *Comparison of different higher order finite element schemes for the simulation of Lamb waves.* Computer Methods in Applied Mechanics and Engineering, 2012. **241-244**: p. 246-261.

Chapter 6

Conclusion

Chapter 6: Conclusions

6.1 Summary

This thesis has investigated nonlinear guided waves using combined frequency waves for damage detection in structures. It has systematically studied the advantages of nonlinear guided-wave mixing for its applications of NDT and SHM. The first part of the thesis introduced general concepts related to NDT and SHM, and continued with a more detailed explanation of the nonlinear guided wave based techniques.

In Chapter 2, a theoretical approach has been developed that correlates the applied torque at a bolted joint to the amplitude of the combined frequency wave at the sum harmonic frequency. The mathematical derivation considered the joint as a one-degree-of-freedom system whose stiffness can be associated to the contact effect generated between the joint plates when the guided wave passes through the joint. The contact effect is reflected in the combined frequency wave and its amplitude, and can indicate the level of applied torque at the bolted joint. The proposed method has been experimentally verified and further its robustness has been demonstrated for different time durations of the incident pulse. Small and inexpensive piezoelectric transducers potentially pave the way for future online condition monitoring.

In Chapter 3, a Lamb wave-mixing based technique has been proposed to detect debonding damage in an adhesive joint. A custom made wedge-transducer has been used to increase the excitability of the antisymmetric Lamb wave. Different frequency pairs have been investigated, and showed that the presence of a combined frequency wave indicated the presence of debonding. A validated numerical model has then been employed to evaluate the effect of the debonding width. It has been found that the amplitude of the transmitted energy

at the combined frequency wave can be correlated to the debonding width within a specific range.

In Chapter 4, a composite laminate plate has been studied. Experiments have been carried out to validate a developed numerical model. The numerical model has then been used to conduct further simulations in order to locate a delamination type of damage based on a time-frequency analysis and a network of transducers. A contact nonlinearity is generated when the incident Lamb wave interacts with the delamination damage and generates combined harmonics that indicate the presence of damage. The combined frequency waves exist at sum frequency harmonic and difference frequency harmonic, which are extracted using a time-frequency analysis. A reference free imaging algorithm has been developed to identify the location of the damage on a composite laminate with a network of transducers. The proposed approach does no rely on baseline data to locate the damage, and thus the technique has the potential to be implemented using multiplexed data acquisition systems for in-situ structural health monitoring applications.

In Chapter 5, a study using a non-collinear Lamb wave mixing technique under resonance conditions has been investigated. Interaction of two primary waves with material nonlinearity under resonance conditions are expected to produce a secondary wave. Finite duration pulses and non-planar wavefront were studied for the purpose of investigating that material nonlinearity can be estimated. Numerical simulation and laboratory experiments demonstrated that for non-planar wave fronts the cumulative nonlinear parameter can also indicate material nonlinearity.

To sum up, this research has explored and capitalized the potential of guided wave mixing in plate-like structures. Different types of damages and variety of materials have demonstrated that guided wave mixing can be

effectively used to detect damages such as debonding, bolt looseness and delamination, in aluminium, steel and composite laminates respectively.

6.2 Recommendations for future research

Despite the advancement achieved in this research, there are few suggestions that could lead to future research directions.

The bolt condition monitoring approach proposed can be extended as to monitor multiple bolts with fewer transducers. Multiple reflections may posses some challenges but combined frequency harmonics would theoretically have different arrival times, so a time-frequency analysis could be useful. Bolted joints are also widely used in composite structures and this could be another research direction.

For the aluminium adhesive joint, greater values of debonding width to wavelength ratios could be studied. However, when damage is too large, linear guided wave techniques could be enough for the purpose of debonding detection. Similarly, the effect of more than one debonding location could be investigated. A scattering study could also investigate the amplitude and modal characteristics of the generated nonlinear wave in different directions.

The proposed imaging algorithm could be experimentally demonstrated. Different incident frequency pair that generate a more obvious difference frequency harmonic can also be studied in order to evaluate if the performance of the imaging algorithm is also stable as it has been demonstrated using the sum frequency harmonic.

For the aluminium plate with material nonlinearity, further studies are recommended to evaluate the size of the mixing area and investigate its effect on the generated resonant wave.